

Orbital Structure of Interacting Galactic Systems

by

Andrés Felipe Gómez Muñoz

Submitted to the Institute of Physics
in partial fulfillment of the requirements for the degree of

Bachelor of Astronomy

at the

UNIVERSIDAD DE ANTIOQUIA

July 2021

© U 2021. All rights reserved.

Certified by

Juan Carlos Muñoz Cuartas

Associate Professor and Head of Graduate Programs in Physics
Thesis Supervisor

Orbital Structure of Interacting Galactic Systems

by

Andrés Felipe Gómez Muñoz

Submitted to the Institute of Physics
on July 31, 2021, in partial fulfillment of the
requirements for the degree of
Bachelor of Astronomy

Abstract

The mechanical state that can be constructed from observations for a pair of interacting galaxies is investigated. For that we define the orbital structure of a system as the probability density distribution of the possible states given the available observations with the purpose of easily estimating any physical property of the system with a meaningful error. We propose two approaches to the orbital structure. In one, the interacting galaxies are studied in an early stage as a two body problem and a distribution function of the orbital elements is obtained based on the observation of the positions of the galaxies in the sky as well as its velocities along the line-of-sight. Important symmetries, simplifications and interpretations concerning the nature of the interaction of the pair are obtained from the analysis of the resultant orbital structure. In the second one, we consider interacting pairs in which tidal features are present and can be unequivocally associated to a given disk. A mapping from the tidal regions to the possible orientations of the disk with respect to the angular momentum of the two body orbit is proposed. We perform a statistical analysis for systems in which one galaxy is face-on (with $i = 0$) and other have any inclination with angle of periapsis $w = 0$. The result shows that the mapping proposed can determine the orientation within a solid angle of $\approx 0.03(4\pi)$ with a confidence interval of 99% in the worst case scenario. The last under the assumption that with the exception of the galaxies' orientation the rest of the parameters are known and observations with uniformly high resolution and signal-to-noise ratio are present (these observations are modeled).

Thesis Supervisor: Juan Carlos Muñoz Cuartas

Title: Associate Professor and Head of Graduate Programs in Physics

Acknowledgments

I would like to express my everlasting gratitude to Prof. Juan Carlos for his continued support, guidance, patience and wisdom. They will always remain with me to become a better scientist than I was yesterday. In particular, I want to thank him for his almost unconditional trust in me as a brilliant scientist.

I would also like to thank all my teachers and colleagues in the physics institute which in different degrees helped to shape my mind as a scientist. In this respect, I specially thank Jorge Ivan Zuluaga, Luis Fernando Quiroga, Johny Alexander Jaramillo, Laura Catalina Arboleda, and Luis Abelardo Papiernik.

Finally, I want to thank my friends and especially my girlfriend for their company during the years of my career. But above all, I want to thank my parents and brother for his continuous and unconditional love and support, which have served to me as a stronghold to pursue my dreams as a scientist independent of any circumstances. As a result, I dedicate this work to them.

Contents

1	Introduction	15
2	Theoretical Framework	21
2.1	Introduction	21
2.2	Observations and galaxy morphology	21
2.2.1	Elliptical Galaxies	22
2.2.2	Spiral or Disk Galaxies	23
2.2.3	Lenticular and Irregular Galaxies	25
2.3	Basic Dynamics and Kinematics	25
2.3.1	The Two Body Approximation	26
2.3.2	The Orbits of Stars and Potential Theory	28
2.4	Collisionless Systems	32
2.4.1	Galactic Profiles as Distribution Functions	32
2.4.2	Justification of Collisionless Nature	33
2.4.3	Jeans Equations	35
2.4.4	Stationary solutions and angle-action variables	37
2.5	Collisions and Encounters of Stellar Systems	38
2.5.1	The Fokker-Plank Equation and Dynamical Friction	38
2.5.2	Tidal forces	39
2.5.3	Nth Body Algorithms	41
3	Orbital Structure of Galactic Pair Mergers in Early Stages	43
3.1	Orbital Structure	44

3.1.1	Orbital elements and state vector connection	45
3.2	Orbital Structure Construction	46
3.2.1	Priors	47
3.2.2	Observational Data Used	49
3.2.3	Summary of Methodology	50
3.3	Analysis of Posteriors for Some Cases	50
3.3.1	Marginalizations	51
3.4	Analysis of Symmetries	59
3.4.1	Reflection Symmetries and Computational Identification	60
3.4.2	Analytical Proof of the Prospect Symmetry	61
3.4.3	Symmetric Distributions Analysis and Families of Orbits	63
3.5	Observational errors	66
3.6	Conclusions	70
4	Galactic Pair Collisions in Systems with Tidal Features	71
4.1	Introduction	71
4.2	Identikit Methodology Explained	73
4.2.1	Ground True Data	75
4.3	Identikit Applied	86
4.3.1	Disk Spins	86
4.4	Uncertainties	94
4.4.1	Confidence Intervals of i and w	94
4.4.2	Compared Errors in Both Disks	99
4.5	Conclusions	101

List of Figures

2-1	Isophotes of galaxy M87	23
2-2	M101 and M104 classified according to the Hubble system	25
2-3	Approximate physical picture of a weak field interaction between two point particles	34
2-4	NGC 4676, example of a galaxy with elongated tidal tails	40
3-1	Geometric representation of the orbital parameters in a two body problem	46
3-2	One dimensional marginal distributions for the orbital elements for AM 2229-735.	53
3-3	Two dimensional marginal distributions for the orbital elements for AM 2229-735.	54
3-4	One dimensional marginal distributions for the orbital elements for AM 2322-821.	56
3-5	Two dimensional marginal distributions for the orbital elements for AM 2322-821.	57
3-6	One dimensional histograms of the orbital structure using the (i, ω, ν) symmetry for the system AM 2229-735.	65
3-7	Correlations maps between orbital parameters for the system AM 2229-735 considering errors in the observed component x_{sky} of the relative orbital state vector of the system in the sky plane.	67
3-8	Correlations maps between orbital parameters for the system AM 2229-735 considering errors in the observed component y_{sky} of the relative orbital state vector of the system in the sky plane.	68

3-9	Correlations maps between orbital parameters for the system AM 2229-735 considering errors in the observed component $v_{z,sky}$ of the relative orbital state vector of the system in the sky plane.	69
4-1	Modeled galactic pair collisions. Images from [1]	74
4-2	Geometrical representation of galaxy spins and abstract representation of the parameters space.	76
4-3	Grid division in a treecode algorithm, two dimensional instructive case.	81
4-4	Basic description of the GUI of the program Identikit [2].	87
4-5	Galaxy's orientations probability distributions from the selected tidal regions: systems with $(i_1, w_1) = (0, 0)$, $w_2 = 0$ and i_2 taking on $10^\circ, 20^\circ, \dots, 60^\circ$ values.	88
4-6	Galaxy's orientations probability distributions from the selected tidal regions: systems with $(i_1, w_1) = (0, 0)$, $w_2 = 0$ and i_2 taking on $70^\circ, 90^\circ, \dots, 120^\circ$ values.	89
4-7	Galaxy's orientations probability distributions from the selected tidal regions: systems with $(i_1, w_1) = (0, 0)$, $w_2 = 0$ and i_2 taking on $130^\circ, 140^\circ, \dots, 180^\circ$ values.	90
4-8	At the left: cumulative distribution function of the relative errors in the estimated orientations for disks 1. At the right: the estimated values of the inclination and the angle of periapsis for disks 1.	93
4-9	Resultant distributions for the inclination i and the angle of periapsis w , for the case in which disk 1 has $i = 40^\circ$ and $w = 0$	95
4-10	Resultant distributions for the inclination i and the angle of periapsis w , for the case in which disk 1 has $i = 70^\circ$ and $w = 0$	95
4-11	Estimated values for the inclinations of disks 1 using the maximum and mean of the resultant inclination distribution.	97
4-12	Estimated values for the angles of periapsis of disks 2 using the maximum and the mean of the resultant angle of periapsis distribution.	98

List of Tables

3.1	AM 2229-735: observed components of the relative orbital state vector in the plane of the sky, maximum error in those observed components, and mass as well as size for each galaxy.	51
3.2	AM 2322-82: observed components of the relative orbital state vector in the plane of the sky, maximum error in those observed components, and mass as well as size for each galaxy.	55
3.3	Proposed symmetries for the system AM 2229-735 orbital structure at the left and the computational result of evaluating each symmetry at the right.	61

Chapter 1

Introduction

Since ancient times, mankind has looked up to the sky intrigued by the structure and set of rules that celestial objects obey. In particular, galaxies hypothesized since 1750 by Thomas Wright were the subject of discussion until 1924, when Edwin Hubble showed that "spiral nebulæ" were distant galaxies. The discovery of galaxies broadened our concept of the universe and opened an unique opportunity to understand our own galaxy and place in the universe. One important fact about galaxies is that their evolution is highly driven by collisions. In this thesis we investigate galactic pair collisions by proposing methodologies that intend to reconstruct the mechanical state of such systems from their respective observations. For that end we will justify the construction of a distribution function (DF) of the possible states given the observations; the name of this DF will be referred to as orbital structure. The motivation is to build an orbital structure that will be capable of characterizing any physical information of the system with a meaningful confidence interval.

At first glance, the problem proposed appears to be simple. A galactic system is composed of stars, gas, dark matter, and dust. Therefore, to know the mechanical state we would only need to measure the velocities and position of their respective components. Nevertheless, it is not easy to obtain such information as it is illustrated by important complications:

- Galaxies normally reside far away so that it is not possible to resolve individual

stars; less gas and dust particles. Instead the movement of groups of stars, dust, and gas particles are measured.

- These observations combined with the fact that galaxies have several forms, sizes and orientations implies limitations in the knowledge on the distances that they have to us.
- Dark matter has been found to interact only gravitationally, and as we study it by the effects that it has on observable matter there is a natural indeterminacy in this component.
- As galaxies evolve appreciably over scales of *Gyr* and are far away it is not possible to resolve velocities along the plane of the sky; with counted exceptions such as our own galaxy and the Large Magellanic Cloud (LMC).
- Prohibited times of exposition are often needed to measure some components, e.g. gas in HII regions or star radiation in a dim galaxy.

Naturally, many approaches that try to circumvent such difficulties have been proposed. Generally speaking they can be divided in two. On the one hand, those that study a particular interacting galaxy pair system and intend to reconstruct its mechanical state from its observations and computational simulations. On the other hand, those that study the statistical properties from sets of interacting galaxy pair systems that will collide, which are either obtained from simulations or observations.

Before briefly describing them, we point out that both types of studies make great use of the fact that under classical mechanics the extended bodies considered (galaxies, mergers, galactic clusters) can be modeled as point masses orbiting under the influence of their mutual self-gravity. This is broadly used to evolve a set of previous states of the system to the possible instant in which the system is observed. The previous states depend on the system on consideration. A commonly used approach for an interacting pair is to consider the velocity and density profiles as known, as well as the possible orbits that the galaxies had, all this when galaxies were so separate that each could be regarded as isolated.

The studies that focus into particular galaxy pairs have been formerly studied since approximately 1950 [1]. They have evolved to encompass methods that consider the match and use of complex observations and models, as well as complicate codes. For example, they use tidal features [3, 2, 4, 5], spiral arms [6], warps [7], rings [8], the structure and dynamics of unseen matter [9, 10, 11], dynamical friction [12], mass transfer [13], magnetic fields [14], turbulence, gas dynamics [15] and other considerations [16, 17, 18].

Despite the different data and methodologies used in all of these works, there are several key practices that are commonly adopted, as [3] pointed out.

- Detailed velocity information in the form of HI data is available to constrain the model.
- Astrophysical arguments are used to estimate several critical parameters—specifically, the mass ratio μ , the initial orbital eccentricity e , and the pericentric separation p .
- The models focus on reproducing the large scale morphology and kinematics of the tidal tails (or other features); tidal tails are fundamental since they evolve ballistically and therefore carry memory of the initial conditions.
- Test-particle models with rigid galaxy potentials, constrained to follow realistic merger trajectories, are used to narrow down the range of parameter space.
- Fully self-consistent N-body models are used to refine the final model.
- Simulation particles are plotted over orthogonal projections of the data cube HI to show that the final model reproduced both the morphology and the kinematics of the merger.

Several works illustrate the points made above. The work [3] also intends to offer a survey of such dynamical models of interacting galaxies which make significant use of kinematic constraints. In fact, the work [3] classifies 57 papers according to their considerations about the nature of the interacting pair (e.g. a pair or spiral galaxies) as well as the observations used to match the model. In this last respect the matches

are divided in morphology, kinematics in 1D, kinematics in 2D, qualitative (e.g. visual resemblance between modeled and ground true observations in the plane of the sky), and genetic algorithms; for more details please refer to [3].

On the other hand, the studies that focus on the statistical properties of sets of interacting galaxy pair systems about to collide have been studied formerly since approximately 1970 [19]. Nevertheless, the initial studies focused principally on the mass distribution of infalling halos, and therefore galaxies [20]. In fact, other parameters as orbital elements are shortly mentioned. More recent works [19, 21, 22] give more focus to other important parameters as the orbital elements of infalling galaxies. As an example, in [23] the distributions for the eccentricity and the pericentre of infalling satellite haloes are constructed. Therefore, proposing orbital element distribution priors that could be used in systems of certain masses. Additionally, the work also shows that the redshift or the mass of the host galaxy could be considered to affect such distributions (of the pericentre and eccentricity).

Now, although all these works represent excellent progress, there is not at the moment a direct mapping from the mechanical state to the observational data of the merging systems [24, 25]. Nevertheless, probability distributions over sets of parameters that characterize a merger have been constructed taking into account the available observations [4]; what we called the orbital structure. In this thesis we identified the use of the orbital structure as a fundamental key to the success of a model. This is well justified by our main motivation already exposed, that is, such representation will be capable of characterizing any physical information of the system with a meaningful confidence interval.

Furthermore, the methodologies to construct the orbital structure can be explored in Bayesian terms, so that new information (either new dynamical interactions or observations) could be readily included. This last consideration became insightful for the evaluation of how the orbital structure changes under a series of approximations.

Furthermore, the acceptance of this idea in the community could lead to construct effective theories of incomplete observables. This means that given a general galactic interacting pair we would know what sets of incomplete observations could lead us to characterize its mechanical state within a desired error. As a final comment, the study of galactic mergers have shown to be important not only in galactic evolution, but as well as in other areas. This is because the same algorithms and methodologies can usually be applied to other fields such as cosmology, stellar evolution, statistical physics, planetary science, continuous mechanics, or plasma physics [26, 27].

With everything said, the thesis was divided in 4 chapters. In chapter 2 the theoretical framework is exposed. In chapter 3, a methodology for the construction of the orbital structure was studied for interacting galactic pairs in an early stage. Finally, in chapter 4 it was investigated how tidal features can be used in the determination of the orbital structure.

In chapter 3 the evolution in an early stage is treated as a two-body problem. Therefore, reducing the orbital structure to the knowledge of the orbital elements. Then, based on justified priors for the orbital elements, Monte Carlo methods, and observational data, a posterior distribution is constructed. Namely, the observations used are the centers of the galaxies in the sky plane and their velocities along the line-of-sight. Afterwards, the marginal distributions of the orbital elements are analyzed in one and two dimensions. Based on this, a method for the identification of symmetric transformations of orbital elements is proposed. These symmetries are used to simplify the orbital elements distribution and reduce the orbital space to be explored by at least a factor of 2 for any system in consideration. Moreover, the application of the methodology to specific systems lead to reductions of the size of the orbital space to be explored of the order of 7 with confidence intervals of 99 %. Finally, it is analyzed how the errors in observations and the nature of the system (e.g high speed encounter) could affect the resultant distributions.

In chapter 4 we follow the work in the paper [3, 2] and partially reproduce, complement and add to their results. In short, using test particles and self-consistent

methods the orbital structure of a pair-interacting system is explored. For that, the possible configurations in time of the pair-interacting systems are modeled and tidal regions are identified. Based on this, a mapping from the tidal regions back to the initial conditions is proposed. We used this proposal to investigate how well the initial orientations of each galactic disk (a.k.a. spins) can be estimated. More specifically, we study the mapping from the tidal regions to the orientations for systems in which one disk is face-on (with zero $i = 0$) and the other one has any inclination but a given angle of periapsis $w = 0$. It is shown that when all the parameters are known (with the exception of the galactic spins) observations of the tidal features constrain the orientations of the galaxies to lie in a space of 3% the size in which the orientations were initially searched. Furthermore, additional statistical analysis of the systematic errors and random errors are made, such analysis lets us appreciate for example how such errors behave for different ground true disk orientations.

Chapter 2

Theoretical Framework

2.1 Introduction

In this chapter we present the background for constructing the orbital structure of interacting galaxies, limited naturally to the considerations in the present work; more general theoretical tools could be found in [24] and [25]. We first give a general overview of the type of objects we are about to study altogether with their relevant observational properties that help us test our model. Then, we pass to describe their dynamics under a series of approaches that help to refine the system interactions as well as to encompass everything from a statistical point of view. The following discussion is mainly based on the books [24], [25], [28], and [29].

2.2 Observations and galaxy morphology

In practical terms a galaxy can be defined as a gravitational bound system of stars, stellar remnants, interstellar gas, dust, and dark matter. Nevertheless, for some cases further distinctions must be made considering parameters as relaxation time and size [30]. Despite the complexity and generality of the definition provided, most observable galaxies can be categorized in a reduced number of types. A classification system for excellence is the Hubble one, since it connects well the physical properties that can be associated between systems and their observational appearance. The classification

is divided into Elliptical (10%), Spiral (60%), Irregular (10%), and Lenticular (20%).

2.2.1 Elliptical Galaxies

These are featureless stellar systems containing little or no cold gas, as well as a negligible disk. Their luminous matter is mainly composed of old stars which can be as old as the age of the universe. In the Hubble sequence they are classified by its "ellipticity", defined as $\epsilon = 1 - b/a$, where b and a (minor and major axis) are obtained from the isophotes of the galaxy image (see fig. 2-1). They are mainly composed of two components, an ellipsoid of baryonic matter and a dark matter halo.

Baryonic Ellipsoid

It has a surface brightness that follows a Sérsic profile, $\ln[I(R)/I(0)] = -kR^{1/n}$, where R represents the distance over the sky plane measured from the projected galaxy center. So, as we only see $I(R)$, it is impossible to determine directly whether elliptical galaxies are axisymmetric or triaxial; evidence strongly suggests that both types are present. In addition, baryonic matter has negligible rotation and its velocity dispersion σ is an important dynamical feature. The last one supports the structure of the galaxy and relates with the size and luminosity of the galaxy (see for example the fundamental plane).

Dark Matter Halo

It is a roughly spherical mass distribution, thought to follow a NFW profile, composed of dark matter, that is, non or weak electromagnetic interacting matter. It is proposed to explain features observed in galaxies. In this particular case, it helps to explain the kinematics of objects near the galaxy as nebulae, globular clusters, and satellite galaxies. It also helps to explain the emissivity and temperature distribution of hot gas (assumed in equilibrium) around the galaxy. Within uncertainties of at least a factor of two, the halos extend to $\approx 300\text{Kpc}$ and contain ≈ 10 times the mass in stars.

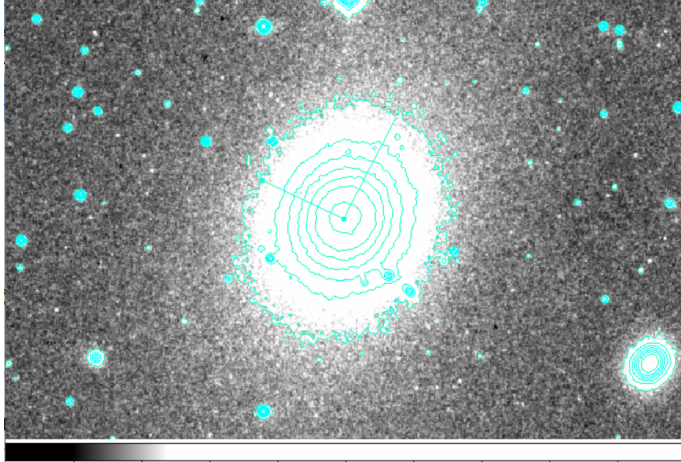


Figure 2-1: The image shows M87 and the blue curves found using ds9 are isophotes in the image. For example, with the second isophote (from the center) it is obtained $\epsilon = 0.0$; nevertheless when calculated from the most external one $\epsilon = 0.1$ is obtained. So, the galaxy could be taken as E0-1. This behaviour is natural for M87 since it is in the middle of a galactic cluster and therefore its outer parts are less virialized by the interactions with the other galaxies. The image is from the SDSS [31].

2.2.2 Spiral or Disk Galaxies

Although these galaxies owe their name to the presence of a prominent disk with spiral arms that contains the majority of stars, cold gas, and dust of the system, they are really composed of two additional components, the bulge and the Halo. These galaxies are named in the Hubble classification along the sequence Sa → Sd. In that same order they have characteristic relative bulge-disk ratio luminosities that decrease. This bulge-disk ratio luminosity decrease also correlates with spiral arms becoming more loosely wound, bluer color of the disk, increase in the relative mass of gas, and more clumpy spiral arms, where individual patches of young stars and HII became more prominent (see fig. 2-2).

Disk

Despite its arms (see M101 in fig. 2-2) are composed by young as well as old stars, the disk can be described as a distribution of matter with cylindrical symmetry, and with a height of about 5 percent of its radial size ($\approx 1 - 10\text{Kpc}$). From face-on observation it is observed that the surface brightness follows an exponential profile.

On the other hand, edge-on observations show that the matter in the disk follows near circular orbits (with speeds between $100 - 300 \text{ km s}^{-1}$). These observations together with equilibrium considerations help us to understand that in these galaxies the luminosity density decays exponentially in the vertical as well as in the radial directions. Measurements also permit us to classify a galaxy in the Hubble system depending on its velocity curve, and the last one helps us to study the visible and non-visible matter distribution around the disk. Additionally, the gas and dust also take an important part in the disk, since their gravitational and electromagnetic interactions also determine the galaxy structure and affect how it will evolve.

Bulge

It can be understood as a central ellipsoid region of the order of few Kpc, virialized and following the same profile as elliptical galaxies. It is mainly composed of old stars, and composed 2/3 of the time by an observable bar, which is thought to be fundamental for the formation of spiral arms. The observed bar is used in the Hubble classification, so that an Sa type with a bar will be identified as SBa.

Halo

It is the more massive component of the galaxy and encloses both the disk and the bulge. It is mainly composed of the stellar and the dark matter halo, both of them with size of some hundreds of Kpc. The first, consist of an ellipsoidal distribution of old stars in globular clusters and field stars whose perpendicular velocities are high. The second one, is equivalent to the description already made for elliptical galaxies, but in this case is additionally a fundamental component in order to explain the kinematics of stars in the disk, tidal features, as well as the equilibrium of disk galaxies.

In this work we will concentrate on spiral galaxies, precisely in chapter 4, because their richness in forms will permit us to talk more about the orbital structure for interacting systems. In some detail, we will analyze tidal regions.



(a) M101.



(b) M104.

Figure 2-2: M101 also known as the pinwheel galaxy is a SBc type galaxy as its little bulge and its loosely wound and clumpy spiral arms show, the B is a reminder that a bar (not very evident in this case) accompanies the bulge. On the other hand, M104 known as the Sombrero galaxy is an Sa type galaxy as its gigantic bulge and neat disk suggest. Images by the ESA/Hubble Space Telescope.

2.2.3 Lenticular and Irregular Galaxies

Lenticular galaxies are transition objects between spiral and elliptical galaxies. They contain a bulge, and sometimes a bar, besides a small and rapidly rotating disk which obeys the exponential surface-brightness law. Nevertheless, like ellipticals, they have little or no cool gas or recent star formation. They are also smooth and featureless in appearance and exhibit no spiral structure; they are classified as S(B)0.

Irregular types on the other hand, are galaxies that, as its name suggests, do not exhibit any regular patterns, so that in order to be described much information will be needed. In fact, in a classical sense we could say that its arrangement is chaotic in nature. They are classified as Irr in the Hubble system. On the other hand, although much of their luminosity is emitted by young stars and more than 30% our neighborhood galaxies are composed of this type, they are not usually found in catalogs since their low surface brightness introduces this observational bias.

2.3 Basic Dynamics and Kinematics

It has become natural to solve physics problems with sequences of approximations since it is procedure convenient and brings a lot of insight. Relevant examples are

functions as mathematical series, the interaction between a couple of bodies as point particles (e.g. planets), or the model of macroscopic systems from harmonic oscillators; only to give few.

The main approximations used in this work are: consider the system as a two body problem, evolve it as a N-body problem in which each point particle represents a set of particles, consideration of smooth potentials, non-collisional considerations, galaxies as underlying continuous phase distributions, the association of prior distributions for some parameters that characterize galactic collisions and how such parameters get affected by new information (e.g. observations).

In this section, the elements to consider two simple models are presented. First, galaxies as if they were punctual particles. The other one, in which each galaxy behaves as if it were isolated, but as a whole follows the orbit given by the two body approximation.

2.3.1 The Two Body Approximation

It refers to the fact that two extended systems sufficiently isolated and far from each other interact as an isolated pair of point particles. As a result, this approximation could give a first analytical guess to the orbit that a pair of galaxies follow in an encounter, especially in early stages. Based on this, each galaxy is considered as a punctual mass m_i ($i = 1$ or 2), where the total mass is $M_T = m_1 + m_2$, and each sub-index refers to a certain galaxy.

The analytical results of the approximation become clear by using the symmetries that the Lagrangian of the system exhibits as well as using certain coordinate systems in order to write the equations of motion. Doing a quick summary we first consider the Lagrangian in an inertial frame for two interacting galaxies under a two body approximation. Writing the position of each particle as $\mathbf{r}'_i = \mathbf{r}_i + \mathbf{R}$, where \mathbf{R} represents the center of mass, it is obtained that:

$$\mathcal{L} = \frac{1}{2} M_T \dot{\mathbf{R}}^2 + \frac{1}{2} (m_1 \dot{\mathbf{r}}_1^2 + m_2 \dot{\mathbf{r}}_2^2) - V(r) \quad (2.1)$$

Then, using the fact that \mathbf{R} is cyclic, the definition of \mathbf{r} ($\mathbf{r} \equiv \mathbf{r}_2 - \mathbf{r}_1$), the invariance under rotations, and writing down the gravitational potential explicitly, an equivalent Lagrangian is written in standard polar coordinates (θ, r) , in terms of the reduced mass $\mu = m_1 m_2 / (m_1 + m_2)$ and $k \equiv GM_T\mu \equiv G(m_1 + m_2)\mu$, as:

$$\mathcal{L} = \frac{1}{2} \frac{m_1 m_2}{m_1 + m_2} \dot{\mathbf{r}}^2 - V(r) = \frac{1}{2} \mu \dot{\mathbf{r}}^2 - \frac{GM_T\mu}{r} = \frac{1}{2} \mu [\dot{r}^2 + (\dot{\theta}r)^2] - \frac{k}{r} \quad (2.2)$$

Furthermore, given that θ is cyclical, that $\dot{\theta}$ and \dot{r} can be determined from the Lagrange equations and so $\frac{dr}{d\theta}$, the following results can be obtained:

$$\frac{\partial \mathcal{L}}{\partial \dot{\theta}} = \mu \dot{\theta} r^2 = L \quad (2.3)$$

$$r = \frac{a(1 - e^2)}{1 + \cos(\theta - \theta')} \quad (2.4)$$

$$\Delta t = \sqrt{\frac{\mu}{2}} \int_{r_0}^r \frac{dr}{\sqrt{E - V(r) - \frac{L^2}{2\mu r^2}}} = \begin{cases} \sqrt{\frac{ma^3}{k}} \int_0^\psi d\psi (1 - e \cos \psi) & \text{if } e < 1 \\ \sqrt{\frac{ma^3}{k}} \int_0^{\psi'} d\psi (e \cosh \psi - 1) & \text{if } e \geq 1 \end{cases} \quad (2.5)$$

Clearly in eq. 2.3 L is the magnitude of the angular momentum. Equation 2.4 encompasses the orbit geometry in its plane. Equation 2.5 permit us to solve the problem in time together with the use of the eccentricity e , the semi-major axis a , and the eccentric anomaly ψ or ψ' for the elliptical or hyperbolic case respectively; all this variables are defined by 2.6.

$$e = \sqrt{1 - \frac{L^2}{\mu k a}} \quad \frac{L^2}{\mu k} = a(1 - e^2) \quad (2.6a)$$

$$r = a(1 - e \cos \psi) \quad r = a(1 - e \cosh \psi') \quad (2.6b)$$

2.3.2 The Orbits of Stars and Potential Theory

Although this first approximation could tell us about the relative positions and velocities between galaxies (its centers of mass), under the assumption that they interact as point particles, it does not say anything about the dynamics of the particles inside each galaxy.

To overcome this problem, inspired in the observations of continuous profiles for the surface luminosity of galaxies as pointed out in 2.2, it could be thought that the mass density, $\rho(\mathbf{r})$, of each galaxy in the system is also a smooth continuous function. With this in mind we could write the potential, $\Phi(\mathbf{r})$, as follow and show that the Poisson equation is satisfied (v represents the volume of integration):

$$\Phi(\mathbf{r}) = -G \int_{v'} d^3\mathbf{r}' \frac{\rho(\mathbf{r}')}{|\mathbf{r} - \mathbf{r}'|} \quad \nabla^2 \Phi = 4\pi G \rho \quad (2.7)$$

Forthwith, the Lagrangian describing the dynamics of each point particle (star or set of them) with total mass m and position vector \mathbf{r} respect the center of mass of its host galaxy would be given by:

$$\mathcal{L} = \frac{1}{2} m \dot{\mathbf{r}}^2 - m\Phi(\mathbf{r}) \quad (2.8)$$

This means that although each galaxy is composed of stars and other point-like interacting particles, we are neglecting the forces from individual particles and considering only the large-scale force from the overall mass distribution, which is made up of millions of stars. In other words, gravitational fields of galaxies are smooth, neglecting small-scale irregularities due to individual stars or larger objects like globular clusters or molecular clouds.

It is important to point out that the Lagrangian form obtained in eq. 2.8 could be easily constrained to obtain the one of the two body problem (see 2.2), so that the fascinating interpretations in the case of a spherical symmetric potential can be readily applied to the two body problem, with the natural caveat that to talk about

the actual coordinates the holonomic constraints of the problem must be used.

Now, to model the motion of stars a form must be given to the potential in eq. 2.8 and the equations of movement must be derived and integrated. For the present study the spherical and axial symmetric potentials are the ones that arouse interest, since with them models for elliptical and spiral galaxies can be constructed. In fact, the functional form of such potentials is fundamental for the initialization of the positions of the galaxies in an early stage. So, we pass to explain how such potentials could be justified. Additionally, under further considerations they will also be fundamental to initialize the velocity distributions and evolve the systems under a collisionless formalism.

Spherical symmetry

For this type of systems the orbit equation for each particle can be easily obtained from 2.8. So, considering an inertial frame in the center of mass of the system, the spherical symmetry, the conservation of the angular momentum, standard polar coordinates (r, θ) , and with the change of variables $1/r = u$ it is obtained that:

$$\frac{d^2u}{d\theta^2} + u = -\frac{m}{L^2} \frac{d}{du} \Phi\left(\frac{1}{u}\right) \quad (2.9)$$

In addition to model orbits by directly replacing Φ in equation 2.9, we could solve for turning points, show symmetries in a coordinate change as θ to $-\theta$, and understand rather restrictive dynamics in some cases (e.g. integrability only for certain potentials; in the case $\Phi \propto r^{n+1}$ they can be classified by n).

So, a concrete orbit is obtained for eq. 2.9 by using Poisson eq. 2.7 and considering two parameter density models given by eq. 2.10. This family of functions lead to important and standard density profiles. For example, the Hernquist profile ($\alpha = 1, \beta = 4$) allow us to model the bulge of a spiral galaxy, so that, when projected as a luminosity surface density under a constant mass to light ratio it resembles the Vaucouleurs profile mentioned in 2.2. In addition, the NFW profile ($\alpha = 1, \beta = 3$)

permits us to model the galactic halo, giving sense to the circular velocities observed for disk stars and the profile obtained by modeling dark matter halos formation and evolution [32].

$$\rho = \frac{\rho_0}{(r/a)^\alpha (1+r/a)^{(\beta-\alpha)}} \quad (2.10)$$

Axial symmetric

In a simple but working approximation, galactic disks can be modeled with axially symmetric mass distributions. This of course has the advantage that the angular momentum conservation reduces the dimensionality of the problem when the inertial system is considered cylindrical, located at the center of mass of the galaxy and z is measured along the axis of symmetry. A widely used approximation for a variety of problems is to consider the orbit of each star around equilibrium, that is, in a quasi-circular orbit. With this, the equations of motion in terms of the axially symmetric potential $\Phi(R, z)$ for a particle due to a galactic disk can be written as:

$$\ddot{x} = -\kappa^2 x \quad \ddot{z} = -\nu^2 z \quad (2.11)$$

where the equilibrium points, the definition of x as well as the radial and vertical frequencies (κ and ν) are given by (all in respective order):

$$\frac{L_z^2}{R^3} = \left(\frac{\partial \Phi_{eff}}{\partial R} \right)_{(R_g, 0)} \quad 0 = \frac{\partial \Phi}{\partial z} \quad x = R - R_g \quad (2.12)$$

$$\kappa^2 = \frac{\partial^2 \Phi_{eff}}{\partial R^2} \quad \nu^2 = \frac{\partial^2 \Phi_{eff}}{\partial z^2} \quad \Phi_{eff} = \Phi(R, z) + \frac{L_z^2}{2R^2} \quad (2.13)$$

This is the approximation used to initialize the motion of particles in a galactic disk (used in chapter 4). More generally, the equations of movement for the particles in a disk inside a galaxy must be found from eq. 2.8 considering the contribution to the potential from the disk (as just shown), the bulge, and the dark matter halo,

where the last two are obtained as specified in the spherical symmetry section. The contribution to the potential from the disk is the result of considering the disk as the sum of infinitesimal thin disks as we are about to show.

The potential of an infinitesimal thin disk given by eq. 2.14. This potential is the result of summing the contribution of thin oblate spheroids of homogeneous surface density $\Sigma_0(a)$, with semi-axis a and c such that $a \gg c$. What is remarkable of eq. 2.14 is that $\Sigma_0(a)$ can be written in terms of a razor-thin disk of known surface density $\Sigma(R)$; $\Sigma_0(a)$ correspond to the derivatived right inner integral.

$$\Phi'(R, z) = 4G \int_0^\infty da \sin^{-1} \left(\frac{2}{\sqrt{+} + \sqrt{-}} \right) \frac{d}{da} \int_a^\infty dR' \frac{R' \Sigma(R')}{\sqrt{R'^2 - a^2}} \quad (2.14)$$

where

$$\sqrt{\pm} = \sqrt{z^2 + (a \pm R)^2} \quad (2.15)$$

So, with a suitable surface density for the disk, as the exponential one supported by observations (see 2.2), we can finally compute the potential of a thin disk with eq. 2.14. Nevertheless, disks have a vertical structure. So, to construct a more realistic model, it is considered that at every z' we have a razor exponential thin disk (with radial scale a_d) that contributes at every z a potential $dz' \Phi'(R, z - z') \xi(z')$, where ξ weight the contribution of each thin disk and is called vertical scale. Therefore, we can sum all the contributions using eq. 2.16; note however that in $\sqrt{\pm}$, z must be replaced by $z - z'$

$$\Phi(R, z) = -\frac{4G\Sigma_0}{R_d} \int_{-\infty}^\infty dz \xi(z) \int_0^\infty da \sin^{-1} \left(\frac{2}{\sqrt{+} + \sqrt{-}} \right) a K_0(a/a_d) \quad (2.16)$$

Finally, the fact that each galaxy can be considered with its particles moving as if were isolated (with the potentials mentioned) while they follow the two body orbit (in early stages) can be understood by the separable nature of the total Lagrangian

of both galaxy $L = L_{\text{two-body}} + L_{\text{particles-inside-galaxy1}} + L_{\text{particles-inside-galaxy2}}$. This naturally follows from the fact that the magnitude of the relative vector between galaxies, \mathbf{r} , is much greater than the radial scale of the halo that contains the galaxy. That is, $|\mathbf{r}| = |\mathbf{r}_1 - \mathbf{r}_2| \gg a_h > R_d > z_d$, where a_h represents the dark matter halo scale of the galaxy and z_d the vertical scale of the disk.

2.4 Collisionless Systems

So far we have proposed a model in which each galaxy behaves as if it were isolated, in the sense that each star moves with respect to its galaxy center of mass according to the potential of the former one. However, when considering a collision, we regard that galaxies follow the orbit given by the two body approximation. For all that, we developed the two body approximation and proposed the smooth potentials, justified empirically by the fact that observations in the projected density or circular velocity could be reconstructed.

Nevertheless, the admission of smooth potentials, its implications and limitations can be analyzed from a more fundamental and general point of view, that is, under a collisionless formalism. This is clear from the proper definition of collisionless system: one in which any forces encountered by the particles must be conservative and smooth. In the present work this formalism will also permit us to understand the equilibrium state of galaxies and reconstruct the possible mechanical states of an isolated galaxy, taking into account its discrete nature. Toward this end let us first examine the physical meaning of a profile.

2.4.1 Galactic Profiles as Distribution Functions

If we are faced with $\rho(\mathbf{r})$ or any other profile, we must be capable of interpreting it in the light of the discrete nature of galaxies. In fact, the representation of a galaxy by infinitesimal small masses all over space is rather unsatisfactory. This is evident by the distances separating stars of the order of a few *pc*. Furthermore, since the infinite number of particles implied such representation (the infinitesimal small masses all

over space) alone would not suggest a relevant use of N-body methodologies. In short, it must be analyzed how from continuous profiles the discrete nature in these system will be explained.

In principle, a direct interpretation could be tried to be established in analogy with the construction of a density in the case of continuum mechanics. Nevertheless, this interpretation can lead to poor estimations of the density. The answer to the problem relies on interpreting a profile as a probability distribution function.

This view is well justified as a limiting case of Liouville's Theorem, which establishes that in an isolated Hamiltonian system the density of points representing particles in the phase space is conserved as they propagate through their trajectories and that therefore:

$$\frac{df}{dt}(\mathbf{q}, \mathbf{p}) = 0 \quad (2.17)$$

where (\mathbf{q}, \mathbf{p}) represent the possible position and momentum of a particle in the system and f is the density of such points in a phase-space volume. In other words, f is the probability distribution of the phase-space variables without normalization. Therefore, the density, in the special case of particles with the same mass, can be written as a simple marginalization of f :

$$\rho(\mathbf{q}) = m \int_0^\infty f(\mathbf{q}, \mathbf{p}) d^3 \mathbf{p} \quad (2.18)$$

This allows to write $dN = \rho/m dV$, where N is the number of particles, so that with a rejection sampling would be straightforward to spatially realize these systems numerically. Similar procedures will be illustrated later for the velocities and will be used extensively in chapter 4 for the construction of extended systems.

2.4.2 Justification of Collisionless Nature

Before proceeding to other fundamental considerations for the present work, we first formally justify Liouville's Theorem for a galaxy from an insightful point of view.

Louisville's Theorem requires that any forces encountered by the particles must be

conservative and smooth. In other words, forces must not change the total energies of the particles nor can they be abrupt forces such as those arising from collisions.

Therefore, the collisionless nature of galaxies should be explained by calculating how much time it takes for a star to interact with the others in order for dispersive encounters to change its kinetic energy in the same quantity of its initial value, and then observing that the resultant time is much larger than the age of the galaxy.

For that, an overestimation in the importance of encounters is made. We consider that each time a star crosses the system, for example completes an orbit, it has a considerable encounter with the other stars. This over estimation is well justified by the fact that the number of direct encounters is $2\pi R(2R_\odot)^2 n \approx 10^{-19}$. Even if we consider that the gravitational effect increase the impact parameter, $2R_\odot$, it must be under a weak field interaction (see Fig. 2-3) since the ratio of the potential energy between two given particles respect their total kinetic energy is of the order of 10^{-8} . This last point becomes clear when writing the Lagrangian of such pair of particles $\mathcal{L} = K + U$ and realizing that U slightly perturbs the Lagrangian value. So, considering the impact parameter as $b = 2Gm/v^2$, that is, the minimum impact parameter in a weak field approximation and consider a number density of 10^9Kpc^{-2} in the interaction, the resultant number of collisions are of still of the order of 10^{-3} .

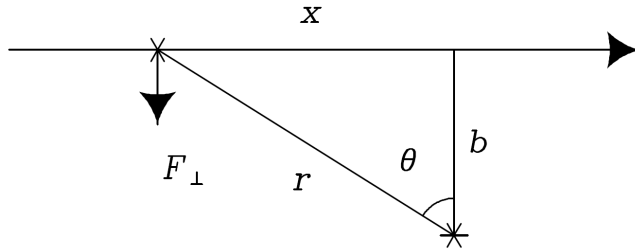


Figure 2-3: The collision takes place under a weak field interaction, which means that the impulse caused by one encounter can be calculated by considering that the momentum only changes along the vector connecting both particles when they are at the minimum distance b (impact parameter). The image illustrates the direction x in which the momentum remains unchanged and the force F_{\perp} in which the momentum changes. Image taken from Binney [24].

So, in each crossing the change that will be made in the velocity over the star that travels horizontally near another can be calculated as (see fig. 2-3) :

$$\delta v = \frac{1}{m} \int_{-\infty}^{\infty} dt \frac{1}{[1 + (vt/b)^2]^{3/2}} = \frac{2Gm}{bv} \quad (2.19)$$

Therefore, we can write the "total change" in the kinetic energy by adding the changes due to the interactions at all the impact parameters b :

$$\Delta v^2 = \int_{b_{min}}^{b_{max}} dn(b) \delta v^2(b) \quad (2.20)$$

where b_{min} is the impact parameter that causes $\delta v = v$ in a dispersive collision, $b_{max} = R$, and the number of stars in $(b, b + db)$ is $dn = 2\pi b N / (\pi R^2) db$, where R is the galaxy's radius and N the total number of stars. So, for velocities in the keplerian regime we would obtain that the time for the system to change thanks to dispersion effects would be:

$$t_{relax} = t_{cross} * \frac{v}{\Delta v} \approx \frac{0.1N}{\ln N} t_{cross} \quad (2.21)$$

where t_{cross} is the time that takes the start to cross the system once. With this in mind it is easy to see that a relaxation time for a galaxy at the sun's location for example would be larger than the age of the universe, also, this is the case for almost all the regions except near the center where collisions are important. So, collisions are unimportant and it is suitable to propose a smooth potential to model the dynamics of the system. With the fact that this potential is gravitational, it becomes evident that Liouville's Theorem is satisfied.

2.4.3 Jeans Equations

Now that we know that a galaxy is collisionless, what information could we obtain from this? With the considerations done until now we could write eq. 2.17, with a smooth potential Φ , as eq. 2.22. This expression, also known as the Boltzmann equation, describes the evolution of a system in phase-space through the evolution of the distribution function f .

$$\frac{\partial f}{\partial t} + \frac{\mathbf{p}}{m} \cdot \frac{\partial f}{\partial \mathbf{q}} - m \frac{\partial \Phi}{\partial \mathbf{q}} \cdot \frac{\partial f}{\partial \mathbf{p}} = 0 \quad (2.22)$$

The solution of this seven variable differential problem is usually very difficult. However, valuable expressions are obtained by taking the distribution function moments of f . That is, integrating eq. 2.22 in the \mathbf{v} space directly or after multiplying by v_j and considering the moments of the distribution $\langle v_i^m v_j^n \rangle$ with m and n between 0 a 2 along with the dispersion velocity tensor given by $\sigma_{ij}^2 = \langle v_i v_j \rangle - \langle v_i \rangle \langle v_j \rangle$ we could write:

$$\frac{\partial \rho}{\partial t} + \frac{\partial(\rho \bar{v}_i)}{\partial x_i} = 0 \quad (2.23a)$$

$$\frac{\partial \bar{v}_j}{\partial t} + \bar{v}_i \frac{\partial \bar{v}_j}{\partial x_i} = \frac{\partial \Phi}{\partial x_j} - \frac{1}{\rho} \frac{\partial(\rho \sigma_{ij})}{\partial x_i} = 0 \quad (2.23b)$$

where repeated indices imply summation. We clearly see a continuity equation and one very similar to the Euler's equation; these 4 equations give relationships between the moments of f . It is interesting to note that the second one permits us to say that the mean velocities in a galaxy are the result of the potential as well as the dispersion of velocities. Therefore, with these equations we gain insight and could begin to approximate to f using a distribution that shares some of its momentum up to order 2. This is specially useful for the case of the velocity distribution in the disk together with the fact that the spatial density is already known to a good degree

More information can be obtained from these equations when analyzed in a given system of coordinates. For instance, in chapter 4 the considerations of eq. 3.1 in an axial-symmetric case permits us to justify the vertical structure for a disk.

The Moments Approximation

The use of the moments of the distribution as fundamental properties that characterize the distribution itself becomes totally clear writing the distribution in its Fourier representation; a two dimensional example is illustrated in eq. 2.24. So, we could

approximate the Fourier transform and go back to the phase-space by the inverse Fourier transform.

$$\mathcal{L}(f) = m \int_0^\infty e^{i(k,h)\cdot(x,p)} f(x, p) dx dp = \sum_{m,n=0,0}^{\infty,\infty} i^{m+n} \langle x^m p^n \rangle \frac{k^m}{m!} \frac{h^n}{n!} \quad (2.24)$$

The velocity distribution in the disk is described with this approximation in mind and the satisfaction of eq. 3.1. In addition, more sophisticated methodologies will be illustrated. For example, in chapter 4 we will show a possible mapping between tidal regions (regions of marginal distributions of f) and possible initial mechanical states for the galaxies.

2.4.4 Stationary solutions and angle-action variables

It is clear that the form of equation 2.22 is that of a constant of motion. In fact, this also tells us that any function only of integrals of motion would also be a solution to the Boltzmann collisionless equation (steady case) since any term in the summation in equation 2.25 is equal 0. So, it becomes a motivation to write the f depending on isolating integrals, which in turn depend on (\mathbf{q}, \mathbf{p}) ; we conveniently choose from now on $(\mathbf{q}, \mathbf{p})=(\mathbf{x}, \mathbf{v})$ thanks to its direct physical interpretation.

$$\frac{d}{dt} f[I_1(\mathbf{x}, \mathbf{v}), \dots, I_n(\mathbf{x}, \mathbf{v})] = \sum_{m=1}^n \frac{\partial f}{\partial I_m} \frac{dI_m}{dt} = 0 \quad (2.25)$$

Nevertheless, it is sometimes the case that non-isolating integrals are obtained for a system. So, in order to address the problem special cases are considered, in which angle-action variables can be chosen such that the orbits of the system have in fact isolating integrals. More formally, this is the statement of the strong Jeans theorem: the distribution function (DF) of a steady-state stellar system in which almost all orbits are regular with non-resonant frequencies may be presumed to be a function only of three independent isolating integrals, which may be taken to be the actions. This is taken into account in order to construct the initial configuration of

the spherical components of galaxies as will be refereed in further detail in chapter 4.

2.5 Collisions and Encounters of Stellar Systems

So far we have considered weak interactions between two galaxies as the two body approximation, we have shortly described their stellar orbits, and considered the probability distributions of the stars as if each galaxy were sufficiently isolated.

Nevertheless, galaxies are formed within a hierarchical model, which propose that they are formed thanks to the mergers that constantly happen, and that principal features such as stripping material, rings, accelerated star formation and others can be explained from encounters. Therefore, in order to correctly describe the orbital structure in galactic mergers, the physical mechanisms present in them must be taken into account. These mechanisms are useful in the present work since they are used to construct consistent initial mechanical states and computational simulations.

2.5.1 The Fokker-Plank Equation and Dynamical Friction

When two systems collide there is a systematic transfer of energy from the relative orbit motion into random motion of their constituent particles. This begins when the two dark halos of the galaxies start to merge and the baryon-rich central regions spiral towards the center of the merged halo, where they in turn merge. This process is generally known as orbital decay and we demand it for the simulations in chapter 4. The orbital decay is explained by dynamical friction. The last one can be seen as a consequence of the Fokker-Plank equation, which simply refers to the correction, $\Gamma[f]$ needed for the collisionless Boltzmann equation (see 2.26).

$$\frac{df(\mathbf{x}, \mathbf{v})}{dt} = \Gamma[f(\mathbf{x}, \mathbf{v})] \quad (2.26)$$

More concretely, considering that the analysis of hyperbolic collisions between an arbitrary chosen star of a galaxy (labeled subject star, with mass m) with the rest of the stars, known as field stars (with mass m_a), mostly explain the successive change in

the structure of the system, we can rewrite equation 2.26 as 2.27a - 2.27c; the subindex a is also used for the phase-space coordinates of field stars. This result is often referred as the Fokker-Plank approximation for local encounters and the quantities $D[v_i]$ and $D[v_i v_j]$ are called diffusion coefficients and denote the expectation of the change in $v_i(\mathbf{x}, \mathbf{v})$ and $v_i v_j(\mathbf{x}, \mathbf{v})$ per unit time respectively.

$$\frac{df}{dt} \approx - \sum_{i=1}^3 \frac{\partial}{\partial v_i} \{D[v_i]f(\mathbf{x}, \mathbf{v})\} + \frac{1}{2} \sum_{i,j=1}^3 \frac{\partial^2}{\partial v_i \partial v_j} \{D[v_i v_j]f(\mathbf{x}, \mathbf{v})\} \quad (2.27a)$$

$$D[v_i] = 4\pi G^2 m_a (m_a + m) \ln \Lambda \frac{\partial}{\partial v_i} \int d^3 \mathbf{v}_a \frac{f_a(\mathbf{x}, \mathbf{v}_a)}{|\mathbf{v} - \mathbf{v}_a|} \quad (2.27b)$$

$$D[v_i v_j] = 4\pi G^2 m_a^2 \ln \Lambda \frac{\partial^2}{\partial v_j \partial v_i} \int d^3 \mathbf{v}_a f_a(\mathbf{x}, \mathbf{v}_a) |\mathbf{v} - \mathbf{v}_a| \quad (2.27c)$$

$$\Lambda = \frac{b_{max} v_{typ}}{G(m + m_a)} \quad (2.27d)$$

This set of equations are fundamental because they give useful analytical approaches to study collisions of stellar systems under sufficiently weak encounters. Of interest here eq. 2.27b and eq. 2.27c make evident the orbital decay and permit us to make estimations for its time. For instance, in a minor merger f represents the DF, f_a the DF of the major galaxy, and $|D[\mathbf{v}_i]|$ is much larger than $D[v_i v_j]$, and then $D[\mathbf{v}_i]$ can be understood as a friction that oppose the movement of each star at (\mathbf{x}, \mathbf{v}) of the satellite galaxy.

2.5.2 Tidal forces

Another important effect that plays a fundamental role is that of tidal forces. Nevertheless, in contrast with the last section, tidal forces permit us to talk more intuitively about how interacting galaxies could lose mass and limit their sizes as they interact. For instance, a static tidal field prunes distant stars from the satellite system, thereby enforcing an upper limit on its size and mass. An example per excellence of these streams of material in interacting galaxies is NGC 4676 (see fig. 2-4).

To consider tidal forces, two complementary theoretical approaches are considered.



Figure 2-4: NGC 4676 is known as the Mice thanks to its elongated tails, that is, the elongated and thin regions of stars and interstellar gas that extends into space from the galaxies. Tidal tails have been likely formed because the galaxies passed through each other and tidal forces took place. Image by the ESA/Hubble Space Telescope.

The restricted three-body problem and the sheared-sheet approximation. Both of them permit us to approximate the maximum extent of each galaxy as well as to consider the movement of the striped material. Here we will arbitrarily consider the restricted three-body approximation; as a comment it is valuable to add that the motion of the striped material can be even clearer under the consideration of angle-action variables.

Restricted Three Body Approximation

In this scenario, both galaxies are approximated as point masses and move within a circular orbit of radii R_0 . It is intended to find the trajectory of a massless test particle (usually the most external particles that belong to each galaxy) that orbits in the combined gravitational field of these two masses. When this is considered under a coordinate system positioned on the center of mass that rotates at the angular speed of the orbit between the galaxies, the tidal field is stationary. So, using this approximation the last closed zero-velocity surfaces surrounding a single body can be readily

used to estimate the maximum extent of each galaxy; this surface is characterized by the Hill radius given by equation 2.28.

$$r_{J(1,2)} = \left(\frac{m_{(1,2)}}{3m_{(2,1)}} \right)^{1/3} R_0 \quad (2.28)$$

where R_0 is the separation between both galaxies and the sub-indexes in parenthesis collect the expressions for both hill radius, this index refers to a certain galaxy. A better estimate is obtained recognizing that the effect of tidal fields on satellites in non-circular orbits is intermediate between tidal radii (a concept that applies to circular orbits) and tidal shocks (which apply to high-velocity or plunging orbits). In chapter 3, we use these considerations to estimate the maximum periapsis between the galaxies in an early (about to interacting) stage. Moreover, these considerations allow us to expect tidal features in certain simulations at certain distances. In fact, it has been found by numerical experiments that the tidal features in pairs of interacting galaxy systems can be greatly explained by the interaction of the disk of each galaxy with the respective galactic halos; this will be used in chapter 4.

2.5.3 Nth Body Algorithms

So far the considerations about how to build the mechanical states of galaxies in an early stage have been made, that is, when they are far from each other such that each galaxy can be considered as isolated. With this we could reconstruct an initial mechanical state of the system, and then evolve it with the use of eq. 2.7 and the Euler equations from 2.8. Nevertheless, distribution functions with lower symmetry systems (as triaxial or time dependent as in a collision) have non analytical distribution functions, this fact justify the computational methodologies as a necessity in a merger.

As a result, computational methods that follow the motion of a large number of masses under their mutual gravitational attraction are developed. Nevertheless, these methods have several complications. It is clear that to carry out simulations with all the particles in a galaxy is not feasible. For example, our galaxy has on the order of

10^{11} stars and $10^{69} GeV/(mc^2)$ dark matter particles of mass m . On the other hand, model a galaxy with less particles, suppose that we are representing the evolution of all the population given a sample and therefore statistical noise as well as collisions become concerns.

As a consequence, the methods normally used have considerable levels of sophistication. On the one hand, calculating the forces between particles in an effective way is fundamental. Moreover, depending on the characteristics that we desire to reproduce in the system different integration methods for the equations of motion can be used. A good example to illustrate both points is the use of orbit average methodologies to solve the Fokker-Plank equation.

For the present work, a N-body collisionless methodology is used. In this one a given particle represents a set of particles of the system and the potential is modified to avoid unreal collisions between sets of particles. In addition, the force is calculated using a tree code algorithm and a symplectic method is used for the integration in order to conserve energy. An important reason to choose this methodology is the fact that tidal features as well as orbital decay can be reproduced. More details and further discussion will be given in chapter 4.

Chapter 3

Orbital Structure of Galactic Pair Mergers in Early Stages

Abstract

In this chapter the orbital structure, defined as the organization of the mechanical state information given the observations, for a pair of interacting galaxies is investigated. For that, the evolution in an early stage is treated as a two-body problem. Therefore, reducing the orbital structure to the knowledge of the orbital elements. Then, based on justified priors for the orbital elements, Monte Carlo methods, and observational data, a posterior distribution for the orbital elements is constructed. Namely, the observations are the centers of the galaxies in the sky plane and their velocities along the line of sight. Afterwards, the one and two dimensional posterior distributions of the orbital elements are analyzed and important results as the partial characterization of the interacting nature of the system are obtained. Then, a method for the identification of symmetric transformations of orbital parameters is proposed. These symmetries are used to simplify orbital element distribution and reduce the orbital space size to be explored by at least a factor of 2 for any system in consideration. Moreover, the application of the methodology to specific systems leads to reductions of the orbital space to be explored of the order of 7 with confidence intervals of 99 %. Finally, it is analyzed how the errors in observations and the nature of the system (e.g high speed encounter) could affect the resultant distributions, for which it is found that several important characteristics in the orbital structure are conserved.

The early stages of a galactic collision are one of the most fundamental moments since a good approximation of the system through analytical procedures is still possible. As a result, collisions between galaxies are often modeled from these stages. This means that the set of parameters that characterize these initial states are ex-

plored based on computational simulations towards the possible final states of the system, where the last mechanical state is chosen based on the similarity between the predicted observations and the actual observations of the system.

Therefore, methodologies to reconstruct the mechanical state of a merger are computationally expensive and several key practices are used to reduce the computational effort. One fundamental step is the use of astrophysical arguments to estimate several critical parameters. An important set of them are the orbital parameters (see fig. 3-1) since they permit us to approximate the trajectories that the centers of mass of the galaxies follow. Orbital elements estimates are typically used by more complex procedures to refine the final estimate of the initial mechanical state. An illustrative example is the evolution from several possible initial mechanical states with the use of test particles and rigid galaxy potentials; partial reproduction of observations here permits to rule out options. As a last step one or several fully self-consistent simulations are used to refine the final model.

As a consequence of this well justified process [3], it is seen that the estimation of the possible initial orbital elements have an important place. In this chapter we develop and test a methodology for the estimation of such orbital elements from the observation of an early stage interacting system. More concretely, the system is supposed to interact under a two body approximation and the observations are the positions in the plane of the sky and velocities along the line of sight of the galaxies.

3.1 Orbital Structure

The problem of determining the orbital parameters in an early stage is an ill posed problem, in the sense that there is no unique solution for a given set of incomplete observations; this is clarified in detail in 3.1.1. Additionally, some orbital elements can be more probable, for example high relative velocities along the line of sight between galaxies could imply higher eccentricities. Hence, a significant statistical estimation of the density probability of the orbital elements given the observations is needed. We will name this distribution the orbital structure of the system.

As it was mentioned before, the orbital structure of early interacting galactic pairs is intended to be described under a two body approximation. For this reason, the orbital elements as a meaningful set of coordinates that capture all the possible states has been implicitly chosen. This selection has to do with the fact that they completely characterize the mechanical state of a two body problem and characterize the geometry of the orbit (see Fig. 3-1). In addition, in contrast to the relative position and velocities, the orbital elements (with the exception of the true anomaly ν) are constant under a two body approximation (see section 2.3.1).

3.1.1 Orbital elements and state vector connection

Based on the above, a natural procedure will be to analyze the mapping from the observational relative state vector (\mathbf{r}_{sky} , \mathbf{v}_{sky}) (positions and velocities measured from Earth) to the orbital parameters. We have:

$$\mathbf{h} = \mathbf{v}_{sky} \times \mathbf{r}_{sky} \quad \mathbf{n} = \hat{\mathbf{k}} \times \mathbf{v}_{sky} \quad (3.1a)$$

$$\mathbf{e} = \left(\frac{v_{sky}^2}{\mu} - \frac{1}{r_{sky}} \right) \mathbf{r}_{sky} - \frac{\mathbf{v}_{sky} \cdot \mathbf{r}_{sky}}{\mu} \mathbf{v}_{sky} \quad \cos \omega = \frac{\mathbf{n} \cdot \mathbf{e}}{n e} \quad (3.1b)$$

$$\cos i = \frac{h_z}{h} \quad \cos \Omega = \frac{n_x}{n} \quad (3.1c)$$

where $\mu = m_1 m_2 / (m_1 + m_2)$ is the reduced mass, \mathbf{h} is the specific angular momentum, and \mathbf{n} is called the node vector. The other parameters are explained in fig 3-1. Additionally, it must be noted that simple conditionals must be used for a proper interpretation of the results of ω , i , and Ω .

From the above equations it is easily noted that we have a set of transcendental equations to solve for the orbital elements given an incomplete set of observations as x_{sky} , y_{sky} , and $v_{z,sky}$; which are the observations that can be usually obtained. So, thanks to the implicit function theorem (with the exception of the values in which $(r_{sky}, v_{sky}) = (0, 0)$), we could write all the orbital elements in terms of only three of them and the respective observations. In order to solve these equations we followed

a Montecarlo procedure, which is the subject of the next section.

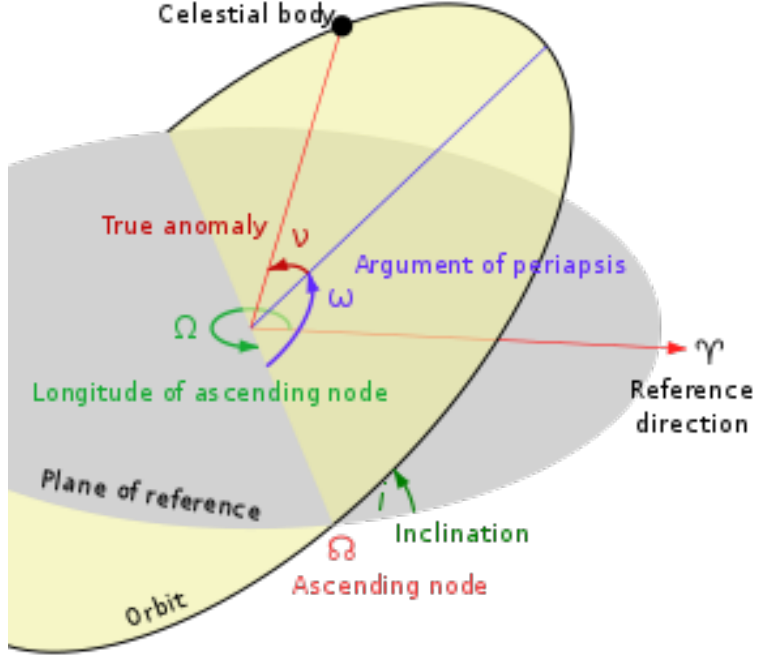


Figure 3-1: Geometric representation of the orbital parameters. In the present case the plane of reference is the plane of the sky. In the picture, the periapsis q , defined as the closest distance attained in the orbit between both galaxies, is the length of the purple oriented segment. The argument of periapsis, ω , is the angle between the sky plane and the purple segment. The true anomaly, ν , is the angle measured from the purple segment in the direction of the angular momentum of the system. The inclination, i , is the angle between the sky plane and the plane of the orbit. The longitude of the ascending node, Ω , is the angle between the intersection of the plane orbits and a direction of reference in the plane of the sky; this one is clarified for each specific case. Finally, the eccentricity, e , gives the shape of the orbit, characterizing circles, ellipses, parabolas, and hyperbolas as it increases. Lasunnty via Wikimedia Commons.

3.2 Orbital Structure Construction

In short, to find the orbital structure we sampled orbital elements from a prior distribution and then obtain the possible set of state vectors $(\mathbf{r}_{sky}, \mathbf{v}_{sky})$ associated with such samples. Then, we will only accept the orbital elements that reproduce the observations.

Let us first illustrate the mapping from the orbital elements to $\mathbf{w} = (\mathbf{r}_{sky}, \mathbf{v}_{sky})$. In virtue of the two body problem, the position of the orbital plane could be chosen to be:

$$\mathbf{r}_{plane} = \frac{(1+e)q}{1+e\cos\nu}(\cos\nu, \sin\nu, 0) \quad (3.2)$$

$$\mathbf{v}_{plane} = \sqrt{\frac{\mu}{q(1+e)}}(-\sin\nu, e+\cos\nu, 0) \quad (3.3)$$

where q , e , ν , and $\mu = m_1m_2/(m_1 + m_2)$ state for the periapsis, eccentricity, true anomaly, and reduced mass (see fig. 3-1). So, using the Euler angles ω , i , and Ω as in fig. 3-1 we can write the observational state vector, that is, the relative positions and velocities in the plane of the sky as:

$$\mathbf{w} = (\mathbf{r}_{sky}, \mathbf{v}_{sky}) = R_z(\omega)R_x(i)R_z(\Omega)(\mathbf{r}_{plane}, \mathbf{v}_{plane}) \quad (3.4)$$

3.2.1 Priors

Now, to reconstruct the possible state vectors \mathbf{w} we must assume some justified priors for the orbital elements. A good prior for the Euler angles could be the distribution of them for an arbitrary interacting pair system in the sky. For this we could argue in favor of the isotropy of the universe at large scales. The fact that any angle would be more probable in its distribution will imply a preference direction; characterized by a majority of the systems oriented in such a direction. As a result, we propose uniform distributions for the Euler angles. On the other hand, the other parameters are related to the physical properties of the system itself. So, only assuming their existence can be considered to follow uniform distributions since any threesome will be equivalent. This rather arbitrary consideration, known as the principle of transformation groups, can be perhaps best justified. This assumption could let us identify more easily symmetries between regions of orbital elements since the unique thing that makes such regions different is their range.

With this in mind we pass to justify the ranges for these distributions. It is clear

that for ω , ν and Ω the values go from 0 to 2π , while i goes from 0 to π . On the other hand, for q the minimum can be 0, since in fact a collision along a line is possible. Similarly, e has a minimum 0 since a circular orbit is possible. For the upper bounds of q and e we proceed as follows:

For the maximum value of q we demand that some of the outer particles in a dark matter halo of at least one galaxy experience a considerable interaction with the other galaxy. The outermost particles are considered to be at the virial radius of the dark matter halo since the lack of viralization is a signal of interaction. Furthermore, a considerable interaction means that there is an outer particle equally bound to both galaxies. Since the spherical symmetry of the dark matter distributions, the most affected particle will likely be along the line passing through the centers of mass of both haloes and in the periapsis. With this in mind we proceed analogously to section 3 of [33]. In it, it is exposed how to calculate the size of a star cluster depending on its periapsis distance with respect to its host galaxy. We use this in the inverse sense since we know the maximum size for our galaxies (virial radius). Then, it is found that the maximum pericentre distance is given by eq. 3.5. Where is important to note that eq. 3.5 really refers to two equations, where the indexes 1 and 2 simply help us to refer to either halo, and $q_{max,i}$ is the distance obtained between galaxies when the i -th halo is the one with the outermost particles affected at its virial radius $R_{200,i}$. Nevertheless, $q_{max,i}$ can be refereed as an overestimation since the mass densities of the dark matter halos could have previously interacted with each other causing considerable orbital decay and therefore a smaller periapsis. Finally, we do $e \approx 1$ in 3.5 in agreement with the arguments that will be presented in the next paragraph and do $q_{max} = \text{Max}[q_{max,1}, q_{max,2}]$ in consistency with the fact that it is enough that some of the outer particle of one Halo are affected.

$$q_{max,(1,2)} = R_{200,(1,2)} \left(\frac{(3+e)M_{(2,1)}}{M_{(1,2)}} \right)^{1/3} = R_{200,(1,2)} \left(\frac{4M_{(2,1)}}{M_{(1,2)}} \right)^{1/3} \quad (3.5)$$

Cosmological simulations [3] supports that $e \approx 1$ in an initial stage of the merger. The last consideration easily appears to be reliable. To illustrate it, we "maximize"

the eccentricity considering a high velocity encounter $v_{max} \approx 2000 km/s$ with a maximum periapsis of about $20 Kpc$, with masses of about 10^{12} , this estimation leads to an upper bound of 5. For these reasons e is considered in the range $[0, 5]$. This considerations can be summarized by equation 3.6, which denoting \mathbf{OP} as the orbital parameters establish that they follow an uniform distribution with its respective ranges.

$$\begin{aligned}\mathbf{OP} &= (q, \nu, e, \omega, i, \Omega) \\ \mathbf{OP} &\sim U[(0-q_{max}), (0-2\pi), (0-5), (0-2\pi), (0-\pi), (0-2\pi)]\end{aligned}\tag{3.6}$$

3.2.2 Observational Data Used

Now that we have a distribution for the \mathbf{OP} , it must be considered how a sampled \mathbf{OP}_i reproduces the observations. As we basically seek to construct a posterior probability and also seek to have a robust methodology to add more information that could be measured we consider a Bayesian methodology. Based in this we write:

$$P(\mathbf{OP} | \mathbf{Vobs}) = \frac{P(\mathbf{OP} \wedge \mathbf{Vobs})}{P(\mathbf{Vobs})}\tag{3.7}$$

where $\mathbf{Vobs} = (x_{sky}, y_{sky}, v_{z,sky})$ denotes the vector of observations calculated with eq. 3.4 and P denotes the probability density distribution of what it contains in parentheses. So, as $P(\mathbf{Vobs})$ will only play the role of normalization we only need to focus on the numerator. If we consider \mathcal{M} as the application from orbital parameters to its corresponding vector of observation we could consider that the orbital elements that satisfy the observations are given by eq. 3.8.

$$\begin{aligned}d &= |\mathcal{M}(\mathbf{OP}) - \mathbf{Vobs}| < \epsilon \\ d &= \sqrt{(x_{sky}(\mathbf{OP}) - x_{sky})^2 + (y_{sky}(\mathbf{OP}) - y_{sky})^2 + (v_{z,sky}(\mathbf{OP}) - v_{z,sky})^2} < \epsilon\end{aligned}\tag{3.8}$$

To give a suitable value to ϵ in the last equation the errors of the observations $(x_{sky}, y_{sky}, v_{z,sky})$ are taken into account. The percentage errors are supposed to have

a maximum, as a limiting case to be justified shortly, of 10% . That is, $\Delta r = 0.1\text{Max}[x_{sky}, y_{sky}]$, similarly for the velocity error $\Delta v = 0.1v_{z,sky}$, so epsilon is given by $\epsilon^2 = 2\Delta r^2 + \Delta v^2$. Nevertheless, these errors, Δr and Δv , could be case dependent (e.g., on the accuracy of the observational data). The use of 10% here is justified as a limiting case, such that cases with less error will still gain information in the application of the methodology, if this one is successful with a 10% error. In this respect, comparisons are made by changing Δr and Δv ; we will usually refer to Δr and Δv as spatial and velocity resolutions, respectively.

Finally, it is valuable to notice that according to the methodology proposed the resultant orbital structure (in the six dimensional space) is again an uniform distribution, but with its regions modified. There is not, however, reason to believe that this will still be the case for the one and two dimensional distributions that result from marginalizing the orbital structure.

3.2.3 Summary of Methodology

With this in mind the methodology can be summarized in the following set of steps for any particular system in which it will be applied:

1. Estimate the ranges of the priors.
2. Sample a possible set of orbital elements from the priors.
3. Estimate the value of the vector of observations for the sampled orbital elements.
4. If d (eq. 3.8) is less than the resolution error then the point is accepted, otherwise it is rejected.
5. Repeat 2-5 until a proper convergence is obtained, this last step is case dependent and it will be mentioned accordingly.

3.3 Analysis of Posteriors for Some Cases

In the rest of the chapter the method is applied and analyzed for two particular cases. The interacting systems AM 2229-735 and AM 2322-821.

3.3.1 Marginalizations

AM 2229-735

The algorithm [34], implemented using C and Python, is applied to the system in table 3.1. Figures 3-2 and 3-3 are obtained by marginalizing the posterior distribution obtained, they show the one dimensional and two dimensional marginalization correspondingly. The q_{max} obtained was of 460Kpc, nevertheless it was bound to 200Kpc in the graphs since within such a range 99 % of the data is contained and gives a better visualization. Furthermore, here the convergence (step 5 in 3.2.3) was to demand that the underpopulated regions were correctly mapped. In fact, based on the estimation that the probability of obtaining a sample in one of such regions is 10^{-5} (e.g q in $(190, 194)$ and ν in $(\pi, 1.04\pi)$) we use 10^6 total samples; in this way, with a 99 % confidence level, maximum errors are about 1 count in regions of this nature. This follows from the fact that the probability of finding n number of points in a given region follows a binomial distribution and that as samples increase in a binomial distribution, it rapidly tends to a Gaussian.

Component	Mass MG	R_{200} MG	Mass SG	R_{200} SG
Halo	70.19	278.64	3.05	108.6
x_{sky}	y_{sky}	vz_{sky}	Δr	Δv
17.95	-17.47	192	0.90	9.6

Table 3.1: Upper part: masses and virial radii of the galaxies in the AM 2229-735 system. MG stands for main galaxy, while SG for satellite galaxy. Masses are measured in units of $10^{10}M_\odot$, while lengths are measured in Kpc, and velocities in Km/s . Down part: values for the line-of-sight velocity, position and its resolutions. Estimates are used from [35].

The marginal distributions at figure 3-2 illustrate that the true anomaly, the longitude of pericenter, and the inclination are symmetric with respect to their medians. Additionally, the longitude of ascending nodes is clearly symmetric with respect to its peak, situated at $\Omega_{peak} \approx 5.45$. These symmetries can be seen perhaps more clearly when considered along a cylinder, this thanks to the angular nature of the variables and its correspondence between different branches. For example, the values $\nu < \pi$ are reflected with respect to a vertical line at π . So, we can write for the left ν its

corresponding pair, that is, $\nu \rightarrow \pi + (\pi - \nu)$. Similar analysis then shows that independent of the region (left or right) we can write the following correspondences that leave the histograms invariant:

$$\nu \rightarrow \pi + (\pi - \nu) \quad \omega \rightarrow \pi + (\pi - \omega) \quad (3.9a)$$

$$i \rightarrow \frac{\pi}{2} + \left(\frac{\pi}{2} - i\right) \quad \Omega \rightarrow \Omega_{peak} + (\Omega_{peak} - \Omega) \quad (3.9b)$$

where the corresponding angular variables at the left are measured in the branches $[0, 2\pi)$, $[0, 2\pi)$, $[0, \pi)$, and $[\Omega_{peak} - \pi, \Omega_{peak} + \pi)$ respectively. As a result, they insinuate that some combination of such transformations leave the orbital structure invariant.

Additionally, it is interesting that the q distribution has a distinct peak and a considerable region in which is more probable to find both galaxies in its near approach (e.g. 99 % of the samples have $q < 200\text{Kpc}$). These results illustrate that the initial space of parameters can be considerably reduced with a good confidence interval. The e distribution shows a slight preference for the low eccentricities, the lack of information in this sense could be in some cases complemented by the posterior detection of tidal tails since such structures point to eccentricities around 1 as we will see in more detail in chapter 4. Furthermore, ν has the interesting feature of having two peaks, one near π and other in 2π ; the other two follow from the symmetry of eq. 3.9. On a similar behaviour we have the inclination, with the important difference that both peaks are now in the near of $\pi/2$ and π (and the other ones obtained by reflection). Finally, ω and Ω distributions have both very distinctively peaks, nevertheless, the first one has a skew distribution with respect to its peak, while the second one is symmetric with respect to its peak (with a branch around Ω_{peak}). These results clearly show that the introduction of new information became quite relevant, in fact the transition from uniforms distribution to this distributions with distinct and new characteristics is very interesting.

One Dimensional Orbital Element Distributions for AM 2229-735

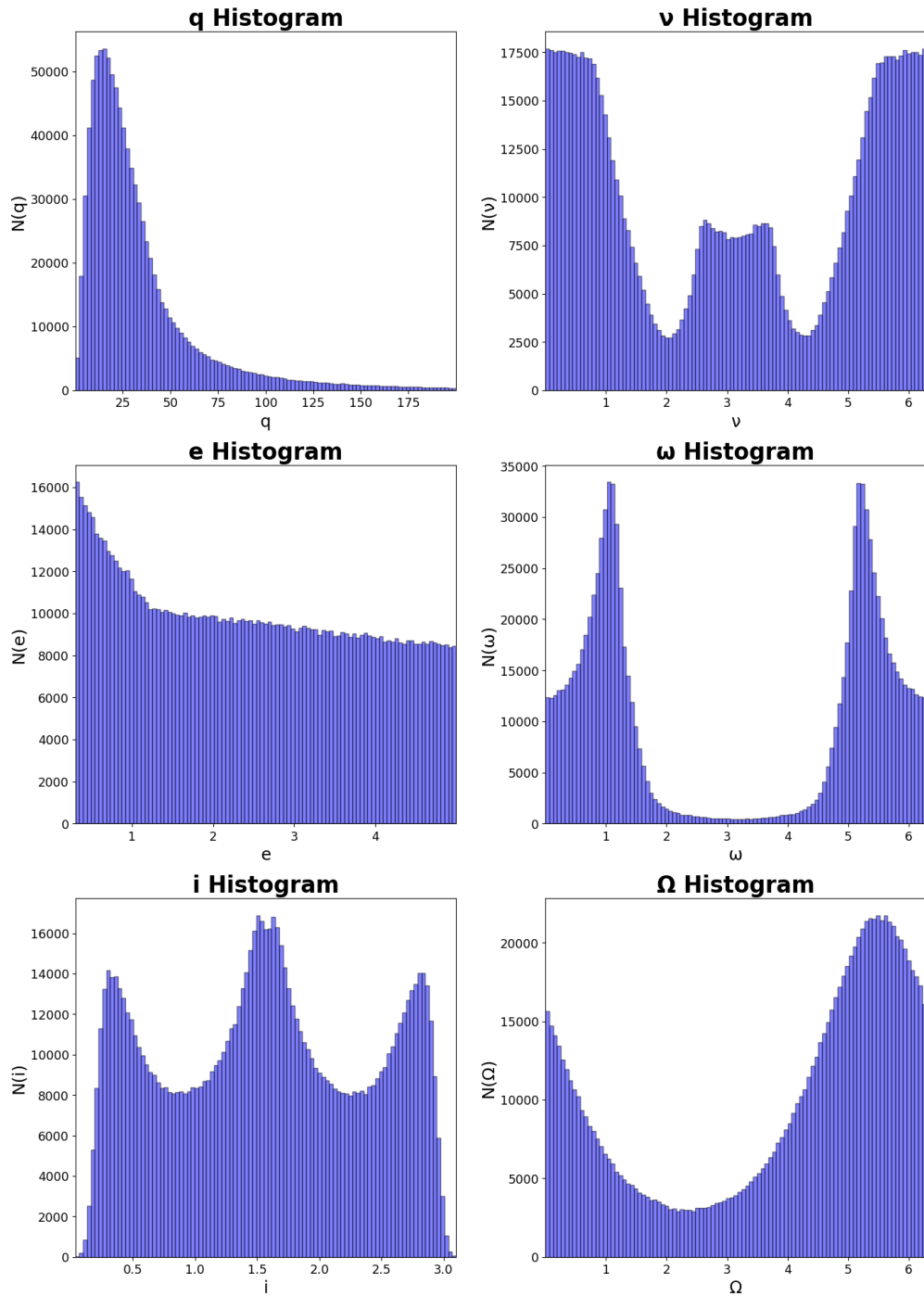


Figure 3-2: One dimensional marginal distributions for the orbital elements for AM 2229-735.

Two Dimensional Orbital Element Distributions for AM 2229-735

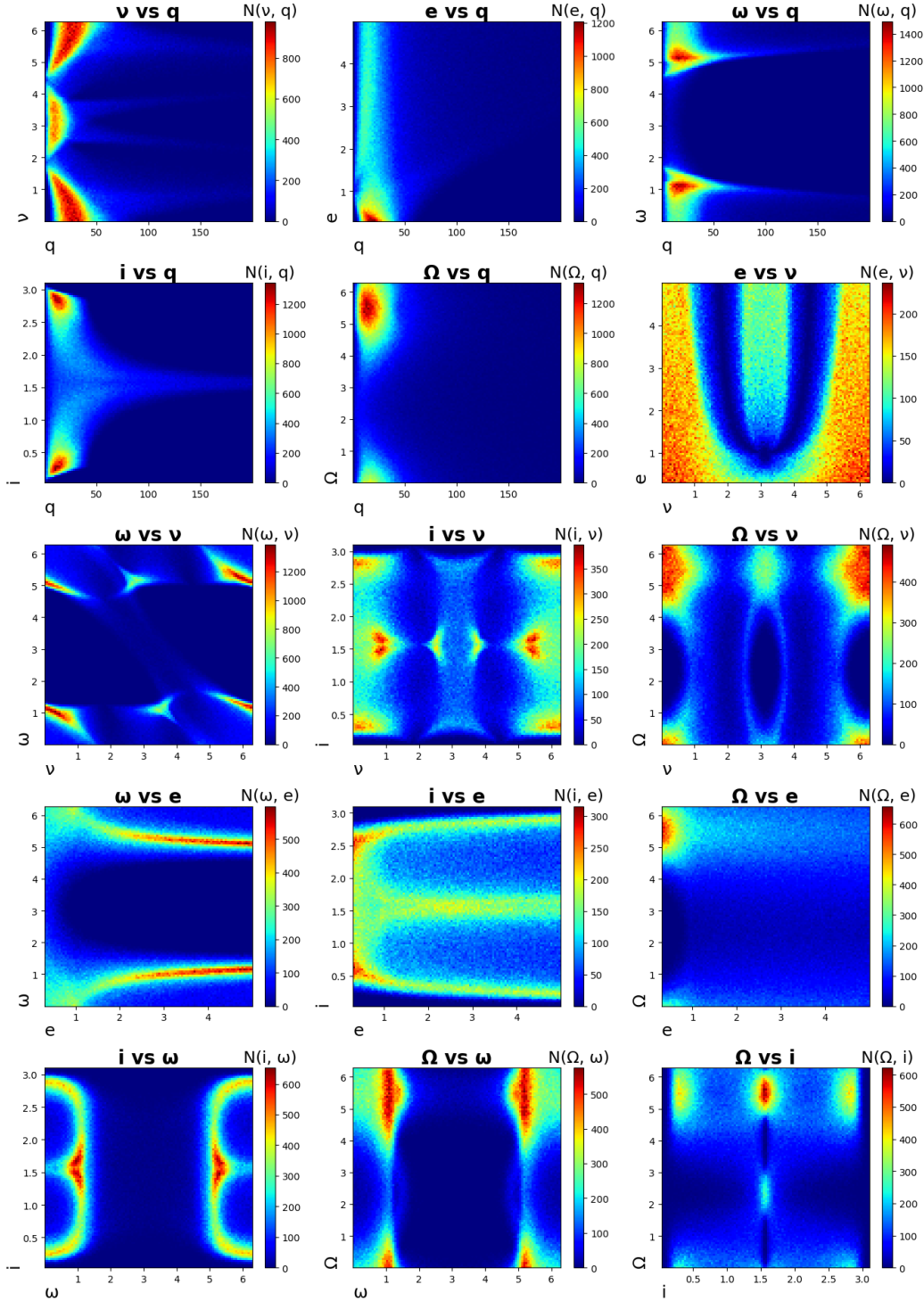


Figure 3-3: Two dimensional marginal distributions for the orbital elements. Each distribution of a pair of orbital elements was plotted with its own colorbar to better visualize changes in sample counts.

On the other hand, the two dimensional marginalizations also illustrate interesting transitions from uniform distributions to other ones with complex geometric properties. One of the most fascinating features is the existence of considerable unpopulated areas in every marginalization since the use of such information illustrates a considerable reduction of the possible values in the parameter space. Furthermore, results points out that the existence of a certain parameter in a defined region constrains the other to be in a defined region. One intriguing example of this behaviour is illustrated by the i vs q map. In this one, it is observed that when the periapsis increases, the possible values for the inclination get more constrained to a shorter range around the same central value. Another curious feature is the existence of regions that have considerably greater probability. As an example let us analyze ν vs q . Interestingly enough, it shows a parabolic-like region in the center and some type of parabolic-triangular-like region (when the down part is connected with the one above). Furthermore, a considerable space is empty, and there are curious underpopulated regions as the triangular-like shapes that extend to large q values.

AM 2322-821

So, the algorithm [34] is now applied to the system in table 3.2. Figures 3-4 and 3-5 are obtained by marginalizing the posterior distribution obtained, they show the one dimensional and two dimensional marginalization correspondingly. The q_{max} obtained is 295 Kpc and again 10^6 samples are used based in the same argument exposed for the last system.

Component	Mass MG	R_{200} MG	Mass SG	R_{200} SG
Halo	140	185.4	11.4	80.05
x_{sky}	y_{sky}	vz_{sky}	Δr	Δv
-109.9	-523.2	359.0	26.2	18.0

Table 3.2: Upper part: masses and virial radii of the galaxies in the system AM 2322-82, MG stands for main galaxy, while SG for satellite galaxy. Masses are measured in $10^{10} M_\odot$ units, lengths are measured in Kpc , and velocities in Km/s . Down part: values for the line-of-sight velocity, position and its resolutions. Estimations are used from [36]

One Dimensional Orbital Element Distributions for AM 2322-821

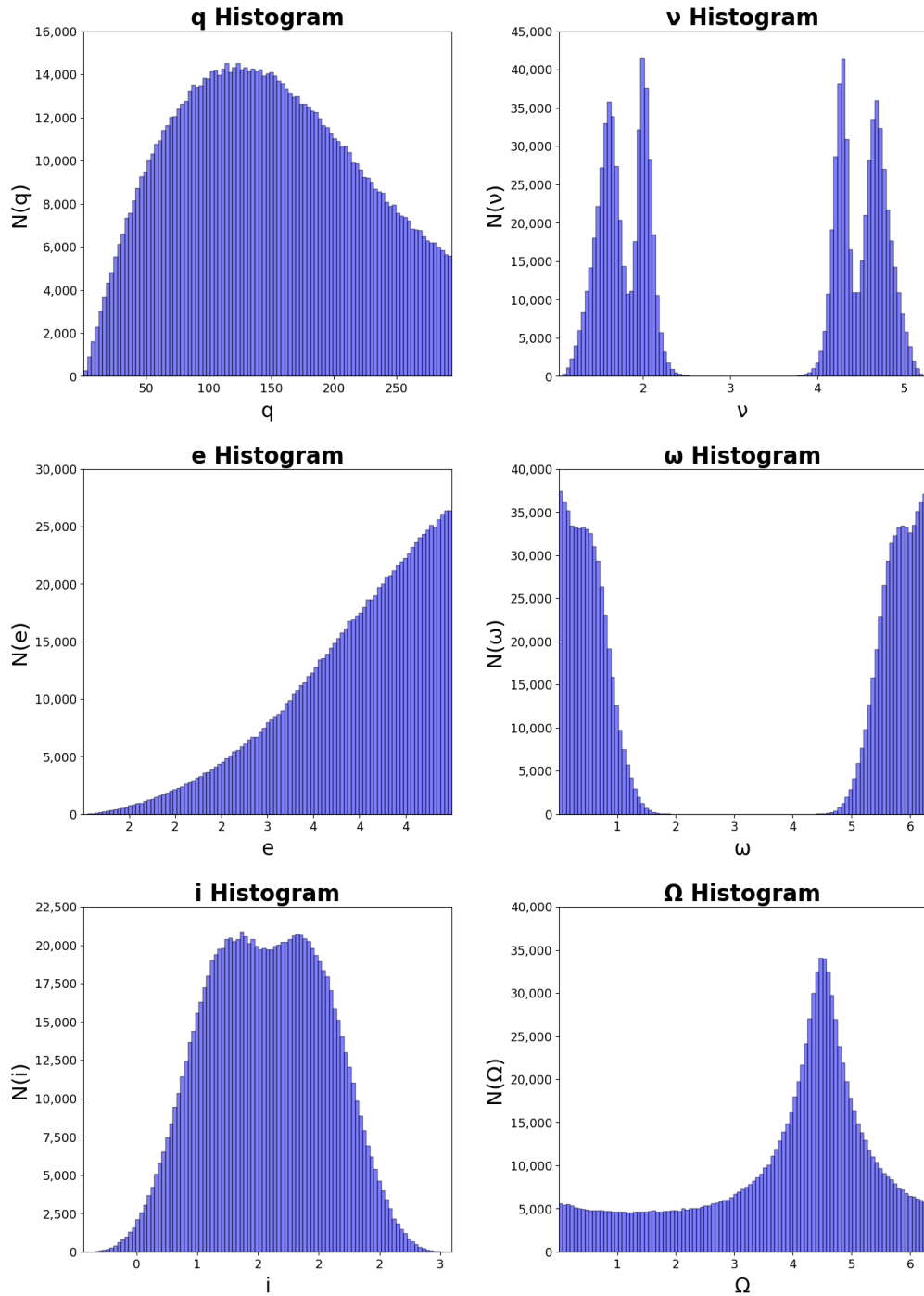


Figure 3-4: One dimensional marginal distributions for the orbital elements for AM 2322-821.

Two Dimensional Orbital Element Distributions for AM 2322-821

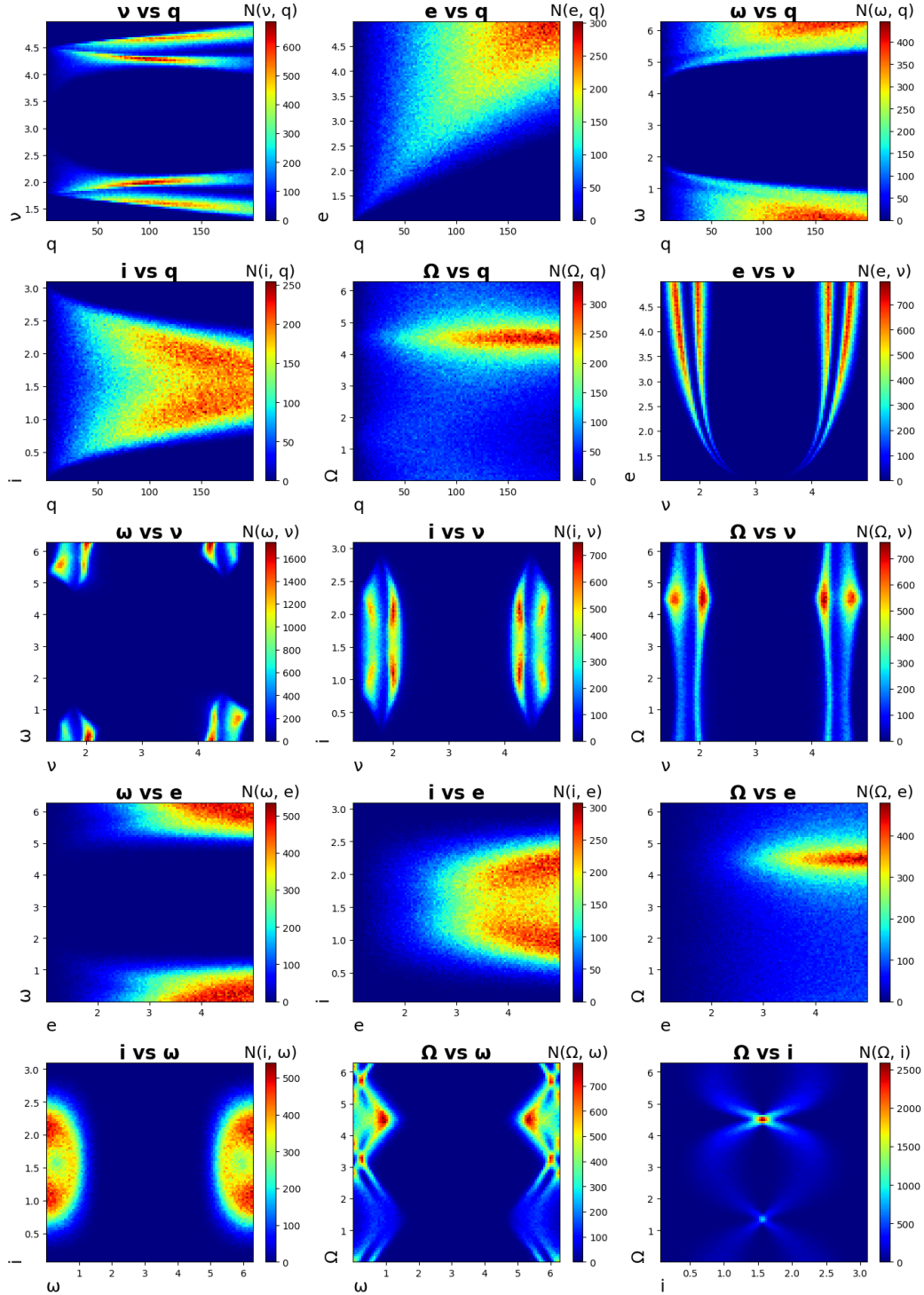


Figure 3-5: Two dimensional marginal distributions for the orbital elements for AM 2322-821. Each distribution of a pair of orbital elements was plotted with its own colorbar to better visualize changes in sample counts.

Immediately, it is observed that both systems, despite the fact that the second one is a high velocity encounter, have important similarities. For i , ω , Ω and ν we still have the symmetries between regions pointed out by equations 3.9.

Additionally, it is interesting that the q distribution has again a distinct peak around 125Kpc and it is consistent with the fact that such probability goes to 0 as q increases, nevertheless the distribution is very broad in comparison with the last example (no region is subject to be excluded). The e distribution shows in this case preference for higher eccentricities, consistent with the high speed encounter. The peaks on ν have the similar feature that when reflected respect π the other two are obtained. Nevertheless the place of both peaks are now near to 2 or 4.5 and the distribution rapidly goes to zero in the neighborhood region to the peaks. The case of i also differs considerably, in fact now only two peaks are observed. Finally and very similar, ω and Ω distributions have again very distinctively peaks, the first one (ω) have again a considerable underpopulated region but with a principal peak that appears to be symmetric, while the second one (Ω) still is symmetric with respect to its peak (with a branch around $\Omega_{peak} \approx 4.5$). Again, the results show that the introduction of new information became quite relevant in comparison with the initial uniform priors.

On the other hand, the two dimensional marginalizations also illustrate interesting transitions from uniform distributions to other ones with complex geometric properties, though with relevant differences with respect to the previous case. Again, we have the existence of unpopulated, underdense, and overdense regions. Also, it is clear again that the existence of certain parameters in a defined region constrains others to be in a defined region. A relevant and interesting behaviour of this is given by the e vs ν . In this one, it is observed that both orbital parameters are able to coexist along a defined parabola. The interesting symmetry with respect to ν will be covered in the next section, in fact we are about to prove that the left configurations ($\nu < \pi$) are equivalent to the right ones in a meaningful sense. Furthermore, in ν vs q denser and underdense regions are again evident, with a considerable part empty. A relevant example of a high sample density and small region is given in Ω vs i .

Furthermore, it is interesting the existence of apparent complementary regions with respect to the previous example. For instance, in the ν vs q case the underdense regions of AM 229-735 became the dense regions for AM 322-821. Similar behaviours are observed for ω vs q , Ω vs q , e vs ν , ω vs ν , Ω vs ν , ω vs e and i vs ω . These observations under a more detailed study could become of high relevance since the construction of the orbital structure of a set of systems will not only talk about its nature, rather about other systems too.

Finally, figures 3-3 and 3-5 raise the question of the possibility of having families of orbits that satisfy certain geometric properties. For example: are all the orbits always separated in two (inner and outer part) by a parabola in e, ν ? These types of questions are of course relevant since they permit us to better understand the structure of the six dimensional distribution and can permit us to study sets of orbits separated from one another. Although relationships of this type are found, they will be discussed in the next section in order to evaluate first how the prospect symmetries encountered can simplify the orbital structure.

3.4 Analysis of Symmetries

Proposing a more general method to construct the orbital structure based on the symmetries implicitly enunciated by eq. 3.9 is worrisome. This is principally due to the fact that our results could be drastically changed with the introduction of more appropriate priors for q , e , and ν . Nevertheless, we will see that such symmetries only lie on the fact that the condition for the observables is met (step 4 of the algorithm 3.2.3), and therefore the procedure will still be useful for different priors as will be explained in detail later.

First, it is instructive to state formally what is meant by a symmetric distribution function, $f(\mathbf{X})$. f defined in the order sets $R \equiv \{\mathbf{X} : x_{1,\min} \leq X_1 < x_{1,\text{mid}}; \dots; x_{n,\min} \leq X_n < x_{n,\text{mid}}\}$ and $R' \equiv \{\mathbf{X} : x_{1,\text{mid}} \leq X_1 < x_{1,\max}; \dots; x_{n,\text{mid}} \leq X_n < x_{n,\max}\}$ is symmetric if there exist $\mathbf{X} \in R_a$ and $\mathbf{X}' \in R_b$ such that $f(\mathbf{X}) = f(\mathbf{X}'(\mathbf{X}))$. That is, there is a correspondence between values in two parts of the

domain of the function. A standard example would be a multivariate normal distribution, which satisfies $\mathcal{N}(\mathbf{X}; \boldsymbol{\mu} = 0, \boldsymbol{\Sigma}) = \mathcal{N}(\mathbf{X}'; \boldsymbol{\mu} = 0, \boldsymbol{\Sigma})$ where $(x_{k,min}, x_{k,max}) = (-\infty, \infty)$, $(x_{1,mid}, x_{i,mid}) = (0, \infty)$ for $i \neq 1$, $X'_1 = -X_1$ and $X_{a,i} = X_{b,i}$ for $i \neq 1$.

From the above considerations, it is clear that if a symmetry is present in the six dimensional orbital element distribution, then it would be in any marginalization. Based on this insight, we propose a procedure to find symmetries. The procedure consists in identifying the symmetries in the marginalizations under analysis and then evaluating them computationally or analytically in the actual orbital structure (here, six dimensional orbital element distribution). The proposed symmetries could be used as first hypothesis. Nonetheless, symmetries present in some marginalization does not automatically translate to symmetric properties of the orbital structure as a whole since the variables could be correlated (e.g., the marginalization in x for $f(x, y) = e^{-(x+y)^2} e^{xy}$ is even but $f(x, y) \neq f(-x, y)$).

3.4.1 Reflection Symmetries and Computational Identification

Two dimensional marginalizations show that the symmetries proposed by the transformations 3.9 can be relevant, but only if some them are applied simultaneously since only in such cases the two dimensional marginalizations remain unchanged. For instance, in a symmetry for the pairs (ν, i) , we would have to transform ν and i to their corresponding symmetric regions. That is, for each $\nu \in (0, \pi)$ we would have a $\nu \in (\pi, 2\pi)$, and for each $i \in (\pi/2, \pi)$ we would have and $i \in (0, \pi/2)$. Similarly, this happens for the threesomes (ν, i, ω) , and quadruples (ν, i, ω, Ω) . We will say that the symmetries observed are therefore of a reflection nature.

However, as mentioned before the hypothetical symmetry from the marginalization does not necessarily apply to the orbital structure. Therefore, a quantification of the relevance of the proposed symmetries is also important since it can be very difficult to study the symmetry with the explicit equations of the problem (see eq. 3.2-3.4 and eq. 3.7). As any symmetry mentioned is of a reflective nature we have a direct correspondence between regions in the marginalizations.

So, to evaluate computationally the viability of a proposed symmetry we will

measure how different the orbital structure is in one region (let us say R) with respect to its symmetric pair region (let us say R'). Each region is divided in a grid of six-dimensional cubes that are denoted by C_i and C'_i . The subindeces are chosen such that the values of the orbital structure in C_i have a symmetric correspondence with the values in C'_i . Then, for a numerical estimation it is proposed to compare the mean of the absolute difference in the number of counts, N , between symmetric pairs of six-dimensional cubes with respect to the mean number of counts in six dimensional cubes (see eq. 3.10). The pairs of symmetric cubes C_i and C'_i are constructed in agreement with the transformations of the type 3.9. Finally, the closer r in eq. 3.10 is to 0 the more it appears to be a symmetric function while the closer it is to 1 it appears otherwise.

$$r = \frac{\sum_i^K |N(\mathbf{OP} \in C'_i) - N(\mathbf{OP} \in C_i)|}{\sum_i^K [N(\mathbf{OP} \in C'_i) + N(\mathbf{OP} \in C_i)]} \quad (3.10)$$

The results of using the ratio r for the different proposed symmetries are illustrated in table 3.3. It is important to mention that other reflection symmetries can also be proposed, for example only respect Ω . However, this one and all similar ones can be discarded as suitable prospects, since they are obtained from the application of two transformations in table 3.3 or are in direct disagreement with the figures 3-3 and 3-5.

Symmetry	Result
$(\nu, i, \omega, \Omega) \rightarrow (2\pi - \nu, \pi - i, 2\pi - \omega, 2\theta_{peak} - \Omega)$	1
$(\nu, i, \omega) \rightarrow (2\pi - \nu, \pi - i, 2\pi - \omega)$	1.5×10^{-3}
$(i, \Omega) \rightarrow (\pi - i, 2\theta_{peak} - \Omega)$	1
$(\nu, \Omega) \rightarrow (2\pi - \nu, 2\theta_{peak} - \Omega)$	1

Table 3.3: Proposed symmetries for the system AM 2229-735 orbital structure at the left and the computational result of evaluating each symmetry at the right.

3.4.2 Analytical Proof of the Prospect Symmetry

Evidently, from the results in the tab. 3.3 we have that the reflections for the three-some (ν, i, ω) is a promising symmetry. In the following we will summarize the proof

that this symmetry is present in the orbital structure of any system with the observations given by \mathbf{V}_{obs} . For that, let us write $(x_{sky}, y_{sky}, v_{z,sky})$ explicitly in terms of $(q, e, \nu, \omega, i, \Omega)$; denoting $\cos(x) \equiv c(x)$ and $\sin(x) \equiv s(x)$ and using eq. 3.2-3.4:

$$x_{sky} = [c(\omega)c(\Omega) - c(i)s(\omega)s(\Omega)]x_{plane} - [c(\omega)s(\Omega) + c(i)c(\Omega)s(\omega)]y_{plane} \quad (3.11a)$$

$$y_{sky} = [c(\omega)s(\Omega) + c(\Omega)c(i)s(\omega)]x_{plane} - [s(\Omega)s(\omega) - c(\Omega)c(i)c(\omega)]y_{plane} \quad (3.11b)$$

$$v_{z,sky} = \sqrt{\frac{\mu}{q(1+e)}}\{-s(i)s(\Omega)s(\nu) + c(\Omega)s(i)[e + c(\nu)]\} \quad (3.11c)$$

where:

$$(x_{plane}, y_{plane}) = \frac{q(1+e)}{1+e c(\nu)}[c(\nu), s(\nu)] \quad (3.12)$$

So, the resultant distribution with the symmetry proposed is invariant if d in eq. 3.8 is invariant. This is natural since corresponding symmetric regions will be accepted with the same probability. Similarly, d is invariant if the threesome $(x_{sky}, y_{sky}, v_{z,sky})$ is invariant. So, taking into account that $c(2\pi - x) = c(x)$, $s(2\pi - x) = -s(x)$, $c(\pi - x) = -c(x)$, and $s(\pi - x) = s(x)$ and replacing in the equations above we see that such is the case.

As a result of the analysis of the specific examples it is observed that a general symmetry has been found for any early galactic merger. The method used here could be also applied in other fields to study symmetries. For example, deducing symmetries in quantum mechanics with limited resolutions or as an important tool to create a possible theory of incomplete observations in classical mechanics.

Reduction of Parameter Space

The fact that this symmetry is satisfied for any system has important consequences. As it was mentioned at the beginning of the chapter the approximation of the orbital structure to the orbital elements distribution is a key step for the final configuration of the system. With the application of the symmetry it is clear that to evaluate the

evolution of the system we would only need to explore half of the orbital parameters that we have obtained in the posterior distribution with the procedure in sec. 3.2.3. In other words, in an early stage we are characterizing all the distribution by examining the values of the distribution in half of its domain. Furthermore, for a more efficient mapping from the resultant posterior we can use the symmetry together with an algorithm that implements important sampling. This will help to take advantage of the knowledge that there are void, underdense, and overdense regions.

In fact, for the examples examined, the parameter space can be considered reduced under good confidence intervals. In particular, we have a reduction from q in $(0, 460Kpc)$ to $(0, 200Kpc)$ in AM 2229-735 under a 99% confidence level. Other reductions for this system consist in ω from $(0, 2\pi)$ to $(0, 2) \cup (4, 2\pi)$ under a 98 % confidence. For AM 2322-821 we have for example a reduction in ω from $(0, 2\pi)$ to $(0, 1.5) \cup (4.5, 2\pi)$ with 99.9 % confidence, and in ν from $(0, \pi)$ to $(0, 2.5) \cup (3.9, \pi)$ with 99 % confidence level. This consideration as a result could lead to reduce by even a factor of 7 the volume in which we are to find the correct orbital elements with confidence values of 99 %. Further reduction will come from analyzing void regions in the two dimensional and three dimensional marginalizations of the orbital structure.

3.4.3 Symmetric Distributions Analysis and Families of Orbits

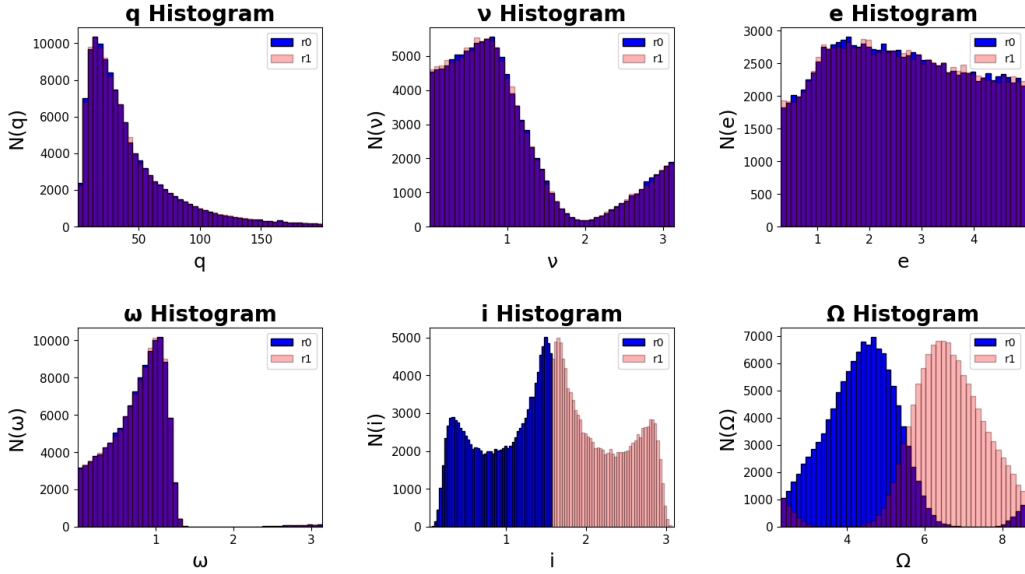
In section 3.3.1 we have raised questions about families of orbits. That is, sets of orbits that satisfy certain conditions. This question is of special relevance since it could be evaluated how each family reproduces certain observations in more advanced stages of the merger and therefore could be used to rule out more rapidly sets of orbits. To illustrate the point we will analyze the resultant families of orbits from symmetric regions of the orbital structure.

First, it must be clarified that the orbital structure can now be reinterpreted thanks to the symmetry in (ν, ω, i) . More precisely, it is enough to define the orbital structure in $(\nu, \omega, i) \in [(0-\pi), (0-2\pi), (0-\pi)]$ such that for each threesome we apply the transformations 3.9 if we desire to characterize the corresponding symmetric and equivalent (as long as $(v_{x,sky}, v_{y,sky}, z_{sky})$ are unknown) point. This makes clear that the resultant orbital structure is represented by the values in 4 different regions. To identify such regions we first denote $(\nu_{left}, i_{left}, w_{left}) \in [(0-\pi], (0-\pi], (0-\pi/2)]$ and $(\nu_{right}, i_{right}, w_{right}) \in [(\pi-2\pi), (\pi-2\pi), (\pi/2-\pi)]$. So, the regions are implied by the threesomes $(\nu_{left}, i_{left}, \omega_{left})$, $(\nu_{left}, i_{right}, \omega_{left})$, $(\nu_{left}, i_{left}, \omega_{right})$, and $(\nu_{left}, i_{right}, \omega_{right})$, which completely describe the orbital structure. To analyze the results in more detail the one dimensional distributions for the 4 regions specified are constructed for AM 2229-735, see fig. 3-6.

Figure 3-6 makes clearer the division of the orbital structure in 4 orbital families. In general terms, each family has a different characteristics, for example a different Ω distribution. These distributions could be used to make a more rapid exploration of the possible orbital elements such that it is easier to discard a larger number of possibilities. For example, later observations could agree better with some unique distributions of Ω and with left side values of ω (ω_{left}). This division of course is somewhat arbitrary, but the idea behind it is that the six dimensional distribution could be written by a kernel of distributions that capture unique geometric properties and at the same time make a good use of the symmetries.

Additionally, it must be noted that the green and the grey have a greater statistical weight than the other pairs since the counts of their bins are greater. Also, the fact that by pairs (green and grey, blue and red) are very similar only with the difference in the i distribution and the Ω distribution (up to a reflection in both), highly motivates the investigation of further symmetries in the six dimensional distribution or in some marginalization, e.g. in the variables (q, ν, e, i, ω) .

One Dimensional Orbital Element Distributions for AM 2229-735 regions 0-1



One Dimensional Orbital Element Distributions for AM 2229-735 regions 2-3

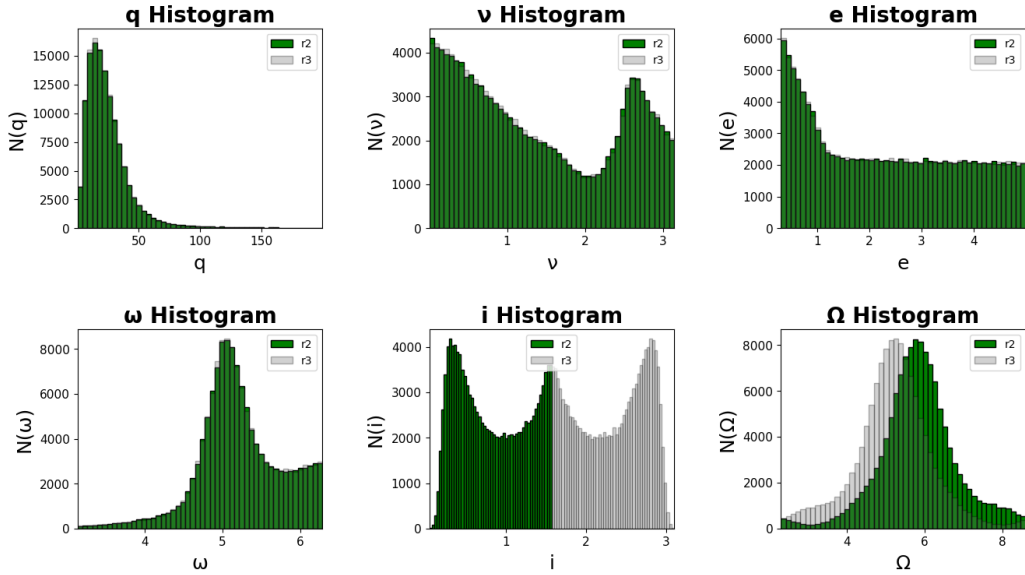


Figure 3-6: One dimensional histograms of the orbital structure using the (i, ω, ν) symmetry for the system AM 2229-735, such that, four regions characterize the orbital structure. Upper figure: blue histograms are given for regions with variables $(\nu_{left}, i_{left}, \omega_{left})$ and $(\nu_{left}, i_{right}, \omega_{left})$ for red. Bottom figure: $(\nu_{left}, i_{left}, \omega_{right})$ for green and $(\nu_{left}, i_{right}, \omega_{right})$ for grey.

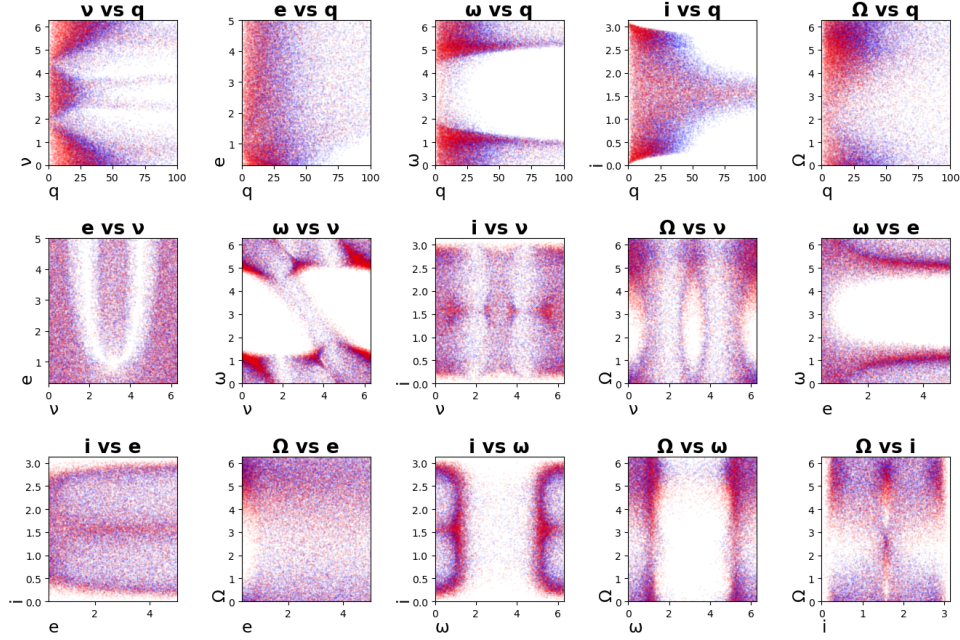
3.5 Observational errors

The analysis evaluates how meaningful the method proposed could be if errors are present and what type of biases could be expected. For systematic errors, comparisons will be made between the 2D correlation maps obtained considering biases in each observational coordinate. For the case of x_{sky} it is taken $x_{sky} + kx_{sky}$ with $k \in (0.5, 0.3, 0.1, 0.09, 0.08, \dots, 0.02, 0.01)$, while y_{sky} and vz_{sky} were considered as constant. An analogous procedure was taken for y_{sky} and vz_{sky} . The results of this simulations can be observed in a video in [34] and the top of the figures 3-7 to 3-9, which illustrate the limit example of $k = \pm 0.5$ for AM 2229-735; this correlation maps have the same resolutions (errors) as before. On the other hand, to take into account the improvement of the resolution as well as the possible systematic errors present still in such case, the above procedure was repeated, but for $\Delta r = 0.2\text{Kpc}$ and $\Delta v = 2\text{km/s}^{-1}$ in AM 2229-735. Again, the limiting results for $k = \pm 0.5$ were reproduced for the same system, figures can be observed at the bottom of figures 3-7 to 3-9.

In general, the correlation maps are still very similar in terms of their geometrical shape when systematic errors are present, but with not obvious contractions and translations. Furthermore, errors in x_{sky} and y_{sky} lead to very similar results, while the bias in vz_{sky} leads to very different results. All previous results are of particular interest because they show that similar observations still lead to similar orbital structures. That is, even with observational systematic errors useful information of the system can be obtained. The generalization of this fact to any system is nevertheless to be evaluated.

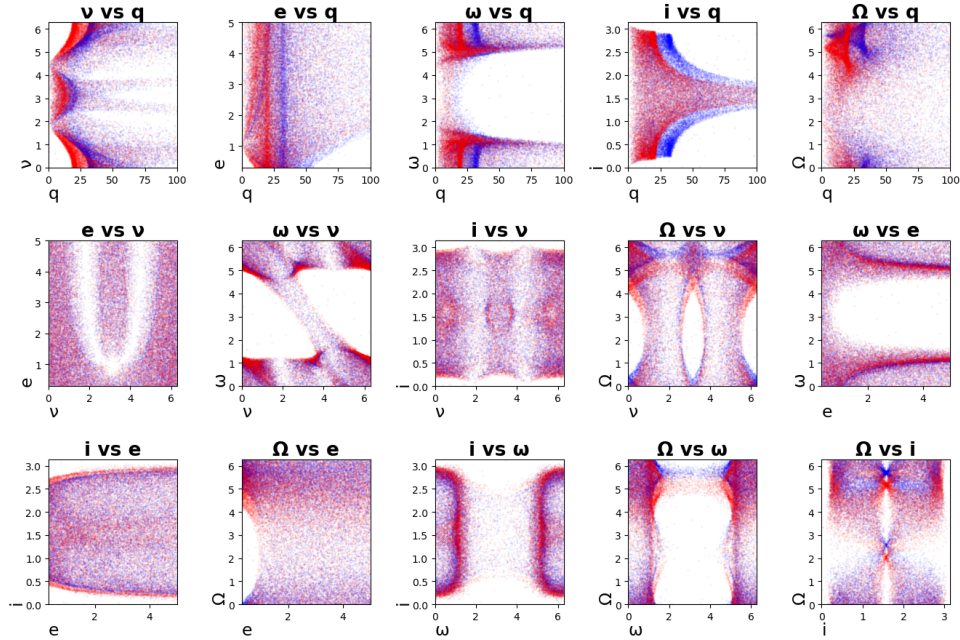
On the other hand, the resolution appears to affect considerably the width of the geometrical shapes present in the correlation maps. The improvement on the resolution clearly makes systematic errors lead to similar geometrical shapes in most cases, but in some of them there is no superposition in high probability regions. Additionally, the change in correlation maps due to the systematic error in the line-of-sight velocity is more visible when there is not a considerable resolution error; in case of considerable resolution error, correlation maps are still very similar.

Correlations Maps for Orbital Elements for x bias of +50% and -50%



(a) x_{sky} case, $\Delta r = 0.9$ Kpc, and $\Delta v = 9.6$ km/s .

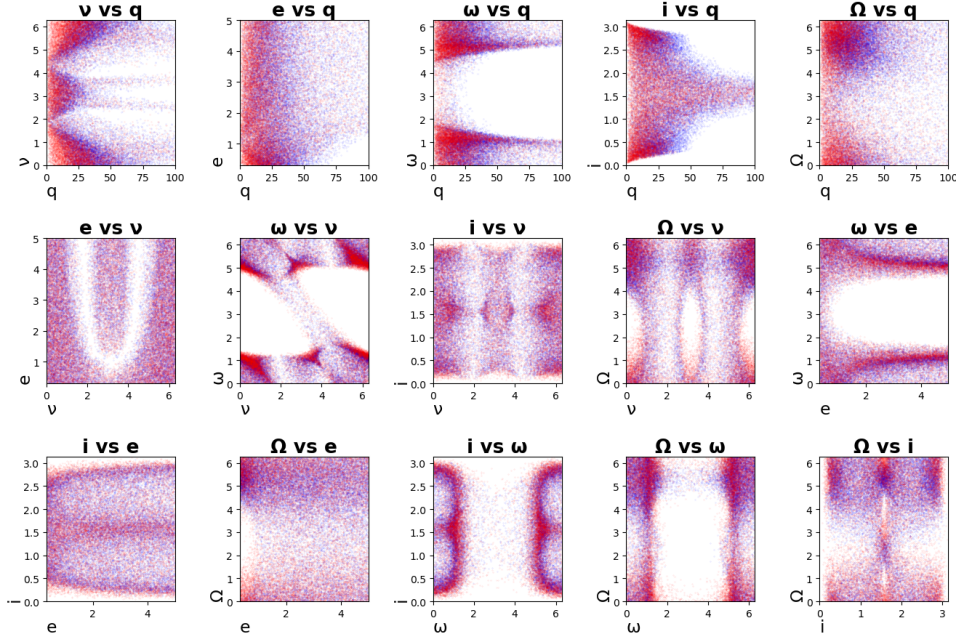
Correlations Maps for Orbital Elements for x bias of +50% and -50%



(b) x_{sky} case, $\Delta r = 0.2$ Kpc, and $\Delta v = 2$ km/s .

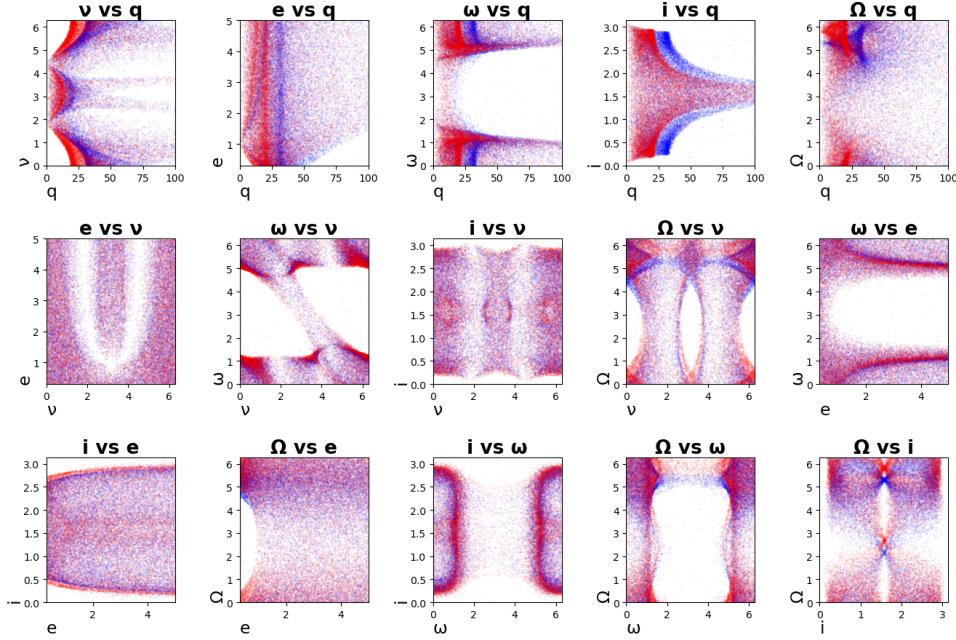
Figure 3-7: Correlations maps for system AM 2229-735 with bias errors in x_{sky} of $\pm 50\%$ for two different Δr and Δv ; for better visualization $q_{max} = 100$ Kpc.

Correlations Maps for Orbital Elements for y bias of +50% and -50%



(a) y_{sky} case, $\Delta r = 0.9$ Kpc, and $\Delta v = 9.6$ km/s .

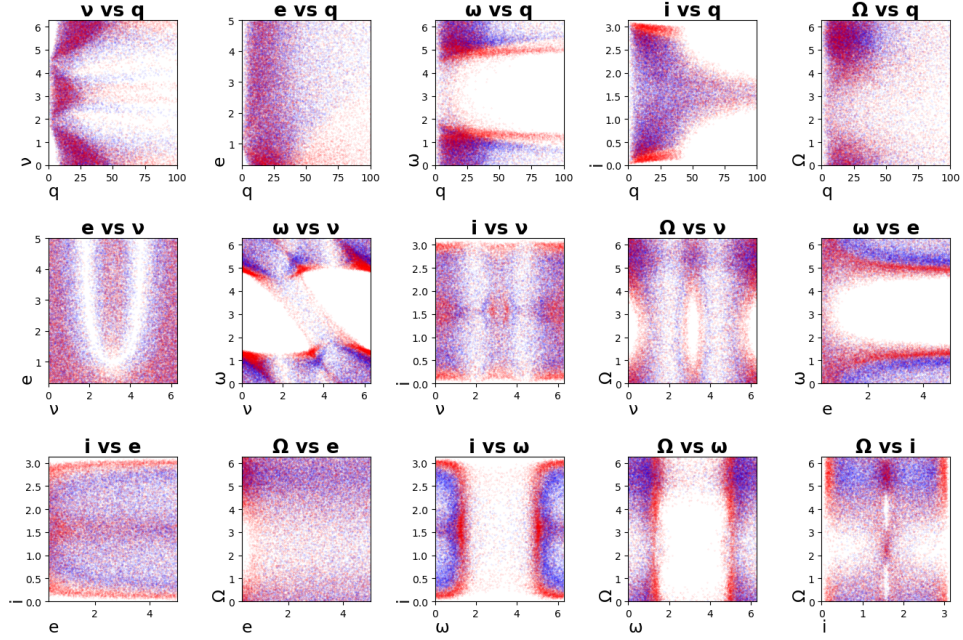
Correlations Maps for Orbital Elements for y bias of +50% and -50%



(b) y_{sky} case, $\Delta r = 0.2$ Kpc, and $\Delta v = 2$ km/s .

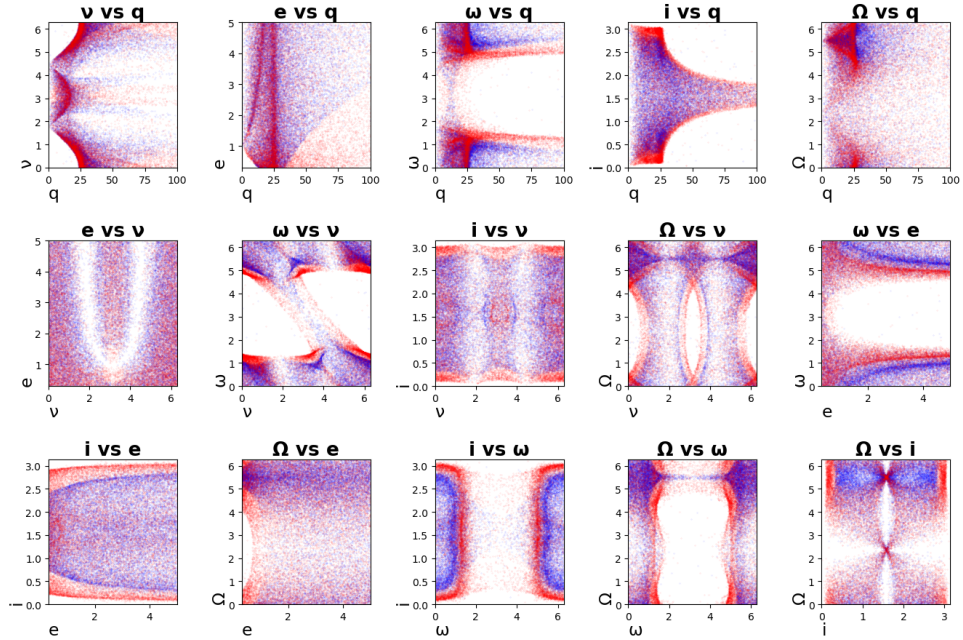
Figure 3-8: Correlations maps for system AM 2229-735 with bias errors in y_{sky} of $\pm 50\%$ for two different Δr and Δv ; for better visualization $q_{max} = 100$ Kpc.

Correlations Maps for Orbital Elements for v_z bias of +50% and -50%



(a) $v_{z,sky}$ case, $\Delta r = 0.9$ Kpc, and $\Delta v = 9.6$ km/s .

Correlations Maps for Orbital Elements for v_z bias of +50% and -50%



(b) $v_{z,sky}$ case, $\Delta r = 0.2$ Kpc, and $\Delta v = 2$ km/s .

Figure 3-9: Correlations maps for system AM 2229-735 with bias errors in $v_{z,sky}$ of $\pm 50\%$ for two different Δr and Δv ; for better visualization $q_{max} = 100$ Kpc.

3.6 Conclusions

A method for the construction of the orbital structure, which led to relevant results, was successfully implemented. Its application permits to identify prospect symmetries to be studied under an analytical approach (i. e. with the use of eq. 3.2-3.4 and eq.3.7). Also, a symmetry that reduce the size of the orbital structure space by a factor of 2 for any system was discovered, as long as $(v_{x,sky}, v_{y,sky}, z_{sky})$ are not measured. Moreover, the analysis of the one dimensional marginal distributions for particular cases shows that the size of the orbital space can be reduced by a factor of 7 under a confidence level of 99%. Further reduction should be obtained from considering the two and three dimensional marginalizations of the orbital structure.

The use of observations for the construction of a posterior together with the analysis of the two dimensional distributions of the orbital elements show that the meaningful correlations exist between the parameters. It is of special interest the void, underdense and overdense regions since such knowledge would permit a more efficient sampling (e. g. important sampling) from the possible orbits that will be later simulated under approximations that do not longer consider the galaxies as point particles.

An approach that allows to identify families of orbits that share important symmetric properties as well as a defined geometry in the orbital element distributions was successfully constructed. In addition, these resultant distributions hint towards the nature of the system, as the case of high eccentricities predicted for AM 2322-821. Moreover, the analysis of some families of orbits suggest that the orbital structure could be reduced even further with other symmetries by the marginalization in some of the orbital parameters.

The analysis of the correlation maps suggest that similar marginal distributions are obtained with the variation of resolution and systematic errors. Therefore, even from observations with errors useful information of the system can be obtained. Nevertheless, the analysis of the correlation maps for low Δv and Δr shows that considerable systematic errors can wrongly estimate the more probable regions.

Chapter 4

Galactic Pair Collisions in Systems with Tidal Features

Abstract

In this chapter we follow the work presented in the papers [2, 3, 4, 5] and partially reproduce, complement and add to their results. In short, using test particles and self-consistent methods the orbital structure of a pair-interacting system is explored. For that, the possible configurations in time of the pair-interacting systems are modeled and tidal regions are identified. Based on this, a mapping from the tidal regions back to the initial conditions is proposed. We used this proposal to investigate how well the initial orientations of each galactic disk (with respect to the angular momentum of the two body orbit and the periapsis separation estimated for an early stage) can be estimated. More specifically, we study the mapping from the tidal regions to the orientations (a.k.a. spins) for systems in which one disk is face-on (with $i = 0$) and other one has any inclination but a given angle of periapsis $w = 0$. It is shown that when all the parameters are known (with the exception of the galactic spins) observations of the tidal features constrain the orientations of the galaxies to lie in a space of 3% the size in which the orientations were initially searched, with a confidence level of 99 %. Furthermore, additional statistical analysis of the systematic errors and random errors are made, this lets us appreciate for example how such errors behave for different ground true disk orientations.

4.1 Introduction

Interacting galactic pairs can have certain observable characteristics as they evolve with time. For example, larger velocity dispersion, star formation, presence of rings,

warps, more hot gas, and others. One of the most important characteristics are tidal features, which as their name suggests are caused by tidal forces. These features are usually given by bridges, tails, and shells. The purpose of this chapter is to investigate how these features could be used to constrain the mechanical state (orbital structure in our case) of the system.

Now, although the presence of tidal regions has been proposed at least since 1952 [37], it was not immediately accepted. This had to do with the fact that tidal features were understood as broad features (and not thin and elongated) and that other alternatives were proposed to explain related observations in galaxies. Nevertheless, such features became well justified by the works as [38, 39, 40, 41, 42, 43].

More particularly, it is valuable to briefly analyze the work [1] since it brings together important considerations mentioned in previous works to easily justify the presence of tidal features. In short, this work approximates each galaxy as a punctual mass and treats the particles of the disks as non-interacting test particles; this is, nevertheless, justified by the fact that the most external particles in the disk are less influenced by self gravity.

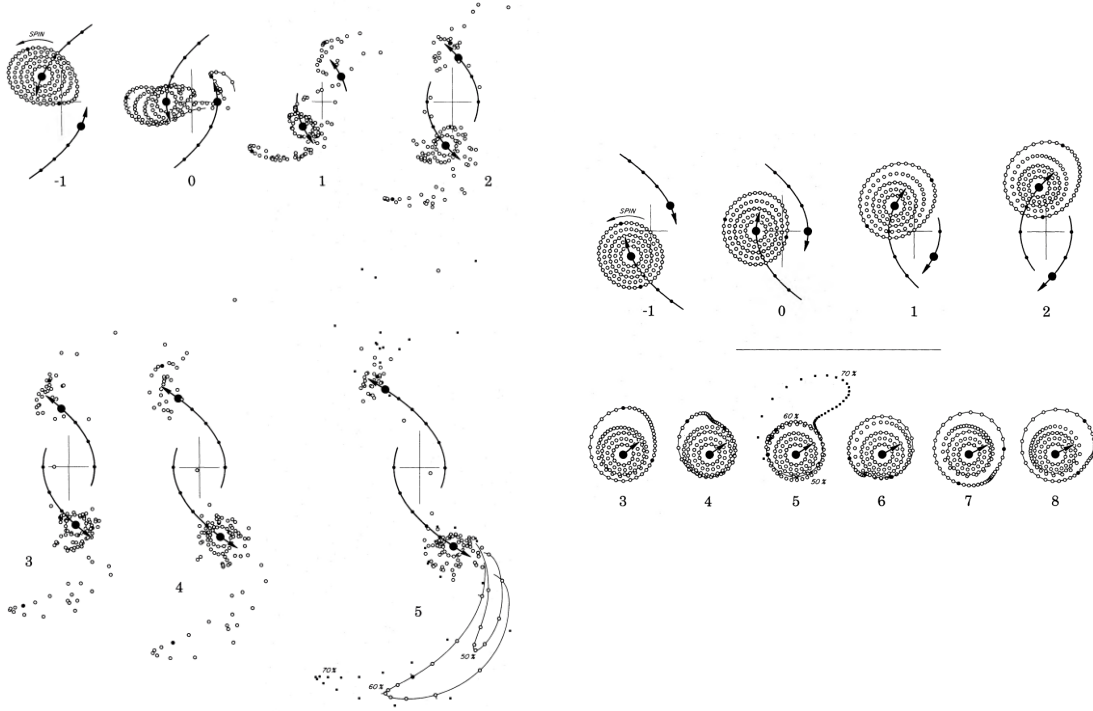
The study [1] also found that tidal features are to be formed with eccentricities around 0.5 and 1, with an upper limit of 2. Furthermore, it also analyzed direct encounters, that is, in which the angular momentum of one the galaxies coincides in direction with the angular momentum of the orbit between the galaxies (zero inclination of the disk). In this type of encounters, the study showed that tidal tails are more prone to be formed, as figure 4-1 suggests. On the other hand, in a retrograde passage (one in which the angular momentum of the galaxy coincides with the negative angular momentum direction of orbit) these features are not apparent (see fig. 4-1). It is easy to justify that such behaviours are related to a resonance or lack of resonance effect. Moreover, figures 4-1 clearly illustrate for some cases the presence of bridges (particles connecting both galaxies) and tails (particles going away from the galaxy in an elongated and thin structure). Furthermore, theoretical considerations are done to argue what size should the disk have so that tidal features are formed for a given orbital periapsis.

Finally and interestingly enough, the study also shows that for disks with several orientations and a good range of inclination tidal features are still present. In fact, it is mentioned how the curvature and width of such tidal structures observed in the sky can hint disk orientation and inclination. In fact, some considerations are applied to qualitatively match the morphology observed in some real systems.

More recent studies make use of more complex methodologies with important similarities to [1]. Particularly, the considerations done in [3, 2, 4] show how the methods have evolved towards giving meaningful numerical estimations of the parameters, at least in the sense that such resultant estimations could be used for a further N-body simulation with a larger resolution (e.g. in an ideal case the disk inclinations appear to be estimated with errors of $\approx 10^\circ$). Consequently, we will focus on these works. Particularly, we will focus on [2]. With the methodology outlined there and some modifications to it we study with what error can the orientations of each disk be determined from the observation of tidal features, when one disk is face-on with $i = 0$ and the other one has any inclination with angle of periapsis $w = 0$. Moreover, a procedure done in [2] to determine two of the Euler angles (i, w, W mentioned in last chapter) is mentioned. This is done with the aim of highlighting relevant future work that could be done by slightly modifying our statistical analysis; it must be said that we focus on [2] since we consider that it permits us to make estimations with meaningful errors.

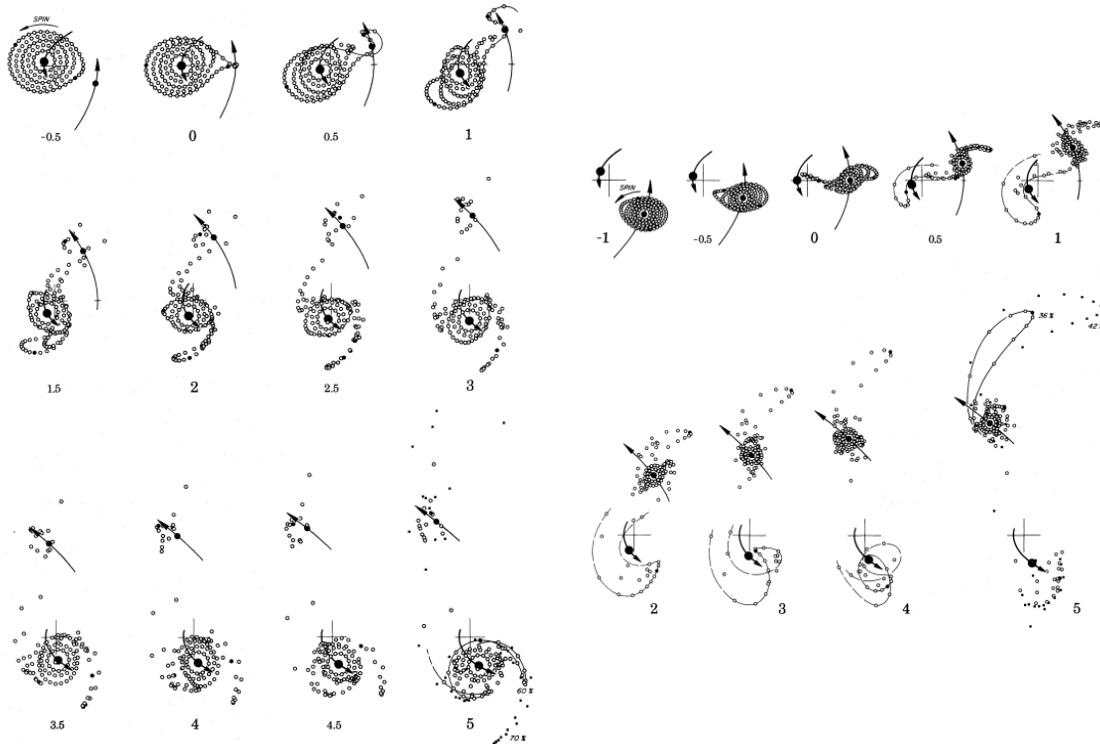
4.2 Identikit Methodology Explained

The methodology of [3] can be divided in two. First, observations are obtained or modeled. Then, several initial mechanical states are evolved and the one that best matches the observation is used to estimate the initial mechanical state. On the other hand, the methodology of [2] take modeled observations based on [3] and evaluate a mapping between each tidal region and a correspondent probability distribution of the spins (specific angular momentum) of the stars in the galaxy. Then, the multiplication of such probabilities is used to measure what are in fact the most



(a) Direct and galaxies of equal mass

(b) Retrograde and galaxies of equal mass



(c) Direct and passing quarter-mass companion

(d) Direct and four times massive companion

Figure 4-1: Modeled galactic pair collisions. Images from [1]

probable spins. Furthermore, as this product distribution depends on the parameters that characterize the initial mechanical state, then the parameters are explored and the ones that lead to the greatest peak are used as a final estimate; the work [4] simply applies the methodology of [2] to a set of GADGET SPH simulations, but automatizing relevant steps and with important considerations.

Here we adhere to the following methodology. First, observations are modeled, then the mapping from tidal regions to the spin distributions for each disk is made, and finally an statistical analysis is carried out to estimate the disk orientations with meaningful errors, which consequently evaluates the validity of the approach proposed. Consequently, we will describe all in this order.

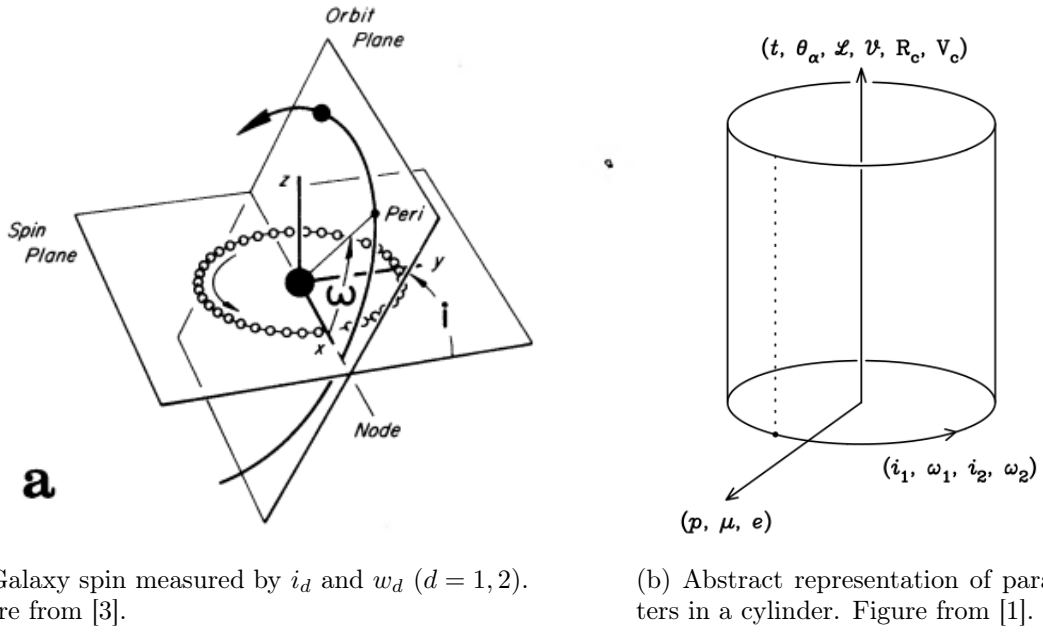
4.2.1 Ground True Data

The term ground true data is used to refer to the data that is intended to be predicted by a model or methodology proposed. In the present case, that would refer to datacubes of observations given by $F_c(X, Y, V_Z)$ where (X, Y) represents a point in the sky plane, V_Z the line-of-sight velocity measured in such point, c the component observed (e. g. neutral hydrogen), and F_c is the distribution function of stars observed in the component c at (X, Y, V) , derived from the raw observational data, the assumption that the light-to-mass ratio is constant and the considerations that all stars have the same mass.

Initial Mechanical State

First, the parameters to model the initial mechanical state of these type of systems can be divided into three groups. The first group specifies the orbit of the galaxies in an early stage, that is, the periapsis separation p , the orbital eccentricity e , and the mass ratio μ . The second group describes the spin vector of each disk, measured with respect to the angular momentum of the relative orbit and the separation between galaxies at periapsis as fig. 4-2a illustrates. These two groups together with any other parameters needed to describe the internal structures of the two galaxies specify the

initial conditions for a galactic encounter. Finally, the third group consist of the time since first periapsis t , the Euler angles (as specified in chapter 3), the scaling factors \mathcal{L} and \mathcal{V} which transform dimensionless simulations to physical quantities, and the centre of mass position on the plane of the sky \mathbf{R}_c and its radial velocity V_c ; see figure 4-2b for an abstract representation of the parameters. These last parameters are the ones needed to translate simulations to observations.



(a) Galaxy spin measured by i_d and w_d ($d = 1, 2$).
Figure from [3].

(b) Abstract representation of parameters in a cylinder. Figure from [1].

Figure 4-2: Geometrical representation of galaxy spins and abstract representation of the parameters space.

Now, in order to model observations from self-consistent galaxy disk simulations, the internal structure that is later evolved is constructed. So, each spiral galaxy is constructed with an spherical bulge (see [44]), which contains 5 % of the mass; an exponential isothermal disk, which contains (see [45]) 15 % of the mass, and the spherical dark matter halo (see [46]), which contains the remaining 80 % of the mass. The profiles are given by eq. 4.1.

$$\begin{aligned}
\rho_b(r) &= \begin{cases} \frac{a_b m_b}{2\pi} \frac{1}{r(r+a_b)}, & \text{for } r \leq b_b \\ \rho_b^* \left(\frac{b_b}{r}\right)^2 e^{-2r/b_b}, & \text{for } r > b_b \end{cases} \\
\rho_d(R, z) &= \frac{m_d}{4\pi a_d^2 z_d} e^{-R/a_d} \operatorname{sech}^2(z/z_d) \\
\rho_h(r) &= \begin{cases} \frac{m_h(a_h)}{4\pi \left(\ln 2 - \frac{1}{2}\right)} \frac{1}{(r+a_h)^2}, & \text{for } r \leq b_h \\ \rho_h^* \left(\frac{b_h}{r}\right)^\beta e^{-r/a_h}, & \text{for } r > b_h \end{cases}
\end{aligned} \tag{4.1}$$

where $r^2 = x^2 + y^2 + z^2$ is the spherical radius, a_b is the scale length of the bulge, $R = x^2 + y^2$ is the cylindrical radius, a_d is the scale length of the disk, z_d is the scale height of the disk, and a_h is the scale length of the halo. Furthermore, b_b and b_h are parameters to avoid placing a small number of particles at large radius; correspondingly ρ_b^* and ρ_h^* are chosen such that the profiles are continuous. Finally, m_t is used to indicate the total mass of the component indicated by the sub-index t , with the caveat that when m_t is used in a functional form it expresses the mass contained within the value indicated in the parenthesis. For example, $m_h(a_h)$ indicates the mass of the halo within 0 and a_h .

Based on this, the resultant cumulative distribution functions of the bulge and halo from eq. 4.2 are used with inverse sampling (i.e. solving for $m(r) = x$, where x follows a uniform distribution in $[0, m(\infty)]$) to obtain the r_i of each particle. Moreover, each position is given by $\mathbf{r}_i = r_i \hat{\mathbf{r}}_i$, where $i = 1, \dots, N_c$ and N_c denotes the total number of particles of the respective component c and $\hat{\mathbf{r}}_i$ follows an uniform distribution in a unit sphere \mathbf{S}^2 ; naturally the mass for each particle is given by $m_c(\infty)/N_c$.

$$\begin{aligned}
m_b(r) &= \int_0^r dx 4\pi x^2 \rho_b(x) \\
m_h(r) &= \int_0^r dx 4\pi x^2 \rho_h(x)
\end{aligned} \tag{4.2}$$

On the other hand, to compute the velocities for the bulge and halo particles, each given by $\mathbf{v}_i = v_i \hat{\mathbf{v}}_i$, it is used the fact that a spherical symmetric system admits

a phase-space distribution function given by (also known as Eddington formula, see pag. 288 of [24] and section 2.4.4):

$$f(\mathcal{E}) = \frac{1}{\sqrt{8\pi^2}} \frac{d}{d\mathcal{E}} \int_{\mathcal{E}}^0 d\Phi \frac{1}{\sqrt{\phi - \mathcal{E}}} \frac{d\rho}{d\Phi} \quad (4.3)$$

where $\mathcal{E} = E$ since we are supposing each halo as isolated. As a result, v_i is obtained using rejection sampling from $v^2 f(E(r_i, v))$ and \hat{v}_i is sample again from a unit sphere \mathbf{S}^2 . Furthermore, the potential Φ in eq. 4.3 is calculated using 4.4, where α is the logarithmic derivative of the density profile as $r \rightarrow 0$, the parameter $\tilde{\epsilon}$ is comparable to the softening length, and the parameter κ adjusts the shape of the transition near $r \sim \tilde{\epsilon}$.

$$\begin{aligned} \frac{d\Phi}{dr} &= G \frac{\bar{m}(r)}{r^2} \\ \bar{m}(r) &= [1 + (2/3)^{\kappa/\alpha} (\tilde{\epsilon}/r)^\kappa]^{\alpha/\kappa} m(r) \end{aligned} \quad (4.4)$$

Finally, to reconstruct the particles in the disk we use the quasi-circular and moments approximation mentioned in chapter 2, that is, the disk is sampled from the distribution 4.5.

$$f(R, \phi, z, v_R, v_\phi, v_z) \propto \rho_d(R, \phi, z) \mathcal{H}\left(\frac{v_R}{\sigma_R(R)}\right) \mathcal{H}\left(\frac{v_\phi - \bar{v}(R)}{\sigma_\phi(R)}\right) \mathcal{G}\left(\frac{v_z}{\sigma_z(R)}\right) \quad (4.5)$$

where \mathcal{H} is used instead of \mathcal{G} as eq. 4.6 show to avoid overpopulating the high velocity tails and c is fixed requiring $\int dx x^2 \mathcal{H}(x) = \int dx \mathcal{H}(x)$, which serve the function of correctly scaling the dispersions in the velocities. Furthermore, v_R, v_ϕ , and v_z are the velocities in the radial, azimuthal, and vertical directions respectively. The function $\bar{v}(R)$ is the mean rotational velocity at radius R , while σ_s is the velocity dispersion in the respective direction s .

$$\mathcal{G}(x) \propto e^{-\frac{x^2}{2}} \quad \mathcal{H} \propto e^{-\frac{1}{2}(x/c)^2 - \frac{1}{4}(x/c)^4} \quad (4.6)$$

Now, the vertical dispersion is deduced from the isothermal disk using the Poisson and Boltzmann equation (see eq. 4.7a), where $\Sigma(R)$ is the surface density of the disk. The radial dispersion is interpolated by 4.7b from the fact that in the solar neighborhood its value is of $\approx 2\sigma_z$ and that as it approach the $R \rightarrow 0$ it must have the same value than the vertical dispersion (note that R_d in eq. is comparable to a_d). The azimuthal dispersion (see eq. 4.7c) is also deduced from the Boltzmann equation, but certain suitable symmetries are demanded (see. pag. 202 of [24]):

$$\sigma_z(R) = \sqrt{\pi G z_d \Sigma(R)} \quad (4.7a)$$

$$\sigma_R(R) = \mu(R)\sigma_z(R) = \left(1 + \frac{R}{R_d + R}\right)\sigma_z(R) \quad (4.7b)$$

$$\sigma_\phi(R) = \frac{\kappa}{4\Omega}\sigma_z(R) \quad (4.7c)$$

where $\Omega(R) = v_c(R)/R$ is the circular orbital frequency and $\kappa = \sqrt{4\Omega^2 + Rd\Omega^2/dR}$ is the epicyclic frequency; see 4.8a and 4.8b for the circular velocity $v_c(R)$ and the potential of the disk, respectively, where $J_1(x)$ is the cylindrical Bessel function of order 1, and setting $\epsilon_d = \sqrt{\epsilon^2 + z_d}$ allows us to approximate the finite thickness of the disk. Finally, the mean rotation velocity $\bar{v}(R)$ is determined using the Jeans equation (see pag. 198 of [24]) as indicated by eq. 4.8c:

$$v_c^2(R) = G \frac{\bar{m}_b(R) + \bar{m}_h(R)}{R} + R \frac{d\Phi_d}{dR} \quad (4.8a)$$

$$\frac{d\Phi_d}{dR} = -\frac{G m_d}{a_d^3} \int_0^\infty dk \frac{k e^{-k\epsilon_d} J_1(kR)}{(a_d^{-2} + k^2)^{3/2}} \quad (4.8b)$$

$$\bar{v}^2(R) = v_c(R) + \sigma_R^2(R) \left(1 - \frac{2R}{a_d}\right) - \sigma_\phi^2(R) + \sigma_z^2(R) R \frac{d\mu^2}{dR} \quad (4.8c)$$

The values used are indicated in 4.9. With such values the simulations used natural units with $G = 1$. For more details see [3].

$$\begin{aligned}
m_b &= 0.0625 & m_d &= 0.1875 & m_h(a_h) &= 0.16 & \epsilon &= 0.0075 & R_\sigma &= 0.075 \\
a_b &= 0.02 & a_d &= 1/12 & a_h &= 0.25 & \tilde{\epsilon} &= 0.0115 & \kappa &= 1.975 \\
b_b &= 4.0 & x_d &= 0.0075 & b_h &= 0.98015 & \tilde{\epsilon}_s &= 0.0115 & \kappa_s &= 2.025
\end{aligned} \tag{4.9}$$

Force Calculation

The force calculation is done through a treecode algorithm. This valuable proposal was initially formulated with a robust approach to calculate the error in the force estimation in [47]. Nowadays, modifications which still preserve the principal ideas of the initial proposal are used in high performance codes for simulating N-body systems as in GADGET 4 [48]. Here, we will use the treecode algorithm provided in [49], the same used in [3]. So, a brief description of the code is presented.

First, an oct-tree is constructed for the particles in the system. For that, initially all the system is initially enclosed in a cube, known as the root node. If the enclosed system consists of one particle, then the process ends. Otherwise, the initial cube is divided into 8 equal cubes, these cubes are defined as the childs of the root node. Again, it is checked if any of the cubes (child nodes) has only one particle, and for the cubes for which that is the case the further division is stopped. Otherwise, the process is repeated for the subsequent child nodes until each particle is contained in a single cube. Image 4-3a illustrate the situation in two dimensions.

Based on such division, the codes associates to each node a total mass located at its center of mass (pseudoparticle) so that for particles sufficiently far away the interaction can be rapidly calculated. More precisely, the code calculates the force at the particle p through the following iterative process. First, it stands in the root node of size l and calculates the distance between the pseudoparticle of the actual node and the particle, denoted as D . So, if $\frac{l}{D} < \theta$, then the interaction between such particle and the cell is considered through a multipole expansion (see pag. 127 of [25]). Otherwise, we pass to repeat the process with each of the child nodes of the

parent node for which we have just obtained $\frac{l}{D} > \theta$; for the present case θ was chosen as 1. Figure 4-3b illustrates the nature of the interaction for a specific particle in a two dimensional case.

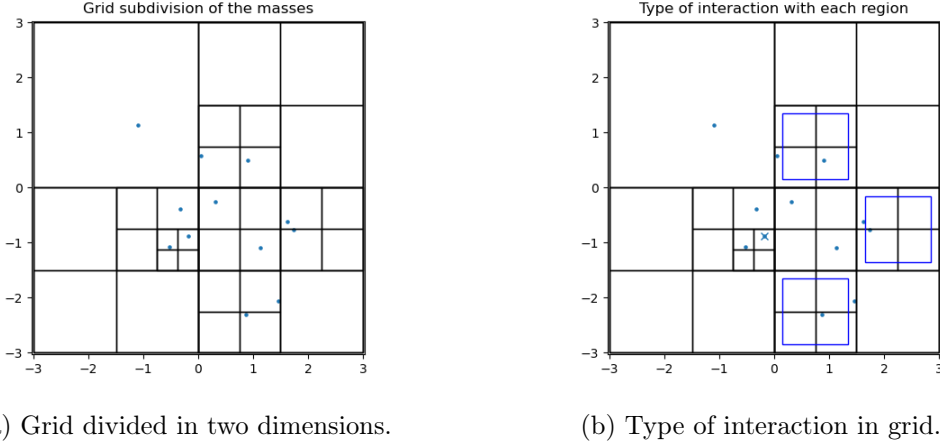


Figure 4-3: (a) indicates the grid that divides the particles. (b) Indicates the divided grid with the type of interaction for the particle crossed by an x, the blue cubes are treated by this one as pseudo-particles; the other ones are considered as single particles. Blue cubes are slightly rescaled for clarity

This algorithm is useful since it permits to model the collisional nature of the system by calculating the force within $O(N \log(N))$ steps in comparison with a direct force calculation of N^2 steps. Furthermore, the parameter θ clearly gives a trade-off between the precision and computational cost, which naturally depends on the case.

Evolution

The evolution is done by the synchronized leap-frog method, using for this the initial mechanical state constructed and the force calculation as was mentioned before. This method has the advantage of being time reversible and being symplectic, the last meaning that it conserves the (slightly modified) energy of the system. The formula to advance the positions \mathbf{r} and velocities \mathbf{v} of a particle from step n to step $n + 1$ are:

$$\begin{aligned}
\mathbf{v}_{n+1/2} &= \mathbf{v}_n + h/2 \mathbf{a}_n \\
\mathbf{r}_{n+1} &= \mathbf{r}_n + h/2 \mathbf{v}_{n+1/2} \\
\mathbf{v}_{n+1} &= \mathbf{v}_{n+1/2} + h/2 \mathbf{a}_{n+1}
\end{aligned} \tag{4.10}$$

where h is the time step, and \mathbf{a}_0 , \mathbf{v}_0 , and \mathbf{r}_0 the initial acceleration, velocity, and position of a particle being evolved, respectively.

Initial Mechanical State Simplified with Test Particles

With the procedure for the construction of the mechanical state of a galaxy specified before, a simulation for a galaxy in isolation was evaluated. This one with $N_b = 16384$ bulge particles, $N_d = 49152$ disk particles, and $N_h = 65536$ halo particles. In [2] it was found that during an interval of 0.25 time units the ratio T/U decay from 0.4980 to 0.4945 and then varied with an amplitude of ~ 0.003 . This indicated that the system took some time to enter in equilibrium, state in which its statistical fluctuations of the order $1/\sqrt{N} = 0.0028$

This consistency together with the fact that tidal features in a disk are mainly formed by its gravitational interaction with both halos (as indicated in the introduction and justified by three body approximation discussed in chapter 2) let us simplify the model treating the disk particles as massless (i. e. test particles). Furthermore, the fact that the orbital decay is largely driven by the interaction between halos [50] let us simplify the model as follows.

Each galaxy will be considered to have an spherical profile given by 4.11, where $m_d(r)$ represents the marginalization of a thin disk in the r coordinate given by 4.12. Therefore, following the inverse sampling procedure indicated for 4.2 and Eddington formula 4.3 (but for $m(r)$ in 4.11) an spherical distribution that represents the particles with mass in each galaxy can be constructed. This realization is done with $N_{sphr} = 8.0 \times 10^4$.

Nevertheless, inside each spherical representation of a galaxy multiple disks of test

particles are embedded. These multiple disks are represented by a spherical distribution $m_d(r)r^2$, where the direction of the angular momentum of the i-th sampled particle, $\hat{\mathbf{s}}_i$, follows an uniform distribution in the unit sphere \mathbf{S}^2 . Furthermore, each particle is consider in a circular orbit with a velocity given by $\sqrt{G\bar{m}(r)/r}$; the total number of this particles would be $N_{test} = 2.56 \times 10^5$.

Two observations should still be added. First, the distribution $m_d(r)r^2$ is chosen to represent the test disks instead of $m_d(r)$ to improve the mapping of test particles at large distances; in the end observations at considerable distances could be obtained from long exposures. Second, based on the construction before, a particle with spin $\hat{\mathbf{s}}_i$ belongs to a disk with $\hat{\mathbf{s}}_d$ if it satisfies 4.13. This last condition can be constructed by the following argument. Accepting $1 - \hat{\mathbf{s}}_i \cdot \hat{\mathbf{s}}_d \leq \sigma$ where sigma is small is evident from the fact that to estimate the value of $\hat{\mathbf{s}}_d$ from samples $\hat{\mathbf{s}}_i$'s, we should take the samples in a small solid angle $\delta\Omega$ around $\hat{\mathbf{s}}_d$, since this solid angle is unequivocally related to the product $\hat{\mathbf{s}}_i \cdot \hat{\mathbf{s}}_d$. This demands as a result that a certain number of particles are given for each disk, i. e. $N_{test}\delta\Omega \approx \delta N_{disk}$. Finally, if we bias the disk distribution by r^2 , then with the aim to still satisfy the last enunciated condition at every r , $\delta\Omega$ would take the value $\delta\Omega/r^2$; note that r_{min} is chosen to prevent the condition to diverge and it has little effect if in fact it is chosen small.

$$m(r) = m_b(r) + m_d(r) + m_h(r) \quad (4.11)$$

$$m(r) = m_d(1 - e^{(-r_d/a_d)})(1 + r/a_d) \quad (4.12)$$

$$1 - \hat{\mathbf{s}}_i \cdot \hat{\mathbf{s}}_d \leq \sigma/\max(r, r_{min})^2 \quad (4.13)$$

This simplification of the original model is used in [3] to try to match the observations constructed from the model in section 4.2.1. In [2] the simplified model is used to simulate the observations, and from them try to reconstruct part of the initial mechanical state. Now, we will mainly focus in the last approach because in comparison with [3], it offers clarity in the metric used to evaluate how good are the

estimated quantities; furthermore, other considerations of [4] can be used to quantify the possible introduction of some random errors.

Finally, as a last comment is in order to do a technical correction. In the previous paragraphs it was enunciated that either orbital decay as well as tidal features are the result of the gravitational interaction in the disks due to the halos, more correctly it will be to say the result of the gravitational interaction in the disks due the mass contained within a given radius of each companion (each respect to its center of mass).

Deriving Disk Spins from Tidal Features

Clearly, the probability distribution of all the possible disks for a galaxy d ($d = 1, 2$) in a time t can be contained in an extended distribution given by eq. 4.14 (with $\xi_i = \max(r_{min}, r_i(t_0))^{-2}$ to account for the bias introduced in the disk). This in the sense that when eq. 4.14 is marginalized over the correct range around the initial spins $\hat{\mathbf{s}}_i = \hat{\mathbf{s}}_i(t = t_0)$ and all the weight factors ξ , it must lead to the correct phase-space distribution for a given disk.

$$g_d(\mathbf{r}, \mathbf{v}, \mathbf{s}; t) = \sum_{i=1}^{N_{test}} \delta^3(\mathbf{r} - \mathbf{r}_i(t)) \delta^3(\mathbf{v} - \mathbf{v}_i(t)) \delta^2(\mathbf{s} - \mathbf{s}_i) \delta(\xi - \xi_i) \quad (4.14)$$

This distribution can be used of course in an inverse sense, that is, integrating over the phase space will lead to the initial spin distribution of the particles, that in turn could be used to estimate the spin of each galaxy. Nevertheless, as mentioned before we are interested in studying if from the available observations of the tidal features we can reconstruct the for disk spins. So, to reconstruct the spin distribution from such tidal regions we suppose that n_{reg} tidal regions are given and denoted by $\tilde{\mathbf{q}}_i$. As a result, the spin distribution is constructed as eq. 4.15 for a given tidal region.

$$\Omega_d(\mathbf{s}; \tilde{\mathbf{q}}_i, t) = \int d\xi \int_{(\mathbf{x}(t), \mathbf{v}(t)) \in \tilde{\mathbf{q}}_i} d^3\mathbf{r} d^3\mathbf{v} \xi g_d(\mathbf{r}, \mathbf{v}, \mathbf{s}; t) = \sum_{(\mathbf{x}(t), \mathbf{v}(t)) \in \tilde{\mathbf{q}}_i} \delta^2(\mathbf{s} - \mathbf{s}_k) \xi_k \quad (4.15)$$

However, to construct this from observations we simply must consider the mapping from (X, Y, V_z) to (x, y, v_z) through the Euler angles and scale parameters that are considered as known in this case. With this in mind we consider that any threesome (x, y, v_z) obtained from this mapping that belongs to $\tilde{\mathbf{q}}_i$ is part of the tidal region. This, because in the absence of (Z, V_x, V_y) we consider that they can in fact take any value.

Now, the assumption that the resultant distribution function must be smooth can be used by interpolating its points. This is expressed in eq. 4.16-4.17 and together with the assumption that such tidal regions are independent, the final distribution taking into account all the regions can be written as eq. 4.18. A few comments of this procedure are in order. In eq. 4.16 $K(\tilde{\mathbf{q}})$ is a constant of normalization that can be chosen to normalize the peak to one, or that can be a simple normalization constant to ensure that the integral over all space is one. Furthermore, the smoothing function w not mentioned in the paper can be deduced by analyzing the source code and it is the cubic spline kernel (see eq. 4.17; where σ_3 is constant depending on the resolution and x is the inclination or argument of periapsis; see [51] for more details).

$$\overline{\Omega_d}(\mathbf{s}; \tilde{\mathbf{q}}_i, t) = K(\tilde{\mathbf{q}}) \sum_{(\mathbf{x}(t), \mathbf{v}(t)) \in \tilde{\mathbf{q}}_i} \xi_k w(\mathbf{s} - \mathbf{s}_k) \quad (4.16)$$

$$w(x) = \begin{cases} \sigma_3 \left[1 - \frac{3}{2}x^2(1 - \frac{x}{2}) \right], & \text{for } 0 \leq x \leq 1 \\ \frac{\sigma_3}{4}(2 - x)^3, & \text{for } 1 < x \leq 2 \\ 0, & \text{otherwise} \end{cases} \quad (4.17)$$

$$\Omega_d^*(\mathbf{s}; \tilde{\mathbf{q}}, t) = \Pi_{j=1}^{n_{reg}} \overline{\Omega_d}(\mathbf{s}; \tilde{\mathbf{q}}_j, t) \quad (4.18)$$

With this in mind, we intend to construct spin disk distributions for particular systems in which one disk is face-on with $i = 0$ and other has any inclination with angle of periapsis given by $w = 0$. From such distribution (eq. 4.18) we can naturally estimate the spin of the galaxy as the mean or more probable spin.

Deriving Viewing Angles

It is valuable to add that a defined procedure to find two of the euler angles is used in [2]. This one is nevertheless only succinctly described with the help of a procedure called center locking. The basic idea is to fix the centers of the simulated galaxies to coincide with the observations. This procedure is supposed to be done by recognizing that for given arbitrary configuration there is a unique way to choose one Euler angle, the center of mass offset, and the length scale, such that the centers coincide. As a result two Euler angles are functions of the parameters mentioned before. Nevertheless, before considering the specific results (spin distributions) of each system it is required to make some general consideration and remarks.

4.3 Identikit Applied

4.3.1 Disk Spins

With the interest of studying how the methodology proposed above behaved to estimate disk spins, it was studied how the algorithm works for cases in which one disk was face-on with $i = 0^\circ$ (disk 2) and the other had inclination given by $i = 0^\circ, 10^\circ, 20^\circ, 30^\circ, \dots, 180^\circ$ with $w = 0^\circ$ (disk 1).

General Considerations

Each galaxy was realized in agreement with section 4.2.1. All the systems were put in an orbit with $p = 0.5$ and $e = 1$; figure 4-4 illustrates the graphical user interface (GUI) of the software in which the tidal regions are chosen. In such image the system in which both galaxies are face-on with $i = 0$ is shown. The rest of the systems with its selected tidal regions and their resultant spin distributions are illustrated in figures 4-5 to 4-7; all of them are explicitly shown with the intention facilitating replicability.

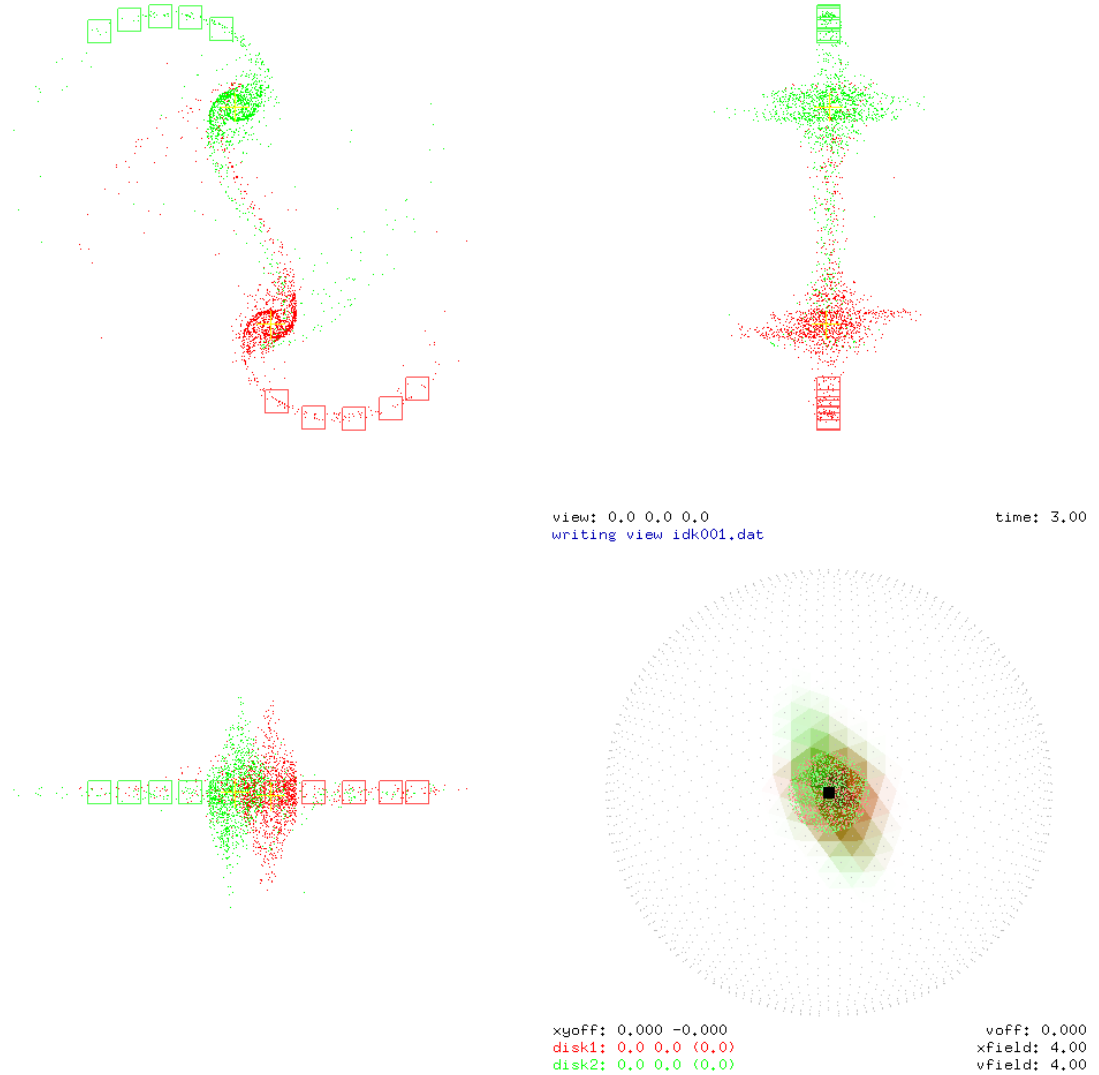


Figure 4-4: GUI of the program Identikit [2]: (X, Y) projections in the left upper part, (Y, V_z) projection in the upper right, (V_z, X) projection in the down left and the resultant spin distribution (see eq. 4.18) for each disk of the system in consideration in the down right. The current system illustrated has $(w_1, i_1) = (0, 0)$ and $(w_2, i_2) = (0, 0)$. The red galaxy will be refereed as galaxy 1 and the green one as galaxy 2. Moreover, the boxes in red and green in all of the projections represent the selected tidal regions for each galaxy.

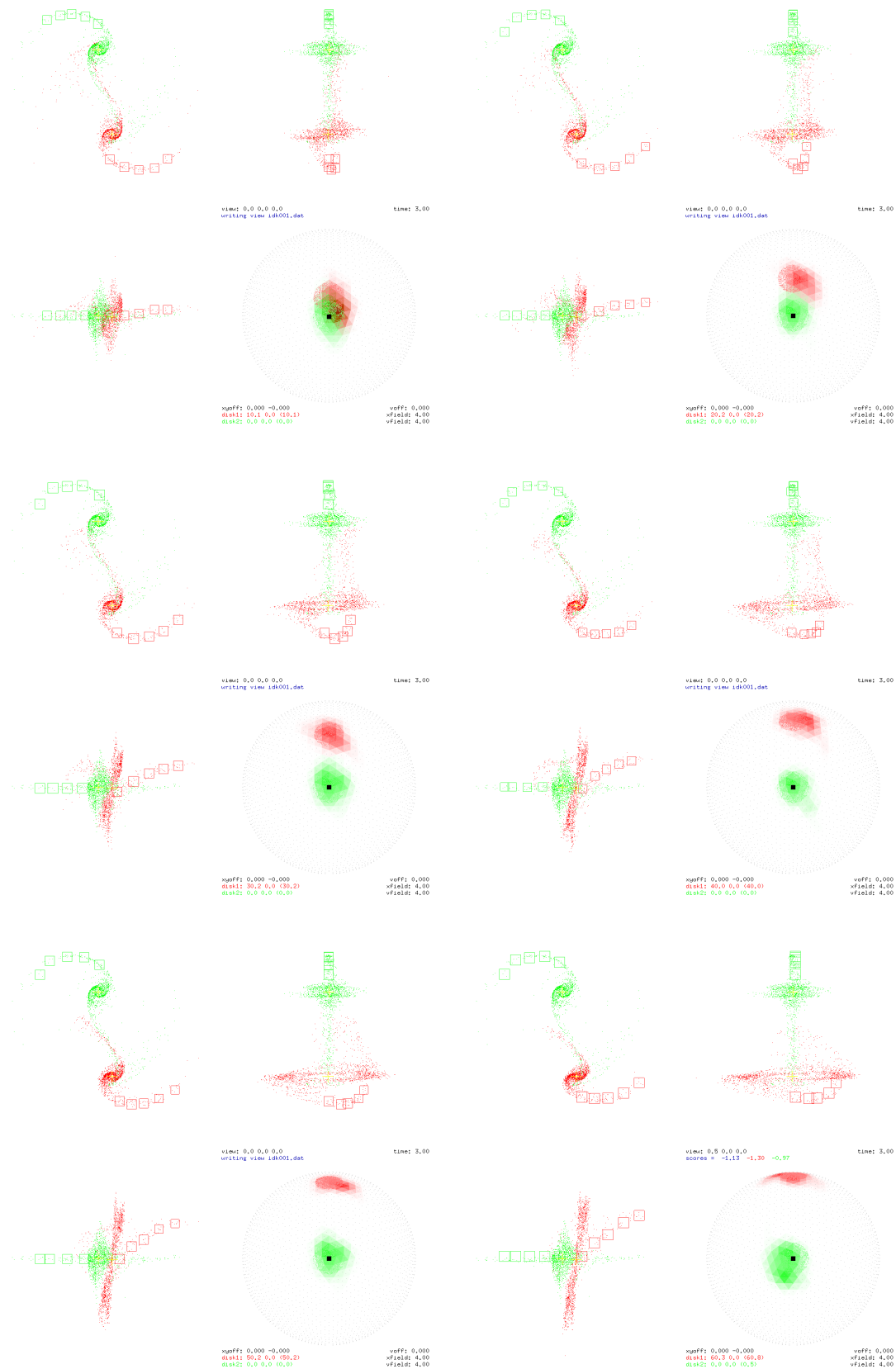


Figure 4-5: In standard reading order: systems with i_2 in $(10^\circ, 60^\circ)$.

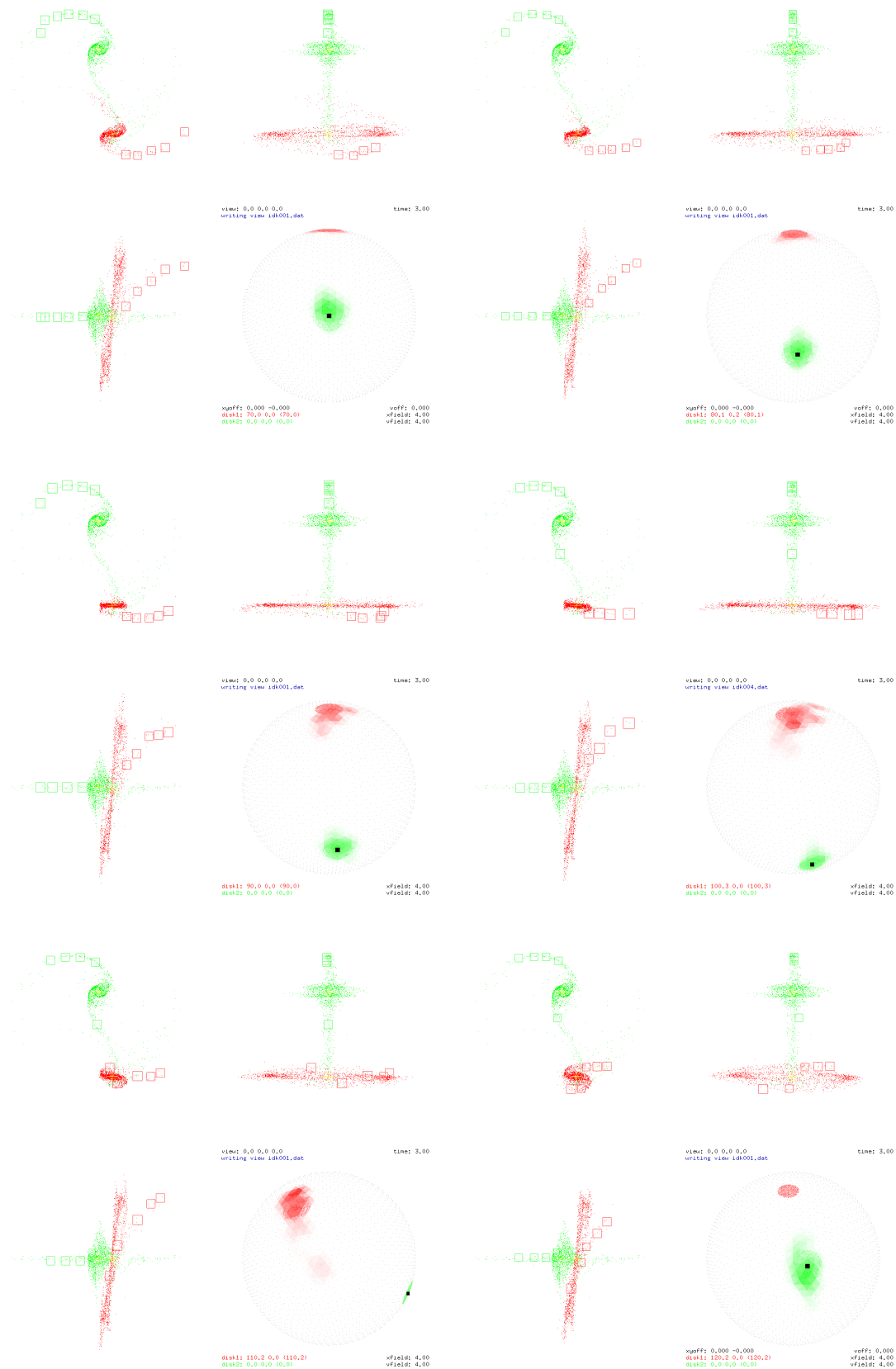


Figure 4-6: In standard reading order: systems with i_2 in $(70^\circ, 120^\circ)$.

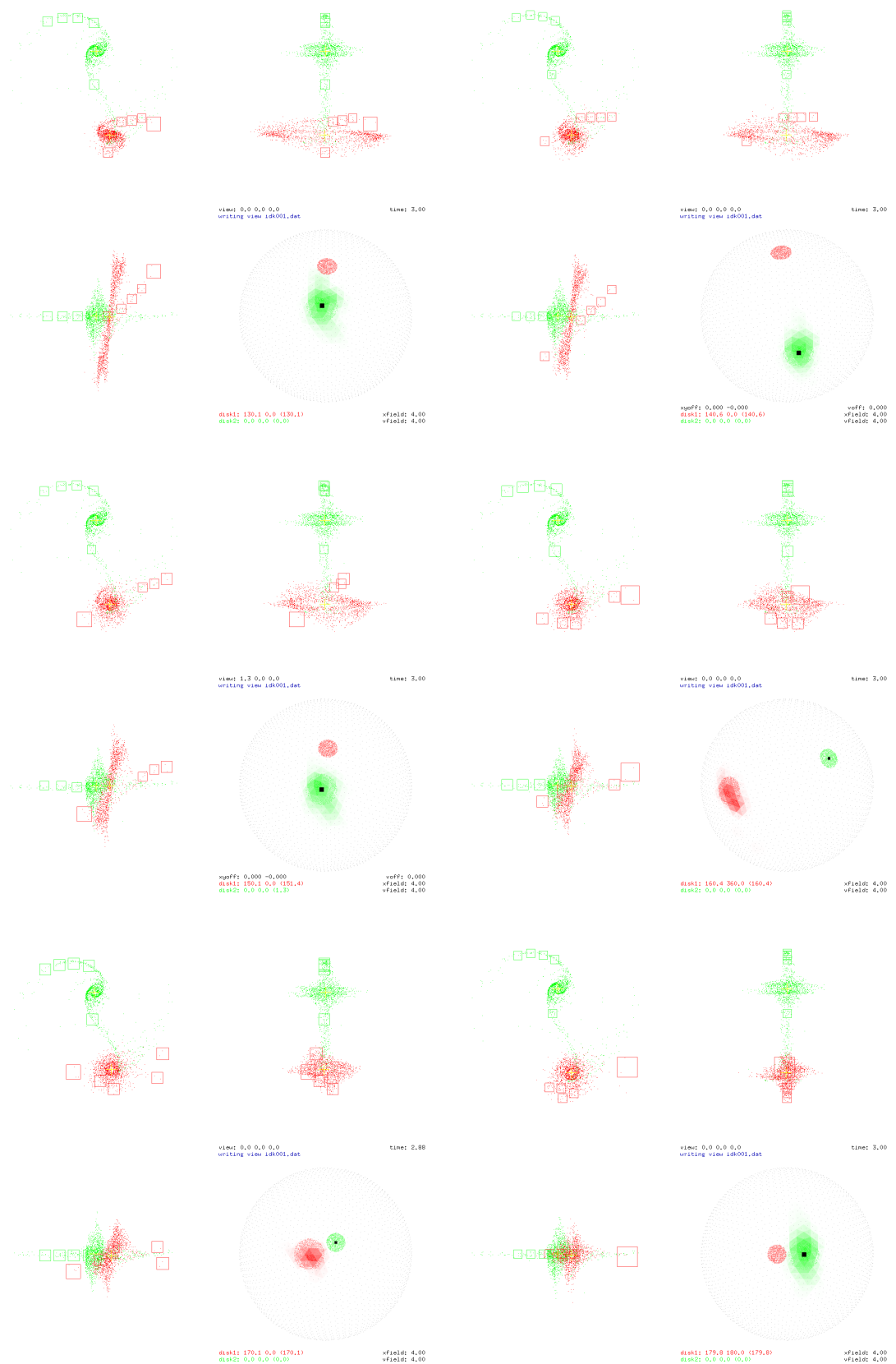


Figure 4-7: In standard reading order: systems with i_2 in $(130^\circ, 180^\circ)$.

We clarify the interpretation for the observations. When a box, which complies with selecting an appropriate tidal region (see 4-4 for an example), is placed in the XY projection we can choose any arbitrary line-of-sight velocity for it that has the specified (X, Y) positions. In other words, it is not assumed that integral field spectroscopy was made in the data. In this way, measurements can be understood as performed by long-slit spectroscopy, one slit oriented along the X axes and other along the Y axes; both of them containing both galaxies in the slit.

In the light of the last comment, it is valuable to say that observations of long slit spectroscopy are enough for the systems in which the disk 1 have inclinations from 0^{circ} to 90^circ as well as 120^circ . This because the majority of tidal features have a one to one correspondence between its spatial distribution ((X, Y) projection) and its velocities. This fact makes the methodology interesting since in some occasions two slits are enough to determine the measurements for the tidal regions (see fig. 4-5 and 4-6). On the other hand, the systems in which disk 1 have inclinations $100^circ - 110^circ$, 130^circ , $160^circ - 180^circ$ there is not one to one correspondence between the spatial components and the line-of-sight velocities. As a result, other measurements apart from the obtained by the two long slits will be needed if it is still of our intention to make use of tidal features unequivocally. In fact, we followed such assumption and it can be imagined that integral field spectroscopy was carried out for such systems in the regions needed (see fig. 4-6 and 4-7).

Another matter of importance are the sizes of the boxes that enclosed the tidal regions. It was assumed that each box had a minimum size of $1.25\ Kpc$, which is more than in agreement with a possible resolution to be obtained. Furthermore, the boxes were considered of larger size only when a small number of particles could be enclosed by the box in a one to one correspondence between spatial tidal regions and the line-of-sight velocities. Furthermore, the analysis in [2] shows that at least 3 boxes per galaxy are necessary to start getting reasonable results, we therefore used 5 boxes whenever possible; of course this based on the fact that the increase in boxes improves the final estimated result.

Finally, we consider that the normalization of the peak to one could be justified

as follows. First, if each region has enough particles it can lead to a reasonable estimate of the same spin distribution. Therefore, the normalization of the peak to one can be interpreted as giving the same density distribution for each region in some standard frequency units. Furthermore, the fact that such normalization is made by its maximum can be justified from the fact that the final estimation is intended to be from a maximum likelihood estimation; in other words, a better estimation of the maximum is of priority. Despite this, we found that the mean is a better estimate for the majority of the cases.

Estimations of i and w

First, it should be remembered that all the results to be illustrated in this section are for systems in which one disk is face-on with $i = 0^\circ$ and another has a given inclination with $w = 0^\circ$. Now, based on the resultant distribution of the spins for disk 1 (in the light of the tidal regions), we estimate the spins of disks 1 from the most probable spin and the mean spin (normalized to 1) in the distributions. The results can be observed in figure 4-8 at the right. The cumulative distribution function of the relative error of such estimates is observed in figure 4-8 at the left.

Important results are observed from fig. 4-8. First, the cumulative distribution function obtained lets us observe that we should expect relative errors of less than 10° for the estimation of the spin. This fact points us hint towards fundamental progress, since this error would reduce the search for the galaxy orientation from all the sphere to a region that represents 1 % of its area. Nevertheless, further analysis is needed if we are to affirm this with a confidence level. Another interesting feature is that for certain range of relative errors the estimation with the maximum appears to perform better than with the mean (observed by similar cdf values than the mean cdf, but for lower relative errors). Nevertheless, the mean estimate appears to have larger accuracy for the majority of the cases. Here, 12 of the 19 systems are better estimated with the mean. Moreover, for almost all the range of Δs it can be observed that when both cdf's have similar values the Δs associated with the mean estimate is considerable lower; in fact the cdf for the Δs_{means} reach one at $\approx 7^\circ$ while the cdf for

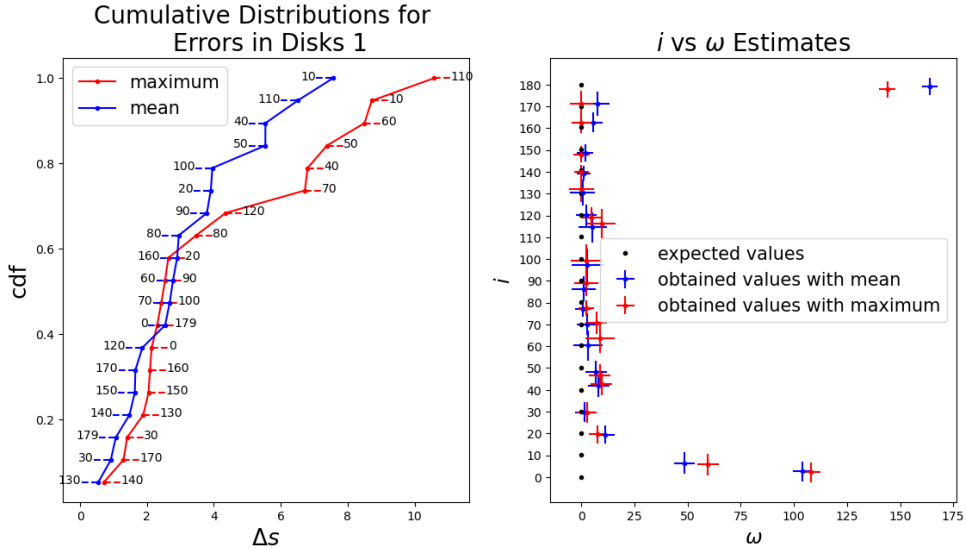


Figure 4-8: At the left: the estimated cumulative distribution function of relative errors for systems with $w = 0^\circ$ and any inclination; while the other disk is face-on with $i = 0^\circ$. Each point represents a system and the inclination associated with each error is placed near; the red line indicates estimation with the maximum and the blue one with the mean. At the right: the resultant values of the inclination and the angle of periapsis based on the spin estimated for each galaxy. The “error” is calculated as the angle between the spin estimated \hat{s} and the vector $\hat{s} + \sigma_{\hat{s}}\hat{u}$, where $\hat{s} \cdot \hat{u} = 0$; color codes follow the same convention.

the Δs_{max} does it at $\approx 10^\circ$. As a result, the ignorance of the relative error beforehand would make us bias to prefer the mean over the maximum to perform estimations.

It must be mentioned that in [2] it was found that the maximum was preferred (though a smaller number of systems were considered and they had in general any orientation). On the other hand, the figure 4-8 (right) shows that for all of the systems the inclination is within one standard deviation of the distribution $\Omega_d^*(\mathbf{s})$. Nevertheless, this is not the case for a considerable number (≈ 7) of w estimates. Despite that, this makes some w estimates consistent with the fact that larger relative errors should be expected, that is, when i is near 0° or 180° , cases in which all the w are equivalent (if we have in fact symmetry along an axis). This behaviour is clearly more pronounced for low inclinations and we consider that could be improved by selecting the most remote areas of the tidal regions, which would have the largest and lowest extensions for low and high inclinations, respectively. In fact, the tidal

regions selected in $i = 170^\circ$ are consistent with this idea and the estimate improves considerably. It must be mentioned though that for the extreme cases of $i = 180^\circ$ and $i = 0^\circ$ no improvement should be expected in the w estimate by its natural degeneracy. In fact, a case of improvement in such extreme cases will instead indicate a problem with the methodology proposed.

4.4 Uncertainties

4.4.1 Confidence Intervals of i and w

Even with the promising results exposed before, the association of a confidence region to the spins estimated is fundamental for statistical consistency. Nevertheless, consider a confidence region on the spin sphere (i. e. S^2) is an involved geometrical problem as it can be partially be observed from the complex colormaps of the resultant spin distributions at figures 4-5-4-7, which hint that percentil contours over the sphere will be geometric involved and that the discretization of the sphere have an important effect. As a result, we determine in a first approximation the confidence interval from the resultant inclination and argument of periapsis distributions obtained for each disk from eq. 4.18.

More concretely, we sampled $N = 10^6$ possible spins from eq. 4.18, and from them the i and w resultant distributions were estimated by their histograms. As an example, figure 4-9 illustrates the i_1 and w_1 histograms in which disk 1 has the ground true values values $w_1 = 0^\circ$ and $i_1 = 40^\circ$ and disk 2 is face-on with $i = 0^\circ$. It is observed that the inclination distribution has a well centered peak. Nevertheless, there is still a considerable probability outside the region $(35^\circ, 45^\circ)$ ($\approx 6.5\%$). On the other hand, the w distribution is well centered too, the values around 350° can be in fact interpreted as -10° thanks to the periodicity. In the range of $i_1 = 10^\circ$ to $i_1 = 170^\circ$ similar histograms are obtained; the exceptions have a more uniform probability in w .

However, some i histograms do not have a well centered peak value. For instance,

the resultant histograms for disks 1 in which it has ground true values $i_1 = 70^\circ$ and $w_1 = 0^\circ$ illustrates such a case (see fig. 4-10). Despite the not well centered peak, it must be remarked that all the distributions in i had the majority of the probability around the ground true inclination.

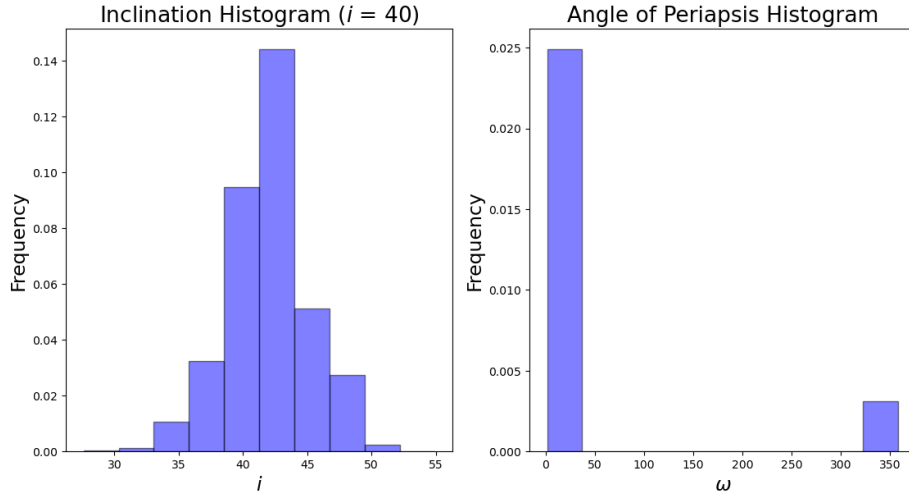


Figure 4-9: Resultant distributions for the inclination i and the angle of periapsis w , for the case in which disk 1 has $i = 40^\circ$ and $w = 0$.

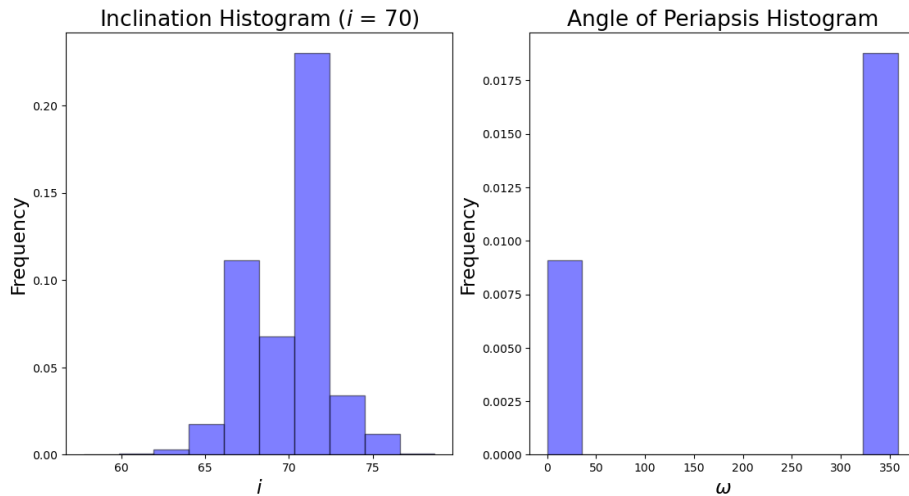


Figure 4-10: Resultant distributions for the inclination i and the angle of periapsis w , for the case in which disk 1 has $i = 70^\circ$ and $w = 0$.

Now, based on the assumption that the smaller probabilities are being underestimated in the i and w histograms it would be wise to calculate a confidence interval with a small p value ($p \approx 0.01$), such that the error is maximized. This gross supposition is supported in the fact that an extensive statistical analysis is indeed needed for all the assumptions that have been made, so that it would be prudent to overestimate possible errors. Furthermore, fig. 4-8 shows that some estimated inclinations are just barely within one standard deviation. Despite all, it will be observed that even if an uniform distribution is considered in the resultant confidence intervals estimated, the parameter space is reduced to a 3% of its initial considered volume in the worst case scenario.

From the fact that the resultant distributions can be multimodal the confidence interval is calculated as follows. The probabilities of the histogram (each associated to a range) are summed up in order of larger probability to the least until the desired confidence value is obtained, then the region associated with such probability is considered as the confidence interval. It must be mentioned that in some cases such regions are not necessarily open sets. In such cases, we simply include the intermediate regions such that the size of the final region is minimized (the periodic nature of the variable gives two ways to consider the final region).

With the last considerations in mind, with a confidence level of 99% the estimates for the inclinations i can be observed in figure 4-11; the error was approximated as half the size of the confidence interval. It is observed that all the obtained values are contained within the confidence interval. For these results would be more correct to say (in comparison with the analysis made for fig. 4-8) that at most 90% of the obtained values are expected to have relative errors of less than 10° with an estimated confidence interval of 99 %. This is consistent with the cumulative distribution function in fig. 4-8. Furthermore, for some cases larger errors are obtained as it is the case of 90° . We agree with [2] that it has to do with the fact in such cases the information of one spatial coordinate is not available; which as a result hinders the identification of tidal regions (see $i_1 = 90^\circ$, $i_1 = 100^\circ$ and $i_1 = 110^\circ$ in fig. 4-6).

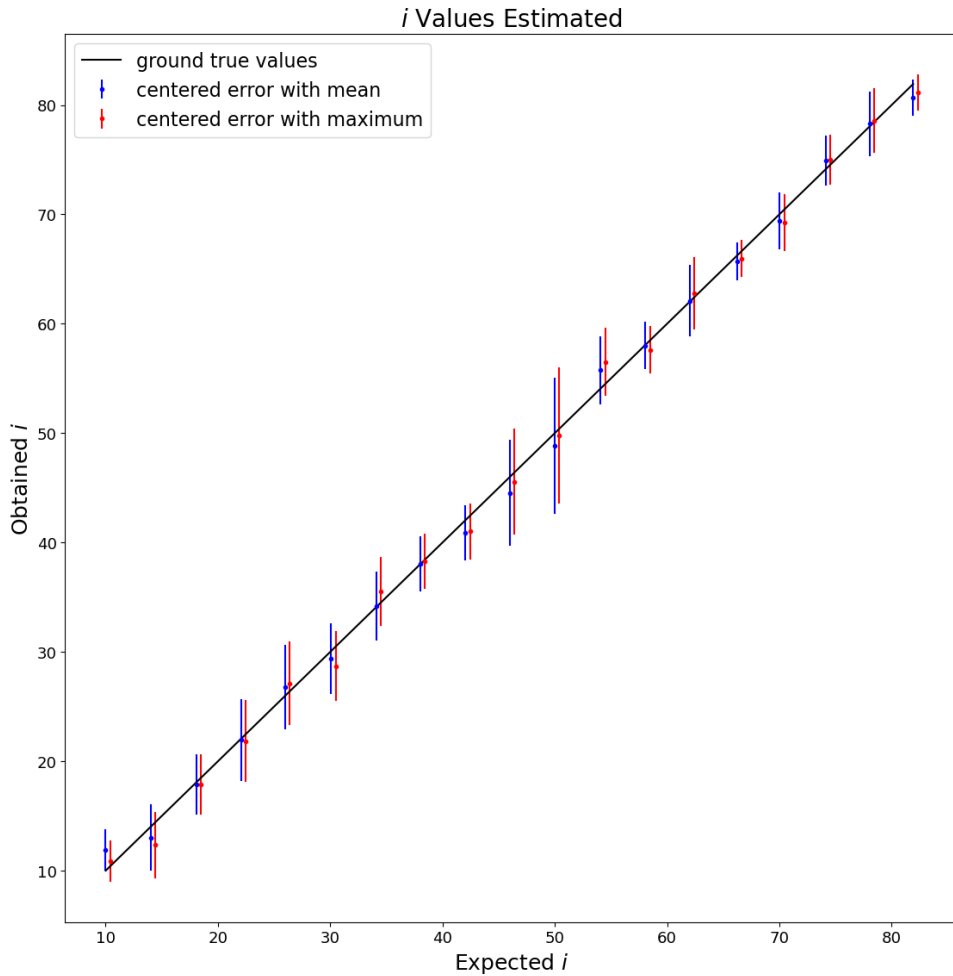


Figure 4-11: Estimated values for the inclinations of disks 1 using the maximum and mean of the resultant inclination distribution. The ground true values for the maximum estimation are shifted 1° to the right for visualization purposes.

On the other hand, the estimations for w have considerably larger intervals. Figure 4-12 shows the estimations with the respective confidence intervals for each inclination; again with an 99 % confidence level. In general, it is observed that w is known for 90% of the cases within an error of less than 40°. Again, the confidence intervals are consistent with the previous analysis of fig. 4-8.

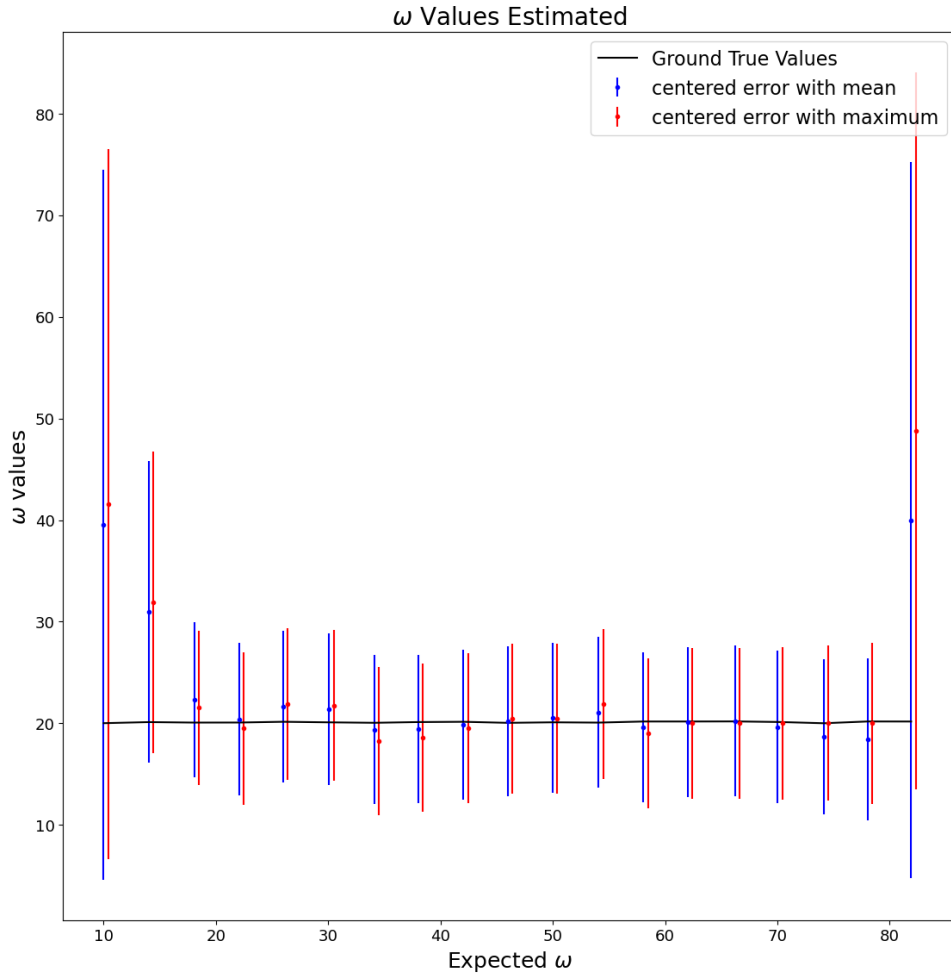


Figure 4-12: Estimated values for the angle of periapsis of disk 2 using the maximum and the mean of the resultant angle of periapsis distribution. The ground true values for the maximum estimation are shifted 1° to the right for visualization purposes.

Figures 4-11 and 4-12 illustrate important implications. In fact, even with errors of 10° and 40° for the parameters (i, w) in disk 1, the parameter space is reduced to approximately 3% of its original volume (in the worst case scenario), which is quite remarkable. This calculation is given by the solid angle around the estimates with the errors obtained from the confidence intervals. Moreover, the cases of $i = 0^\circ$ and $i = 180^\circ$ must be excluded from this reasoning (although not from the conclusion).

The confidence intervals of w when disk 1 or 2 have some of the inclinations of the excluded cases are consistent with the fact that w must be degenerate, the confidence intervals in such cases are $\approx(0, 350)$. So, even interpreting this as meaning that all possible w angles are equally valid, the resultant solid angle with the consistent interval for $i_{estimated} \pm 20^\circ$ leads to a solid angle of 3% of the one of the total sphere.

4.4.2 Compared Errors in Both Disks

Finally, it is valuable to shortly analyze the estimations made for disk 2. Of particular interest is the fact that it was always evaluated in the configuration $i = 0^\circ$, and that therefore we can analyze with better precision the relative errors that we should expect for such inclination. For this purpose and in order to compare with the errors in the estimations of disk 1, the cumulative distribution functions of several quantities that quantify the error in the spins estimated are illustrated in figure 4-13.

From fig. 4-13 it is observed that the errors obtained for the determinations of disk 1 are larger. In fact the mean error is approximately 30% larger than in disk 2 when the estimations are made with the maximum of the spin distribution. Similarly, the mean error is 40% and 66% larger when estimates are made with the mean of the spin distribution and the half size of the confidence interval of the inclination, respectively. Additionally, it is noted that for disk 2 all the relative errors as well as the errors estimated for the inclination are always below 10° .

Another fact that can be observed from the figure is that the confidence level considered for the inclinations is in fact an overestimation of the expected error, since the error associated with the inclination is in most of the cases (97% of them) larger than the relative errors obtained for the orientations. Nevertheless, the fact that is not 100% does not lead to inconsistencies since it follows naturally from the geometry of the sphere that if we have an error $\epsilon(i)_{p=0.99}$ for the inclination then $\epsilon(\hat{s})_{p=0.99} >= \epsilon(i)_{p=0.99}$; where the subindex denote the confidence level, ϵ operates to give the error from the distribution. Besides, for disk 1 it is more pronounced the fact that the mean gives better estimations. This nevertheless is well related with the fact that the maximization depends on the grid considered over the sphere and such discreteness

naturally affects the estimation, while in the case of the mean such effect is better balanced. Finally, this discreteness could also be the cause that for low relative errors the cdf's of disk 2 have different shapes when estimates are done with the maximum, while for disk 1 all of its cdf's have similar shapes.

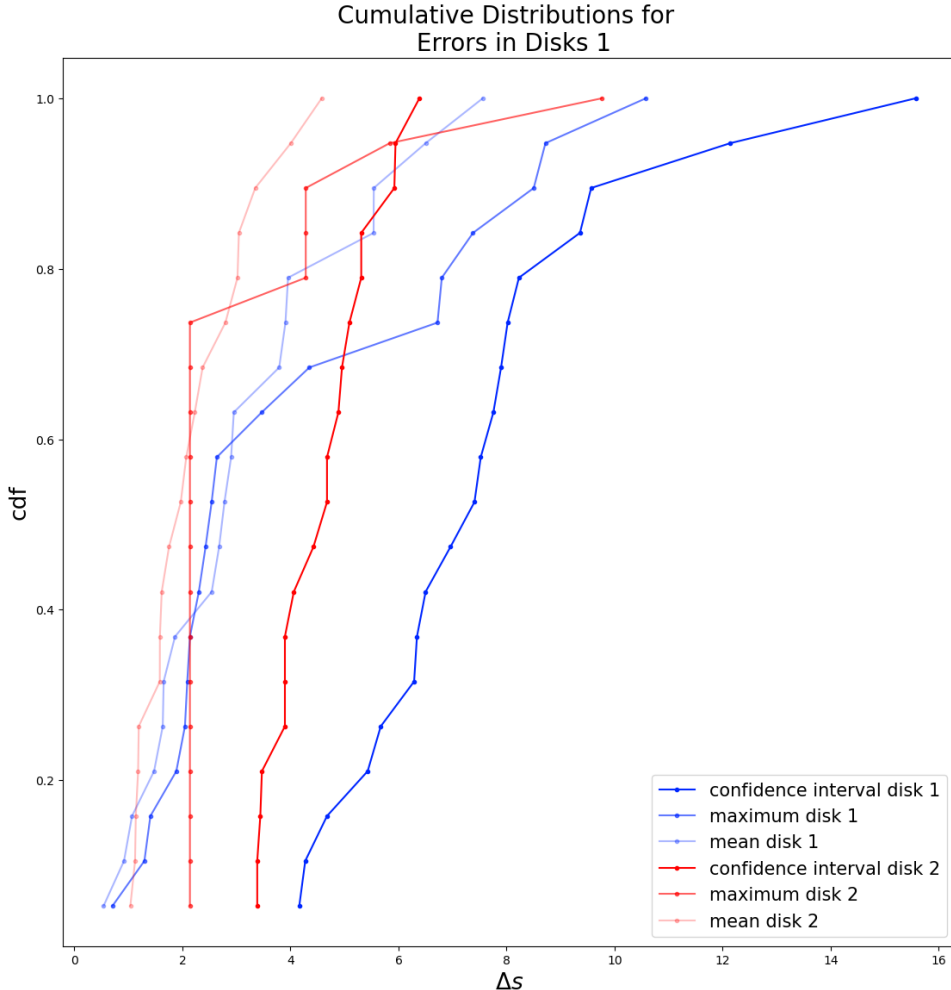


Figure 4-13: The blue lines are cumulative distribution functions for disk 1. In order of less to greater lightness in the blue we have the cumulative distribution functions for: error obtained from the i confidence intervals, relative error by the maximum estimation of the spin distribution, and relative error by the mean estimation of the spin distribution. Similarly, in red are illustrated the cdfs for the disk 2 with the same color code in lightness.

4.5 Conclusions

Some of the suppositions used in the methodology explained in [2] are clarified with more detail and important arguments to complement it are presented. In particular, the conditions in which two long-slit spectroscopy can be enough and when additional observations could be necessary. Additionally, the justification by which the normalization by the maximum in eq. 4.15 still leads to the final distribution in eq. 4.18.

In contrast with [2] it was found that the mean spin of 4.18 was better to estimate (i_d, w_d) than the maximum. These, nevertheless, for systems in which one disk is face-on with $i = 0$ and another has a certain value of inclination and $w = 0$. Furthermore, our results for edge-on systems could appear to differ with the ones in [2] for the same type of systems since our relative errors obtained were below 10° , while in [2] error of 14° are obtained. Nevertheless, this is only apparent because the errors from the i confidence intervals for $i_1 = 90^\circ, 100^\circ, 110^\circ$ are evidently higher $12^\circ, 15^\circ, 8^\circ$, respectively. Furthermore, it must be added that the lack of information for edge-on systems in one spatial direction makes complicated the selection of tidal features; which consequently lead to a considerable error (see $i_1 = 110^\circ$ in 4-6).

An statistical analysis of confidence intervals was made to give meaningful errors to the i and w estimates based on the observations of the tidal regions. This analysis showed that even in the worst case scenarios the parameter space is reduced to a 3% of its initial volume under a 99% confidence level. Furthermore, the fact that the new parameter space (in which we can search the spins) is overestimated is well justified by the estimated cumulative distribution functions in figure 4-13. More concretely, it is observed that the cumulative distribution function for the relative errors with the maximum and mean estimation arrives to 1 considerably faster than the cdf for the inclination errors.

The observation of tidal regions can well constrain the parameters i_d and w_d given that the rest of the parameters are known. Despite this assumption, in the scenario in which the rest of parameters are unknown the methodology is still potentially useful.

For example, we could simply consider all possible mappings of the Euler angles and scale parameters from the observations (X, Y, V_Z) to (x, y, v_z) and take the mean of all the spin estimates in each case that the confidence interval size obtained for the inclination is less than certain value.

General properties for the i and w distributions were found for systems in which one disk is face-on with $i = 0^\circ$ and the other has any inclination with $w = 0^\circ$. More concretely, it was observed that w distributions tend to be considerably uniform for the limiting cases of $i = 0^\circ$ and $i = 180^\circ$. Furthermore, for the other cases it was found that w had two distinct peaks, one around 0° and other around 350° . Regarding the inclinations, it was found that the possible values were considerably concentrated around the ground true inclination (at a maximum distance of about 10°) although not all distributions had necessarily a well centered peak.

The fact that the cumulative distributions functions of disk 1 arrive considerably faster to 1 than the ones of disk 2 justify the considerations of errors in a different way for systems with different estimated spins. In other words, it would be valuable to construct the cdf for systems in which one galaxy has a fixed inclination while the companion has different configurations. This is evident from the fact that the mean error deduced for disks 1 from the cumulative distribution function is approximately 40% greater than the mean error for disk 2.

Bibliography

- [1] A. Toomre and J. Toomre, “Galactic Bridges and Tails,” *ApJ*, vol. 178, pp. 623–666, Dec. 1972.
- [2] J. E. Barnes, “Identikit 2: an algorithm for reconstructing galactic collisions,” *MNRAS*, vol. 413, no. 4, pp. 2860–2872, Jun. 2011.
- [3] J. E. Barnes and J. E. Hibbard, “Identikit 1: A Modeling Tool for Interacting Disk Galaxies,” *AJ*, vol. 137, no. 2, pp. 3071–3090, Feb. 2009.
- [4] S. A. Mortazavi, J. M. Lotz, J. E. Barnes, and G. F. Snyder, “Modeling the initial conditions of interacting galaxy pairs using Identikit,” *MNRAS*, vol. 455, no. 3, pp. 3058–3074, Jan. 2016.
- [5] G. C. Privon, J. E. Barnes, A. S. Evans, J. E. Hibbard *et al.*, “Dynamical Modeling of Galaxy Mergers Using Identikit,” *ApJ*, vol. 771, no. 2, p. 120, Jul. 2013.
- [6] J. Pfleiderer and H. Siedentopf, “Spiralstrukturen durch Gezeiteneffekte bei der Begegnung zweier Galaxien. Mit 7 Textabbildungen,” *ZAp*, vol. 51, p. 201, Jan. 1961.
- [7] E. Poggio, R. Drimmel, R. Andrae, C. A. L. Bailer-Jones *et al.*, “Evidence of a dynamically evolving Galactic warp,” *Nature Astronomy*, Mar. 2020.
- [8] P. N. Appleton and C. Struck-Marcell, “Collisional Ring Galaxies,” *Fundamentals of Cosmic Physics*, vol. 16, pp. 111–220, Jan. 1996.
- [9] V. C. Rubin, J. Ford, W. K., and N. Thonnard, “Rotational properties of 21 SC galaxies with a large range of luminosities and radii, from NGC 4605 ($R=4\text{kpc}$) to UGC 2885 ($R=122\text{kpc}$).” *ApJ*, vol. 238, pp. 471–487, Jun. 1980.
- [10] J. C. Muñoz-Cuartas, A. V. Macciò, S. Gottlöber, and A. A. Dutton, “The redshift evolution of Λ cold dark matter halo parameters: concentration, spin and shape,” *MNRAS*, vol. 411, no. 1, pp. 584–594, Feb. 2011.
- [11] L. Hernquist and P. J. Quinn, “Shell Galaxies and Alternatives to the Dark Matter Hypothesis,” *ApJ*, vol. 312, p. 17, Jan. 1987.
- [12] J. Shi, H. Wang, H. Mo, M. Vogelsberger *et al.*, “The Formation History of Subhalos and the Evolution of Satellite Galaxies,” *arXiv e-prints*, p. arXiv:2001.04090, Jan. 2020.

- [13] J. F. Wallin and B. V. Stuart, “Mass Transfer and Loss in Interacting Disk Galaxies,” *ApJ*, vol. 399, p. 29, Nov. 1992.
- [14] R. Beck, “Magnetic fields in spiral galaxies,” *Springer*, vol. 24, p. 4, Dec. 2015.
- [15] F. Combes, F. C. Foy, S. T. Gottesman, and L. Weliachew, “Neutral hydrogen observations and computer modelling of the interacting galaxies NGC 672-IC 1727.” *A&A*, vol. 84, pp. 85–92, Apr. 1980.
- [16] V. Springel, “The cosmological simulation code GADGET-2,” *MNRAS*., vol. 364, no. 4, pp. 1105–1134, Dec. 2005.
- [17] R. A. Crain, J. Schaye, R. G. Bower, M. Furlong *et al.*, “The EAGLE simulations of galaxy formation: calibration of subgrid physics and model variations,” *MNRAS*., vol. 450, no. 2, pp. 1937–1961, Jun. 2015.
- [18] J. Schaye, R. A. Crain, R. G. Bower, M. Furlong *et al.*, “The EAGLE project: simulating the evolution and assembly of galaxies and their environments,” *MNRAS*., vol. 446, no. 1, pp. 521–554, Jan. 2015.
- [19] R. K. Sheth, H. J. Mo, and G. Tormen, “Ellipsoidal collapse and an improved model for the number and spatial distribution of dark matter haloes,” *MNRAS*, vol. 323, no. 1, pp. 1–12, May 2001.
- [20] H. J. Mo, S. Mao, and S. D. M. White, “The formation of galactic discs,” *MNRAS*, vol. 295, no. 2, pp. 319–336, Apr. 1998.
- [21] H. Y. Wang, Y. P. Jing, S. Mao, and X. Kang, “The phase-space distribution of infalling dark matter subhaloes,” *MNRAS*, vol. 364, no. 2, pp. 424–432, Dec. 2005.
- [22] S. Khochfar and A. Burkert, “Orbital parameters of merging dark matter halos,” *A&A*, vol. 445, no. 2, pp. 403–412, Jan. 2006.
- [23] A. R. Wetzel, “On the orbits of infalling satellite haloes,” *MNRAS*, vol. 412, no. 1, pp. 49–58, Mar. 2011.
- [24] J. Binney and S. Tremaine, *Galactic dynamics*. Princeton University Press, 1987.
- [25] ——, *Galactic Dynamics: Second Edition*. Princeton University Press, 2008.
- [26] G. Kauffmann, S. D. M. White, T. M. Heckman, B. Ménard *et al.*, “The environmental dependence of the relations between stellar mass, structure, star formation and nuclear activity in galaxies,” *MNRAS*., vol. 353, no. 3, pp. 713–731, Sep. 2004.
- [27] L. Hernquist and N. Katz, “TREESPH: A Unification of SPH with the Hierarchical Tree Method,” *ApJS*, vol. 70, p. 419, Jun. 1989.

- [28] B. W. Carroll and D. A. Ostlie, *An introduction to modern astrophysics and cosmology*. Pearson, 2006.
- [29] J. L. S. Herbert Goldstein, Charles P. Poole, *Classical mechanics*, 3rd ed. Addison Wesley, 2001. [Online]. Available: <http://gen.lib.rus.ec/book/index.php?md5=07ed7dc1a346369dea8f9f34caa1b165>
- [30] D. A. Forbes and P. Kroupa, “What is a galaxy? cast your vote here,” *Publications of the Astronomical Society of Australia*, vol. 28, no. 1, p. 77–82, 2011.
- [31] M. R. Blanton, M. A. Bershadsky, B. Abolfathi, F. D. Albareti *et al.*, “Sloan Digital Sky Survey IV: Mapping the Milky Way, Nearby Galaxies, and the Distant Universe,” *AJ*, vol. 154, no. 1, p. 28, Jul. 2017.
- [32] J. F. Navarro, E. Hayashi, C. Power, A. R. Jenkins *et al.*, “The inner structure of Λ CDM haloes - III. Universality and asymptotic slopes,” *MNRAS*, vol. 349, no. 3, pp. 1039–1051, Apr. 2004.
- [33] I. King, “The structure of star clusters. I. an empirical density law,” *AJ*, vol. 67, p. 471, Oct. 1962.
- [34] A. Gómez-Muñoz. and J. C. Muñoz-Cuartas, “Two body mapping codes,” github.com/Andresgomez970/Investigation_codes, 2021.
- [35] L. F. Quiroga, J. C. Muñoz-Cuartas, I. Rodrigues, and N. I. Libeskind, “Simulating the galactic system in interaction AM 2229-735 and the formation of its polar structure,” *MNRAS*, vol. 491, no. 2, pp. 1887–1900, Jan. 2020.
- [36] Arboleda, L. C., and J. C. Muñoz-Cuartas, “Efectos de los Procesos de Aniquilación de Materia Oscura en la Formación de Estructuras a gran escala,” Master’s thesis, Universidad de Antioquia, Dec. 2015.
- [37] F. Zwicky, “Luminous Intergalactic Matter,” *PASP*, vol. 64, no. 380, p. 242, Oct. 1952.
- [38] J. Pfleiderer and H. Siedentopf, “Spiralstrukturen durch Gezeiteneffekte bei der Begegnung zweier Galaxien. Mit 7 Textabbildungen,” *ZAp*, vol. 51, p. 201, Jan. 1961.
- [39] J. Pfleiderer, “Über Gezeitenwirkungen bei der Begegnung von Galaxien,” Ph.D. dissertation, -, Jan. 1961.
- [40] ——, “Gravitationseffekte bei der Begegnung zweier Galaxien. Mit 5 Textabbildungen,” *ZAp*, vol. 58, p. 12, Jan. 1963.
- [41] A. Toomre and J. Toomre, “On Intergalactic Bridges.” in *Bulletin of the American Astronomical Society*, vol. 2, Sep. 1970, p. 350.

- [42] A. E. Wright, “Computational Models of Gravitationally Interacting Galaxies,” MNRAS, vol. 157, no. 3, pp. 309–333, 05 1972. [Online]. Available: <https://doi.org/10.1093/mnras/157.3.309>
- [43] N. Tashpulatov, “The Tidal Effect and the Formation of Bars and Tails in Galaxies. I. Tidal Formation of Linear Bridges between Galaxies.” Soviet Ast., vol. 13, p. 968, Jun. 1970.
- [44] L. Hernquist, “An Analytical Model for Spherical Galaxies and Bulges,” ApJ, vol. 356, p. 359, Jun. 1990.
- [45] G. Vaucouleurs, “Classification and Morphology of External Galaxies,” *Handbuch der Physik*, vol. 11, pp. 275–310, Jan. 1959.
- [46] J. F. Navarro, C. S. Frenk, and S. D. M. White, “The Structure of Cold Dark Matter Halos,” ApJ, vol. 462, p. 563, May 1996.
- [47] J. Barnes and P. Hut, “A hierarchical $O(N \log N)$ force-calculation algorithm,” Nature, vol. 324, no. 6096, pp. 446–449, Dec. 1986.
- [48] V. Springel, R. Pakmor, O. Zier, and M. Reinecke, “Simulating cosmic structure formation with the GADGET-4 code,” *arXiv e-prints*, p. arXiv:2010.03567, Oct. 2020.
- [49] J. Barnes, “Treecode guide,” ifa.hawaii.edu/faculty/barnes/treecode/treeguide.html, 2001.
- [50] J. E. Barnes, “Encounters of Disk/Halo Galaxies,” ApJ, vol. 331, p. 699, Aug. 1988.
- [51] J. J. Monaghan, “Smoothed particle hydrodynamics.” ARA&A, vol. 30, pp. 543–574, Jan. 1992.